8-27-2012

Uranium-series geochronology and stable isotope analysis of travertine from Soda Dam, New Mexico : a Quaternary record of episodic spring discharge and rivern incision in the Jemez Mountains hydrothermal system

April Jean Tafoya

April Jean Tafoya

Candidate

Earth and Planetary Sciences

Department

This thesis is approved, and it is acceptable in quality and form for publication:

Approved by Thesis Committee:

Dr. Laura Crossey, Chairperson

Dr. Karl Karlstrom

Dr. Yemane Asmerom

Dr. Louis Scuderi

URANIUM-SERIES GEOCHRONOLOGY AND STABLE ISOTOPE ANALYSIS OF TRAVERTINE FROM SODA DAM, NEW MEXICO: A QUATERNARY RECORD OF EPISODIC SPRING DISCHARGE AND RIVER INCISION IN THE JEMEZ MOUNTAINS HYDROTHERMAL SYSTEM

BY

April Jean Tafoya

B.S., Environmental Sciences, University of New Mexico, 2010

M.S., Earth and Planetary Sciences, University of New Mexico, 2012

THESIS

Master of Science
Earth and Planetary Sciences

The University of New Mexico
Albuquerque, New Mexico

August, 2012

ACKNOWLEDGEMENTS

I would like to thank my advisors Dr. Laura Crossey and Dr. Karl Karlstrom for their assistance, patience and support in every aspect of this project. I would also like to thank Dr. Louis Scuderi for participation on my committee and generosity with his time. I greatly appreciate all the assistance and support from Dr. Yemane Asmerom and Dr. Victor Polyak with the University of New Mexico's Earth and Planetary Science Radiogenic Isotope Laboratory; without whom this project could not have been completed. Thank you as well to Viorel Atudorei with the Stable Isotopes Laboratory for all his time and interest in this project. Thanks also to Dr. Abdul-Mehdi S. Ali for the use of the Analytical Chemistry Laboratory for water chemistry analyses. Dr. Peter Fawcett's research provided invaluable data for interpretation and his generosity with his time and knowledge through my spontaneous office visits are greatly appreciated. I would also like to thank Dr. Fraser Goff and the various researchers associated with the Valles Caldera projects for their extensive and thorough work that allowed me to compile the information necessary for interpretation. I owe much appreciation for the help and input received from Alexandra Preiswich, Rebecca Wacker, Ryan Crow, Zachary Lapointe, Brandi Cron, Andy Jochems, Miela Kolomaznik and Kyle Paffett. This research was partially funded by the National Science Foundation's Louis Stokes for Minority Participation Bridge to the Doctorate Fellowship through Dr. Crossey's grant #NSF/EHR 1026412 and #NSF/EAR 0838575.

URANIUM-SERIES GEOCHRONOLOGY AND STABLE ISOTOPE ANALYSIS OF TRAVERTINE FROM SODA DAM, NEW MEXICO: A QUATERNARY RECORD OF EPISODIC SPRING DISCHARGE AND RIVER INCISION IN THE JEMEZ MOUNTAINS HYDROTHERMAL SYSTEM

April Jean Tafoya

Coauthors to include:

Crossey, L.J., Karlstrom, K.E., Polyak, V. and Asmerom, Y.

B.S., Environmental Sciences, University of New Mexico, 2010

M.S., Earth and Planetary Sciences, University of New Mexico, 2012

ABSTRACT

High precision uranium-series (U-series) geochronology provides data on timing of travertine deposition at Soda Dam, and a paleohydrologic record for the Valles Caldera hydrothermal system in Northern New Mexico for at least the last 500 ka. Travertine-depositing springs occur in San Diego Canyon, the only surface drainage outlet for the Valles Caldera, along the intersection of the Jemez fault zone (JFZ) and the Jemez River. This travertine-depositing hot spring system is part of the Valles Caldera geothermal system, which has been active throughout the Quaternary and explored for the past three decades for geothermal energy potential. New dates, compiled with previous dating, provide improved geochronologic and geologic context with respect to incision rates of the Jemez River and the episodic nature of travertine deposition.

The largest volume deposit (deposit A), high in the landscape on the west side of the river, yields stratigraphic ages ranging from >500 ka (outside of U-series range) to 287 ka, and caps paleo Jemez River gravels at 132 m above the modern river. Deposit A

is intruded by spar calcite dikes of 486, 455, and 339 ka that are interpreted as episodes of elevated hydrologic head in the hydrologic system generated by caldera paleolakes that were present in several unresolved intervals throughout the recent Quaternary, beginning immediately after the formation of the caldera 1.25 Ma. Intrusions also occur at 207, 211, 111 and 96 ka, during interglacial Marine Isotope Stage's (MIS) 9, 7 and 5. Deposit A_i is inset into deposit A and yields stratigraphic ages of 183 to 132 ka. Ancestral Jemez River gravels cemented by calcite rinds provide a terrace 30 m above the modern river and yield an age of 201 ka, producing a robust bedrock incision rate of 160 m/Ma for the last 200 ka. A cross-cutting calcite sill in deposit A_i yields ages of 111 and 210 ka, again suggesting locally elevated head during MIS 5 and MIS 7. Deposit B is a fissure/mound deposit on the east side of the river that developed along a fissure ridge straddling major Quaternary faults in the JFZ, much like the modern Soda Dam. The mound accumulation is 138 ka near the base and 78 ka at the top. The central fissure has a 1 m thick calcite vein system that displays mm scale banding; calcite vein growth took place approximately from 210 ka to 93 ka. These combined data indicate that the deposit B fissure/mound system was active for a 130 ka interval that spans glacial MIS 6 and the transition into interglacial MIS 5. Deposit C, a minor stratigraphic continuation of deposit B, is 103 ka at the base, capping river gravels 16.5 m above the modern river, and 101 ka at the top, indicating extensive platform development at about 100 ka. Deposit C yields a bedrock incision rate of 150 m/Ma since 101 ka, indicating semi-steady bedrock incision rates over the last 200 ka. Deposit D, the Soda Dam itself, began mound accumulation at 10 ka and is still actively depositing travertine.

Stable isotope values were obtained on 27 dated, and an additional 52 undated travertine samples. Oxygen isotope values ($\delta^{18}0$) have an exceptionally large range from $\delta^{18}0$ = -19 to -4‰ (PDB), reflecting variations in local spring chemistry, source water composition, temperature, as well as fractionation effects during deposition. Carbon isotope values ($\delta^{13}C$) range from +1.4 to +11.7‰ (PDB); these relatively positive values suggest kinetic enrichment during degassing of CO_2 and likely the influence of a magmatic/mantle endmember. Geochronology, combined with volume calculations,

indicate episodic travertine deposition along the Soda Dam fault system, with major accumulations broadly at >500 ka, 200-92 ka, and <10 ka. Over all, the Soda Dam travertine system provides an episodic record of travertine accumulation, river incision history and insights into paleohydrolgic conditions through stable isotope analysis for part of the Jemez hydrothermal system.

TABLE OF CONTENTS

INTRODUCTION 1
BACKGROUND ON TRAVERTINE FORMATION 6
STABLE ISOTOPES: PRESENT INDICATORS OF PAST HYDROLOGIC CONDITIONS 8
BACKGROUND: GEOLOGIC AND HYDROLOGIC SETTING OF THE SODA DAM SYSTEM 11
RESULTS - TRAVERTINE OCCURANCE: DISTRIBUTION, LANDSCAPE POSITION AND VOLUME 18
RESULTS - URANIUM-SERIES GEOCHRONOLOGY 20
RESULTS - STABLE ISOTOPES 23
STABLE ISOTOPES: INSIGHTS INTO PAST DEPOSITION CONDITIONS 26
RESULTS - JEMEZ RIVER INCISION RATES 28
INTERPRETATION OF TRAVERTINE AT SODA DAM IN TERMS OF REGIONAL/GLOBAL PALEOCLIMATE RECORDS 31
INSIGHTS FROM GEOCHRONOLOGY: PALEOHYDROLOGY AND CLIMATE-DRIVEN CONTROLS ON TRAVERTINE ACCUMULATIONS AS EVIDENCE FOR EPISODIC VARIATIONS IN SPRING DISCHARGE 34
SUMMARY OF MAIN FINDINGS 39
APPENDICES 40
APPENDIX A – METHODS 40
Water Sampling and Analysis Methods 40
Uranium-series Geochronology 40
Stable Isotope Geochemistry 40
Mapping and GIS Analysis 41
APPENDIX B – LIST OF FIGURES, TABLES AND CAPTIONS 42
APPENDIX D – SUPPLEMENTARY INFORMATION 65
Stable Isotopes of Carbon and Oxygen: 65
Paleothermometry: 66
Model Ages 68
WORKS CITED 69

LIST OF FIGURES AND TABLES

FIGURE 1 2
FIGURE 2 3
FIGURE 3 4
FIGURE 4 12
FIGURE 5 15
FIGURE 6 22
FIGURE 7 24
FIGURE 8 25
FIGURE 9 27
FIGURE 10 30
FIGURE 11 37
TABLE 1 80
TABLE 2 83
TABLE 3 93
TABLE 4 95
TABLE 5 66
TABLE 6 104

INTRODUCTION

Travertines are freshwater carbonate deposits that accumulate around CO_2-rich springs and can provide a record of past spring discharge. Previous work has suggested that travertine deposition is episodic, and associated with climatically wet conditions that correspond to global glacial periods in the arid Southwest (Szabo, 1990; Crossey et al., 2006; Embid, 2009). Carbonates are resistant to weathering in arid climates and can form a cap that preserves paleo-landscape elements. Ancient travertine deposits positioned high in the landscape provide insight into past hydrologic conditions, including fluctuation in elevation of the local hydrologic head through time. Precise uranium-series (U-series) dating of travertine that cements paleo-river gravels in elevated terrace deposits provides one of the most robust measures of incision rates in southwestern river systems (Pederson et al., 2002; Karlstrom et al., 2008).

Episodic travertine accumulation in ancient and modern deposits at Soda Dam, New Mexico, make this location an exceptional natural laboratory to study links between paleohydrologic conditions and the modern groundwater system. This extensive travertine accumulation is located in San Diego Canyon, which has been incised by the Jemez River, the only surface water drainage for the Valles Caldera (Figure 1). Hydrothermal water encountered by the Baca Wells during geothermal exploration is channeled in the subsurface through San Diego Canyon via the JFZ, and has comprised a portion of the water discharging at the Soda Dam hot springs and depositing travertine for the past >500 ka.

The hydrothermal system is recharged by meteoric water that infiltrates within the Valles Caldera, where it is heated by a shallow magmatic source and circulated with endogenic fluids, (including CO_2) before traveling in the subsurface, down the elevation gradient along the JFZ, mixing with additional meteoric recharge and shallow groundwater along the way (Goff et al., 2002; Figure 2). The JFZ acts as a conduit for the hydrothermal water, cutting across the Jemez River at the Soda Dam location and depositing travertine (Figure 3). Thus, U-series geochronology and stable isotope

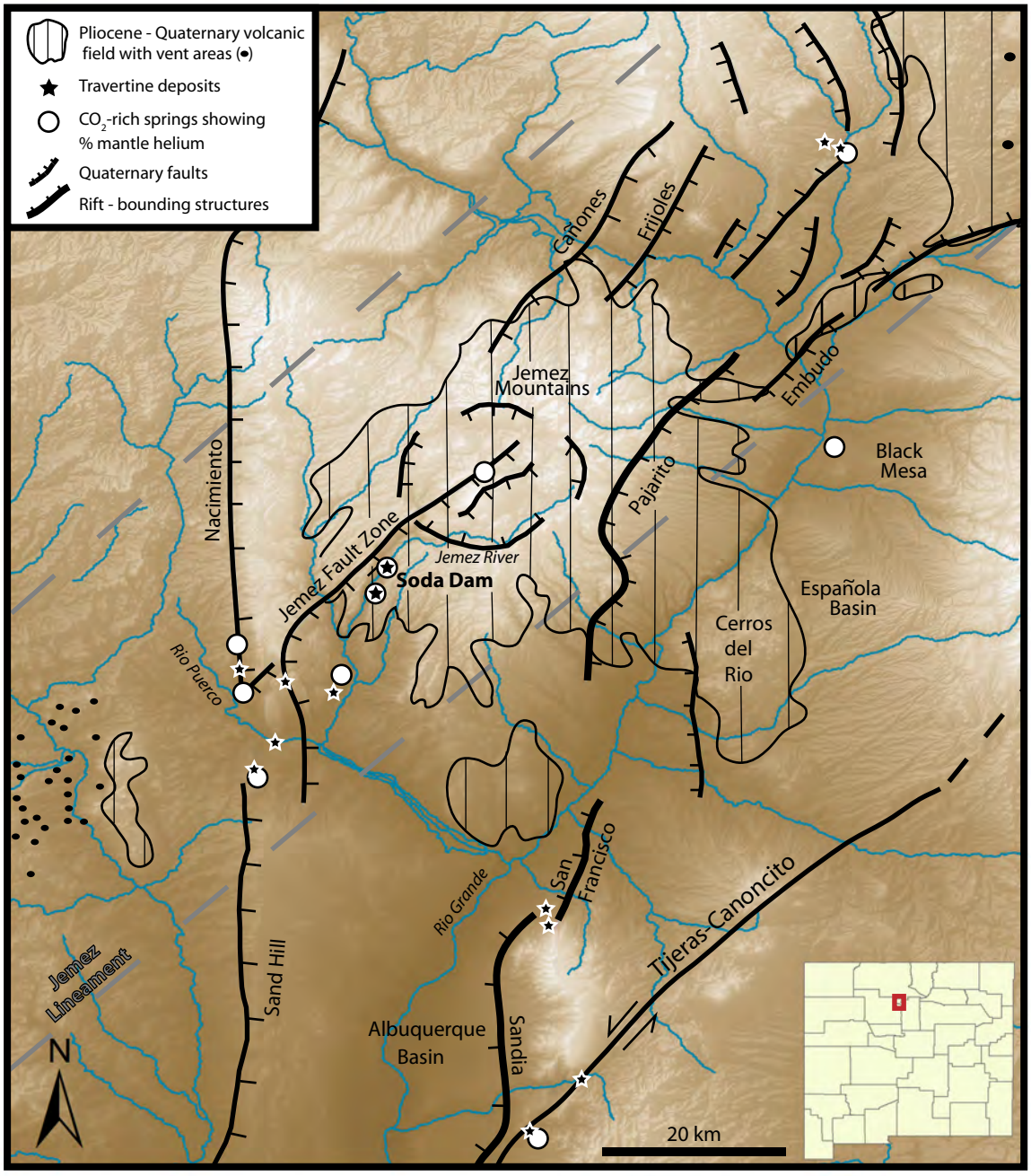

Figure 1: Tectonic DEM map of the Jemez transfer zone formed at the intersection of the Rio Grande rift, the Jemez lineament and Soda Dam. Neotectonic features of this area include: Quaternary extensional and transtensional faults, Plio-Pleistocene volcanic fields (line pattern), springs with mantle 3He (white dots), and Quaternary travertine deposits (stars).

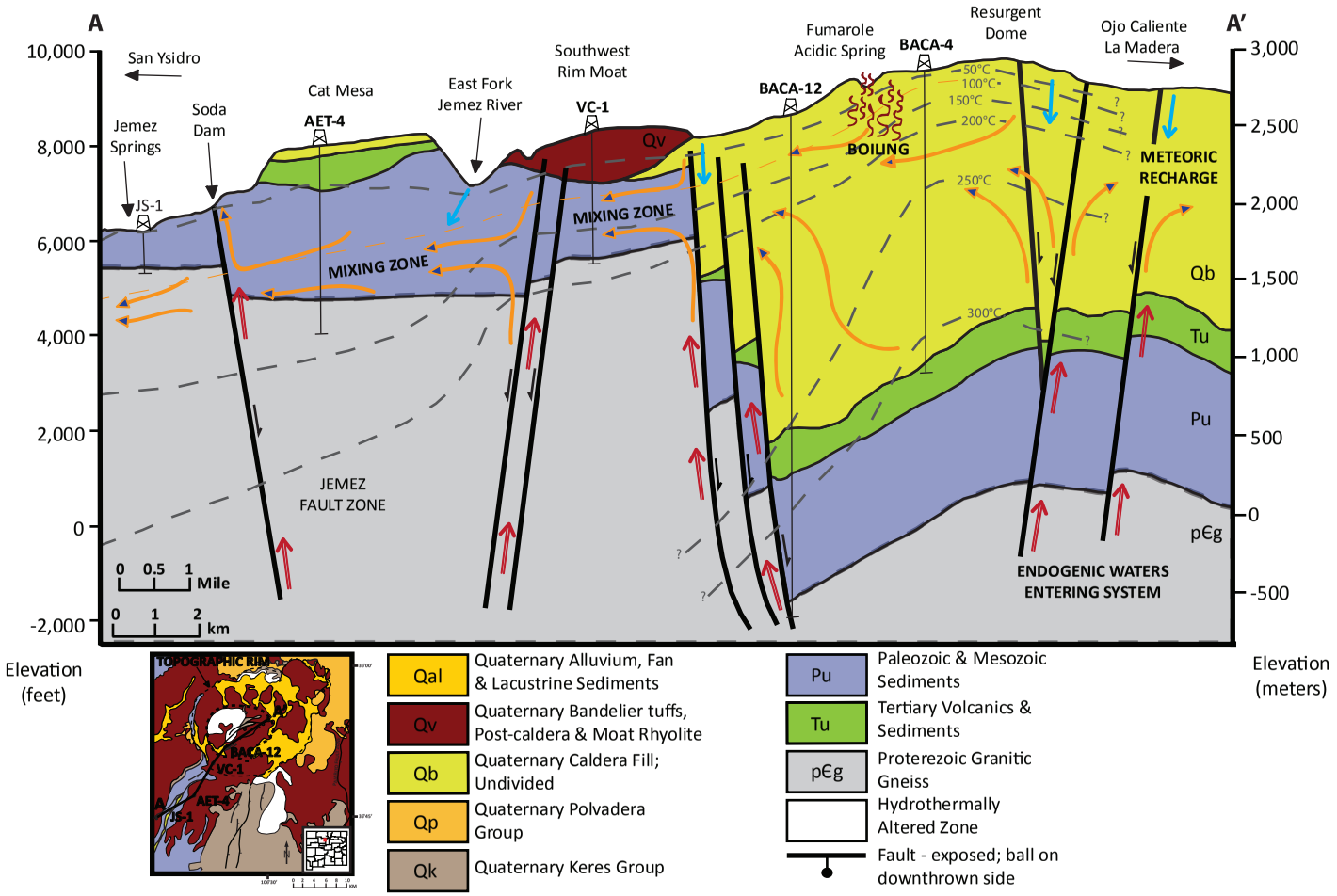

Figure 2: Schematic hydrothermal cross section (modified from Goff, 2009) depicting endogenic waters entering the hydrothermal system via faults (red arrows) and mixing (orange & blue arrows) with the meteoric waters (blue arrows). The hydrothermal waters are heated at depth and convected up where they flow down the Paleozoic aquifer units, mixing with meteoric waters along the way, through the Jemez Fault Zone in San Diego Canyon. A portion of these waters discharge at Soda Dam hot springs and deposit travertine.

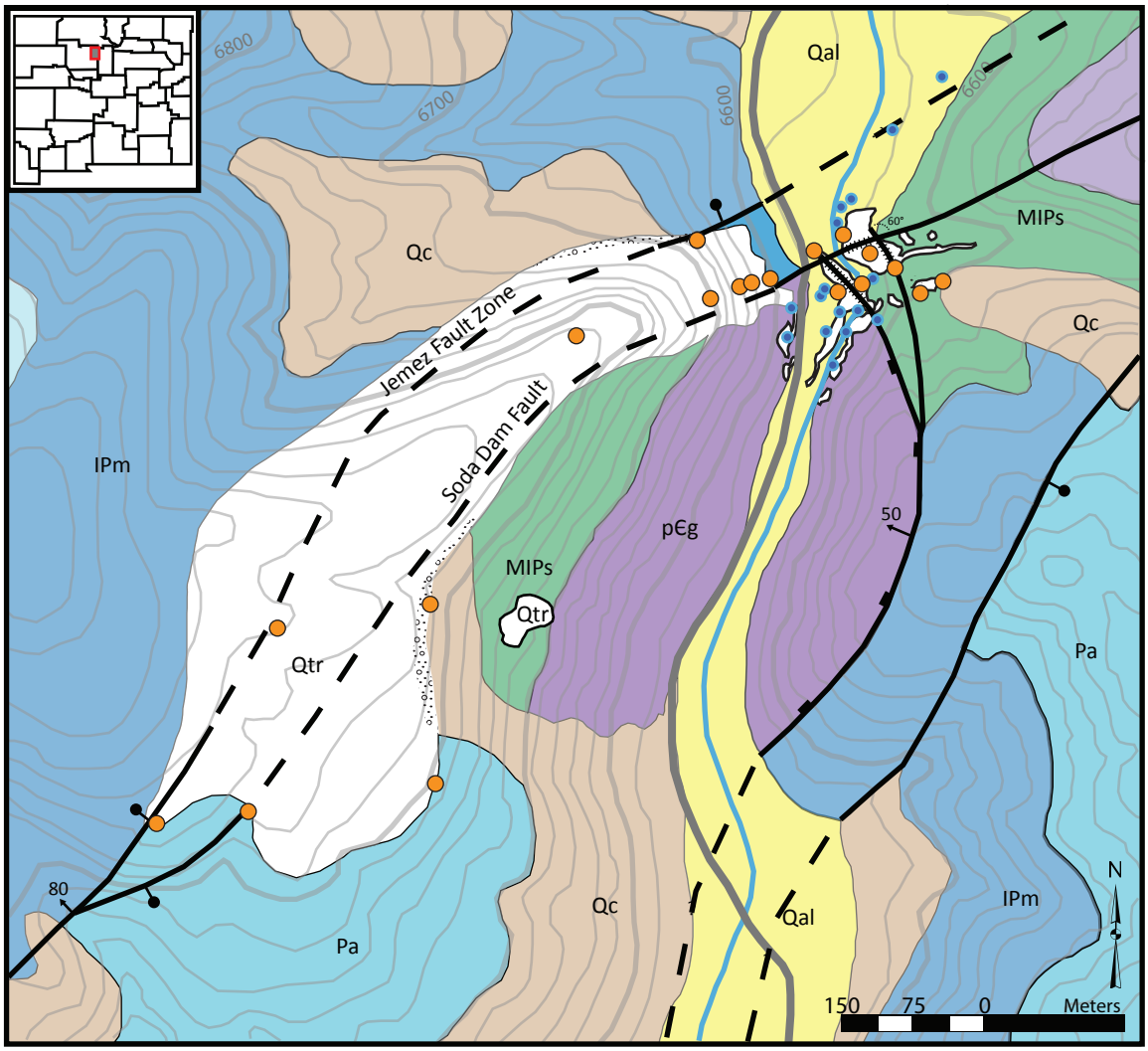

Qtr	Travertine Deposits - Middle Pleistocene to Holocene
Qc	Undivided colluvium - Middle Pleistocene to Holocene
Qal	Alluvium - Holocene. Undivided fluvial gravel, sand silt and clay
Pa	Abo Formation - Permian: Sandstone
IPm	Madera Formation - Pennsylvanian: Limestone
MIPs	Arroyo Penasco, Log Cabin and Sandia Formations Mississippian - Pennsylvanian: Undivided
pЄg	Proterezoic Granitic Gneiss

Symbols

- Spring
- Gravel contact
- Sample location
- Fault - not exposed
- Fault - exposed; ball on downthrown side
- Reverse Fault - exposed; square on upthrown side
- Travertine Feeder Veins

Figure 3: Localized geologic map of the Soda Dam study area (modified from Goff et al., 1980; Kelly et al., 2003; and Moats, 2004) depicting locations of the five travertine deposits, as well as major faults that act as subsurface conduits, channeling the hydrothermal plume through San Diego canyon.

analysis of the extensive and well-preserved travertine record provides insights into understanding the longevity and potential episodicity of the hydrothermal and meteoric systems.

Measured ratio's and composition of carbon ($\delta^{13}C$) and oxygen ($\delta^{18}O$) isotopes in the travertine can be utilized to trace the origins of the carbon and water within the system, and to provide constraints on the deposition conditions through time (Minissale et al., 2002; Crossey et al. 2009;2011). Isotopic variations within the travertine deposits at Soda Dam record influences of geothermal activity, source water and temperature variation, and possibly regional climate change. Endmember $\delta^{13}C$ values of the travertines, as well as hydrothermal and magmatic gases from the Valles Caldera and hot springs at Soda Dam indicate the input of mantle derived fluids and gases. Isotopic composition of modern samples associated with active springs allows for exploration of equilibrium deposition.

The goals of this paper include providing precise U-series ages and accumulation rates of the travertine deposits at Soda Dam, shedding light on paleohydrologic conditions within the Jemez hydrothermal system, examining bedrock incision history of San Diego Canyon, and to discuss conditions of modern and past travertine deposition using stable isotopes. The combined data are significant regionally in terms of providing one of the best records of episodic hydrothermal groundwater discharge as affected by both caldera lakes and climatically wet periods in one of the most volcanically active regions of the Southwestern United States. The Jemez hydrothermal system is comparative in chemistry and isotopic composition to hotspots and volcanically active regions such as the Galapagos (Ecuador), Kilauea (Hawaii, USA), Yellowstone (Wyoming, USA), the Apennine region (Italy), Pamukkale (Turkey), and the French Massif Central (Allier Valley, France). Chemistry, isotopic composition and landscape position of the travertine deposits at Soda Dam can be used to interpret variations within, and the evolution of the Valles Caldera hydrothermal system comparatively with other systems.

BACKGROUND ON TRAVERTINE FORMATION

Travertine deposits are nonmarine chemically precipitated carbonates that form in or near terrestrial springs and other limnological features (Fouke et al., 2000; Pentecost, 2005). Travertines have been categorized in various ways placing emphasis on temperature, hydrologic setting, texture and process (Pentecost, 2005). The term travertine will be used here in the broadest sense, to include all carbonate surface deposits whose precipitation has resulted through the transfer of carbon dioxide (CO_2) from a groundwater source leading to calcium carbonate supersaturation and the occurrence of carbonate mineral growth in a variety of depositional environments associated with CO_2 degassing (Pentecost, 2005).

Travertine deposition involves acquisition of solute in groundwater from the host rock, usually through dissolution due to excess CO_2 (carbonic acid, H_2CO_3 when dissolved), the aqueous transport of the dissolved solutes through the aquifer system and the deposition of travertine (usually as calcite, $CaCO_3$) at a discharge location (Crossey et al., 2009; 2011). This process is represented by the following reaction (Pentecost, 2005):

RXN [1] $CO_{2(g)external} + H_2O + CaCO_{3(limestone)} \rightarrow Ca^{+2}_{(aq)} + 2HCO_3^-{}_{(aq)}$

RXN [2] $Ca^{+2}_{(aq)} + 2HCO_3^-{}_{(aq)} \rightarrow CaCO_{3(travertine)} + CO_{2(g)} + H_2O$

Endogenic waters, or fluids that are derived from depths below the shallow aquifer, are typically associated with basement penetrating faults that provide conduits for the deeply sourced fluid to enter the shallow water system and mix with the fresh surface recharge (meteoric water). Endogenic waters associated with voluminous travertine deposition are highly charged with CO_2, which provides the ability to corrode carbonates along the flowpath and amass a large dissolved calcite load which partially neutralizes acidic pH and increases the concentrations of calcium, magnesium and the alkalinity of the groundwater (Crossey et al., 2006; 2009). When water that is highly charged with CO_2 and transporting an excess of solute becomes exposed to the lower

P_{CO2} of atmosphere, it degasses CO_2 to equilibrate, and precipitates travertine (RXN [2] above, Minissale et al., 2002; Crossey et al., 2006; 2009). The volume of travertine precipitated is controlled by the amount of external CO_2, availability of meteoric water, spring discharge rate and geometry, as well as faults and fractures that allow for circulation of CO_2-rich endogenic waters (Pentecost, 2005; Gilbert et al., 2009, Hancock et al., 1999).

Sources of the external CO_2 gas necessary for large volume travertine deposition are sometimes attributed to biological respiration and the subsequent accumulation of soil CO_2 due to microbial activity as well as transpiration of plants (Chafetz and Folk, 1984; Pentecost, 2005). However, other workers have emphasized that the high concentrations of CO_2 and other trace gases measured in travertine-depositing springs likely ascend along faults via seismic activity, suggesting a connection between travertine and tectonics (Hancock, 1999; Crossey et al., 2009; 2011).

In particular, the presence of high $^3He/^4He$ ratios in many travertine-depositing springs indicates the presence of volatiles that were derived in part from the mantle (Goff et al., 2002; Crossey et al, 2011). In the Jemez hydrothermal system, high $^3He/^4He$ indicate that up to 75% of the helium in some springs is derived from the mantle, implying the much of the CO_2, the inferred carrier gas for the helium, may also be of mantle origin (Ballentine et al., 2002; Crossey et al., 2011). The $^3He/^4He$ ratio is measured at the spring vent and normalized relative to air ($R_A = 1.4 \times 10^{-6}$). Elevated R/R_A values (above 0.1 R/R_A) are a clear indication of mantle-derived fluid; the majority of ^3He was produced during the formation of Earth and retains high concentrations within the mantle, while ^4He is a product of radioactive decay (U-Th series) and therefore concentrated in the crust (Ballentine et al., 2002). Springs at Soda Dam emerge with dissolved gasses carrying a primordial ^3He signature, likely released from the mantle through basalt injections that replenish the Bandelier magma chamber which resides approximately 5 km beneath the Valles Caldera (Goff et al., 2002; Crossey et al., 2009). Mantle derived CO_2 comprises the external CO_2 from RXN[1], allowing large volumes of travertine to be deposited when meteoric conditions supply the

system with recharge water. This mature hydrothermal system remains active today, with primordial ^{3}He signatures that confirm a mantle connection.

Travertine can deposit in a wide variety of morphologies and lithologies, including finely banded laminations capable of preserving a continuous record of chemical and isotopic fluid composition (Pentecost, 2005). Travertine deposits offer rich opportunities to investigate depositing waters, including variations in temperature, mixing ratios and chemistry of the source water, as well as water flux within a system through time (Crossey et al., 2009; Minissale et al., 2002; Fouke et al., 2000).

STABLE ISOTOPES: PRESENT INDICATORS OF PAST HYDROLOGIC CONDITIONS

When CO_2 (external CO_2 of RXN [1]) becomes the carbon component in travertine, the $\delta^{13}C$ value can be used to distinguish between different sources of CO_2 based on global and local proxy values as well as indicate thermal, magmatic and metamorphic influences (Minissale et al., 2002; Crossey et al., 2011; Kele et al., 2011). The $\delta^{13}C$ value of travertine depends upon the $\delta^{13}C$ value of the primary carbonate (Madera limestone) and the $\delta^{13}C$ value of contributing CO_2 endmembers. Contributing CO_2 endmembers have distinct isotopic signatures including; 1) marine carbonates acquired through dissolution along the flow path (C_{carb} = -4.4±1.2‰, Goff et al., 1987); 2) organic carbon input through biological respiration and soil gas (C_{org} = -28‰, Sharp, 2005); and 3) endogenic inputs produced/stored in the crust and/or mantle (C_{endo} = -3 to -5‰) (Crossey et al., 2011). Many springs in Northern New Mexico have enriched $\delta^{13}C$ values, suggesting a flux of endogenic CO_2 into the region; springs at Soda Dam emerge with a $\delta^{13}C$ value of -4.9‰ (Crossey et al., 2011).

Under equilibrium conditions the $\delta^{18}O$ measured within calcite is dependent upon the $\delta^{18}O$ value of the source water and the temperature of deposition. Measured $\delta^{18}O$ values from calcite, as well as measured or assumed $\delta^{18}O$ value of the depositing water, can be used to calculate a temperature of deposition based upon temperature dependent calcite-water oxygen isotope fractionation (Lachniet, 2009; Demény et al.,

2010). The isotopic composition of the source water is heavily dependent on global climatic systems, as well as regional changes in precipitation sources.

Distinct isotopic signatures create consistent, traceable spatial variation within global $\delta^{18}O$ precipitation values (source water) that reflect latitude, altitude and moisture source (Lachniet, 2009). The effects of seasonality, or variation between summer and winter moisture sources, can produce an annual dramatic shift in the average $\delta^{18}O$ value (O'Brian et al, 2006; Lachniet, 2009). Seasonality shifts play an important role in the Jemez Mountain region as recharge is dominated by winter precipitation, which is derived from Pacific storm tracks and depleted ($\delta^{18}O$ = -11‰) relative to summer monsoon precipitation ($\delta^{18}O$ = -2‰), which is derived from the Gulf of Mexico and Gulf of California (Asmerom et al., 2010). On paleoclimate timescales, seasonality shifts are difficult, if not impossible to detect, affecting the use of temperature dependent proxy models.

Stable isotope composition of travertine can be affected by fractionation that occurs during deposition and within the carbonic waters. The $\delta^{18}O$ value of the source water can be affected by phase changes associated with the hydrologic cycle that can cause variation in the isotopic ratio (fractionation) due to equilibrium and kinetic processes (Lachniet, 2009). Fractionation can occur in a variety of ways when an isotopically lighter molecule is preferred in one phase over another, relative to the isotopically heavy molecule, during processes such as evaporation, diffusion, as well as dissociation and biological reactions (Minissale et al., 2002). For example, lighter isotopes of oxygen diffuse faster than heavy isotopes due to differences in velocity (Sharp, 2007).

Travertine deposition and the resulting $\delta^{18}O$ value can be then influenced by kinetic non-equilibrium factors that are dependent on spring temperature, water cooling rates, flow path and deposition morphology, rate of travertine precipitation, evaporation, mineralogy of the host and precipitate rocks, CO_2 quantity and degassing rates as well as microbial activity (Zhang et al., 2001; Minissale et al., 2002; Hori et al., 2009; Sun et al., 2010, Demény et al., 2010, Kele et al., 2011). Kinetic fractionation

within travertine commonly occurs during rapid degassing; slowly precipitated carbonates are more likely to be in equilibrium (Sharp, 2007, Demény et al., 2010). Different species of carbon within the solution (CO_3^{-2}, HCO_3, H^2CO_3, and CO_2) contain different isotopic compositions of oxygen while in equilibrium with water (Demény et al., 2010). When rapid precipitation occurs, carbonate ions are removed from solution before isotopic exchange and equilibrium is reached between the precipitating carbonate and the solution. Variables such as degassing rate and morphology are more controlled when deposition occurs within laminated fissure vein systems, such as the Devil's Hole Record or drip deposits, such as speleothems, allowing for a more accurate reconstruction of deposition temperatures through time.

Solutions with an alkaline pH exhibit lower fractionation values for equilibrium deposition as oxygen isotope exchange differs between species, whose dominance is controlled by pH; degassing of CO^2 causes decomposition of HCO_3 which is enriched in ^{18}O relative to CO_3^{-2} (Dietzel et al., 2009; Demény et al., 2010). When travertine is precipitated in disequilibrium conditions the measured $\delta^{18}O$ values may not reflect the meteoric signature of the source water or temperature of deposition (Lachniet, 2009; Kele et al., 2011).

In extreme geologic environments, such as hydrothermal systems, water-rock interaction, boiling, non-equilibrium surface evaporation and subsurface gases can modify the meteoric signature (Vautaz et al., 1986; Clark, 1997). Isotope exchange with CO_2 has shown to deplete the $\delta^{18}O$ signal of a water reservoir relative to the local meteoric water line, while high temperature exchange with rocks can enrich the $\delta^{18}O$ (Clark, 1997; Kele et al., 2011). Discharge from carbonate aquifer units, such as the Madera limestone, which hosts the Valles Caldera hydrothermal water, can exhibit extreme disequilibrium from meteoric waters at high temperature (Clark, 1997). Previous studies conclude that all of these isotopic modifications are present in the fluids sampled from various wells and springs within the Valles Caldera hydrothermal system (Vautaz et al., 1986).

BACKGROUND: GEOLOGIC AND HYDROLOGIC SETTING OF THE SODA DAM SYSTEM

The travertine deposits of Soda Dam, particularly the iconic Soda Dam itself, are a popular tourist attraction with cultural significance for local Native American communities. The deposits are situated along NM Highway 4, which follows the Jemez River through San Diego Canyon in the Jemez Mountains. The volcanic Jemez Mountains contain an array of basaltic through rhyolitic rocks, but are most widely recognized for the huge caldera forming eruption events that took place 1.62 and 1.25 Ma, creating the Valles Toledo and Valles Caldera, respectively. These eruptions produced approximately 2,000 km^3 of erupted material in the Jemez volcanic field (Goff, 2009).

The Jemez Mountains occur within a complex, geologically active region of the Colorado Plateau; the Jemez Volcanic Lineament containing the 15 Ma – 40 ka Jemez volcanic field, and the extensional Oligocene to Miocene Rio Grande rift, both active throughout the Quaternary, intersect near the SW rim of the Valles Caldera, which developed on a NE-trending fault that now transects the center of the caldera (Figure 1). This region straddles a convergence zone within the asthenosphere and Proterozoic lithospheric mantle, where deep mantle upwelling occurs (Crossey et al., 2009).

Soda Dam is located 3 km and 1000 m down the elevation gradient from the Valles Caldera, in the single surface outlet that drains the high elevation watershed (Figure 1). This outlet, San Diego Canyon has been incised by the Jemez River, exposing rock layers of the Sierra Nacimiento Laramide highland (Kelly et al., 2007). San Diego Canyon has served as a drainage outlet for the headwaters that form within the Valles Caldera since the Pliocene; the paleo-canyon's axis is positioned west of the modern canyon (Figure 4; Kelly et al., 2007). The paleo-canyon was filled with San Diego canyon tuff 1.85 Ma, but continued to incise on the western paleo-axis as indicated by gravel deposits between the San Diego Canyon tuff and the Otowi member (lower) of the Bandelier tuff flow which capped the landscape 1.61 Ma (Kelly et al., 2007; Goff, 2009). River gravels are preserved in several locations between the Otowi Member and the

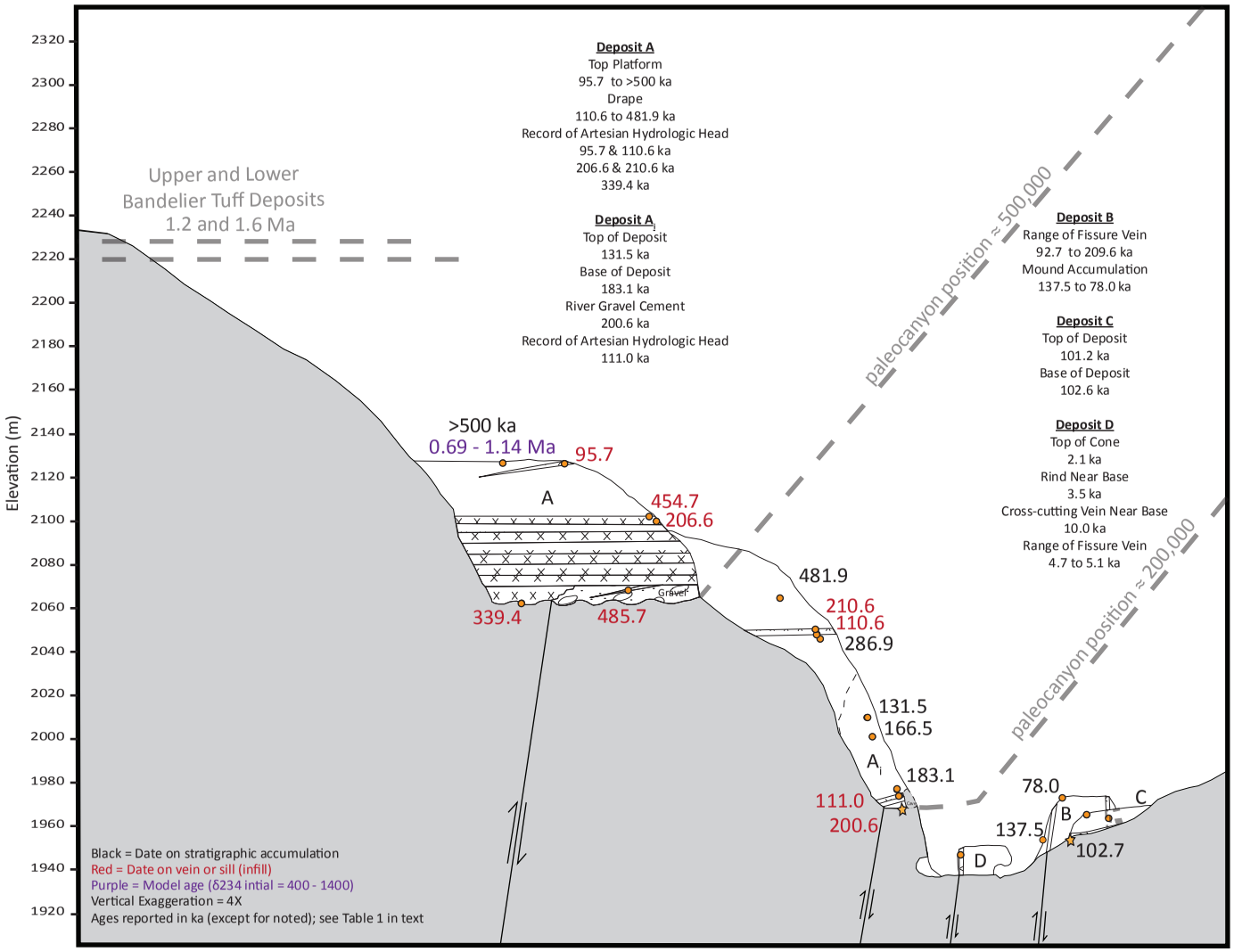

Figure 4: Schematic profile of San Diego Canyon depicting elevations and ages of travertine samples (Table 2) as well as paleocanyon positions resolved through U-series dating of travertine cemented river gravels.

Tshirege Member (upper), 1.25 Ma, of the Bandelier tuffs. One of the drainages that developed as a result of the evolving landscape was in modern San Diego Canyon; river gravels are preserved between the Bandelier tuff Members near Jemez Springs, just south of Soda Dam (Figure 1; Kelly et al., 2007). It is the post 1.25 Ma re-incision history of San Diego Canyon that has been recorded by travertine deposits at Soda Dam.

Shortly after the upper Bandelier Tuff eruption the newly formed Valles Caldera filled with water, forming the first paleo-lake, which occupied the caldera for an undetermined amount of time before draining, likely due to the resurgent dome rising at a rate of 0.1 ft/year for 30 Ka (Fawcett et al., 2007; Goff, 2009). Small, rhyolitic eruptions blocked surface drainage, and several lakes formed again around 0.8 Ma, whose depth and duration are unresolved, in the zone between the resurgent dome and the caldera rim (Fawcett et al., 2007; Goff, 2009). As volcanic influences were shaping the hydrologic system within the caldera, the east fork of the Jemez River cut through tuff and deeper stratigraphic layers as the region was uplifted, re-incising San Diego Canyon until 0.56 and 0.52 Ma when the San Antonio and South Mountain dome rhyolitic eruptions blocked surface drainage through San Diego Canyon (Goff, 2009; Fawcett et al., 2011). The South Mountain dome rhyolite successfully dammed the Jemez River and a large, relatively persistent lake formed in the Valles Grande for at least 189 ka. The lake history, from 0.52 to approximately 0.36 Ma, has been well documented from an 82 m lacustrine sediment core known as VC-3 (Fawcett et al., 2011). The last eruption series in the Jemez Mountains is known as the El-Cajete, finished by the Banco Bonito lava flow at 40 ka which blocked the east fork of the Jemez River, forming a short lived lake in the Valles Caldera a final time (Goff, 2009).

Surface and subsurface water, and hence deposition of travertine at Soda Dam, is tectonically controlled by the northeast trending precaldera JFZ which acts as a subsurface conduit within the semi-permeable Paleozoic aquifer units, channeling hydrothermal and meteoric waters through San Diego canyon (Figures 2, 3). The JFZ is the main subsurface feature controlling drainage; the Pajarito Fault Zone to the northeast acts as a barrier as opposed to a conduit for the hydrothermal waters (Vautaz

et al., 1986; Figure 1). The JFZ is locally a prominent surface tectonic feature of the Jemez lineament; the rift-related normal fault offsets Pennsylvanian-Permian rocks 200-250 m and the upper Bandelier Tuff 15 m west of Soda Dam; offset decreases to the northeast (Kelly et al., 2007). The oldest rock, approximately 1.7 b.y. granite gneiss which is the basal contact of the 1.35 b.y. "Great Unconformity," is exposed on the footwall of the JFZ at Soda Dam (Kelly et al., 2007). This Proterozoic gneiss provides an upper constraint on the JFZ, as the foliation strike in the gneiss is at high angle relative to the stike of the JFZ (Kelly et al., 2007). The resurgent dome within the caldera is dissected by numerous normal faults that are on trend with the JFZ, suggesting tectonic influence of pre-caldera rift faults (Goff et al., 1982).

The largest water reservoir in the modern Valles Caldera occurs in the subsurface caldera fill tuff and associated sedimentary rocks (Goff et al., 1994). Stable isotope analysis reveals δD values that are consistent with the meteoric recharge within the Valles Caldera (Heiken et al., 1990). Surface water travels from the high elevations of the rhyolitic "moat" surrounding the 22 km diameter caldera, as well as from the resurgent dome, where it then infiltrates as recharge or joins one of the four streams, which combine to form the Jemez River and flow towards the Rio Grande River via San Diego Canyon (Vautaz et al., 1986). The subsurface reservoir is liquid dominated; the meteoric recharge infiltrates to depths of 2-3 km where it is heated by the Bandelier magma chamber to temperatures >300°C and mixed with CO_2-rich endogenic fluids that rise within the complex fault system from depth (Figure 2; Heiken et al., 1990; Goff et al., 2002). The thermal waters rise convectively to 500-600 m in depth and migrate down gradient through the JFZ and local aquifer units (Heiken et al., 1990). Previous work concluded that the reservoir fluids sampled from the Valles Caldera hydrothermal system mix with waters that have magmatic and endogenic endmember signatures (Goff et al., 2002). Input of magmatic water affects both the δD and the $\delta^{18}O$ values; the estimated composition of magmatic waters is $\delta^{18}O$ = 6 to 9‰ and δD = -40 to -80‰ (Clark, 1997). Isotopic values of $\delta^{18}O$ and δD measured from the fluids of the Jemez hydrothermal system are enriched relative to the meteoric water line, suggesting a

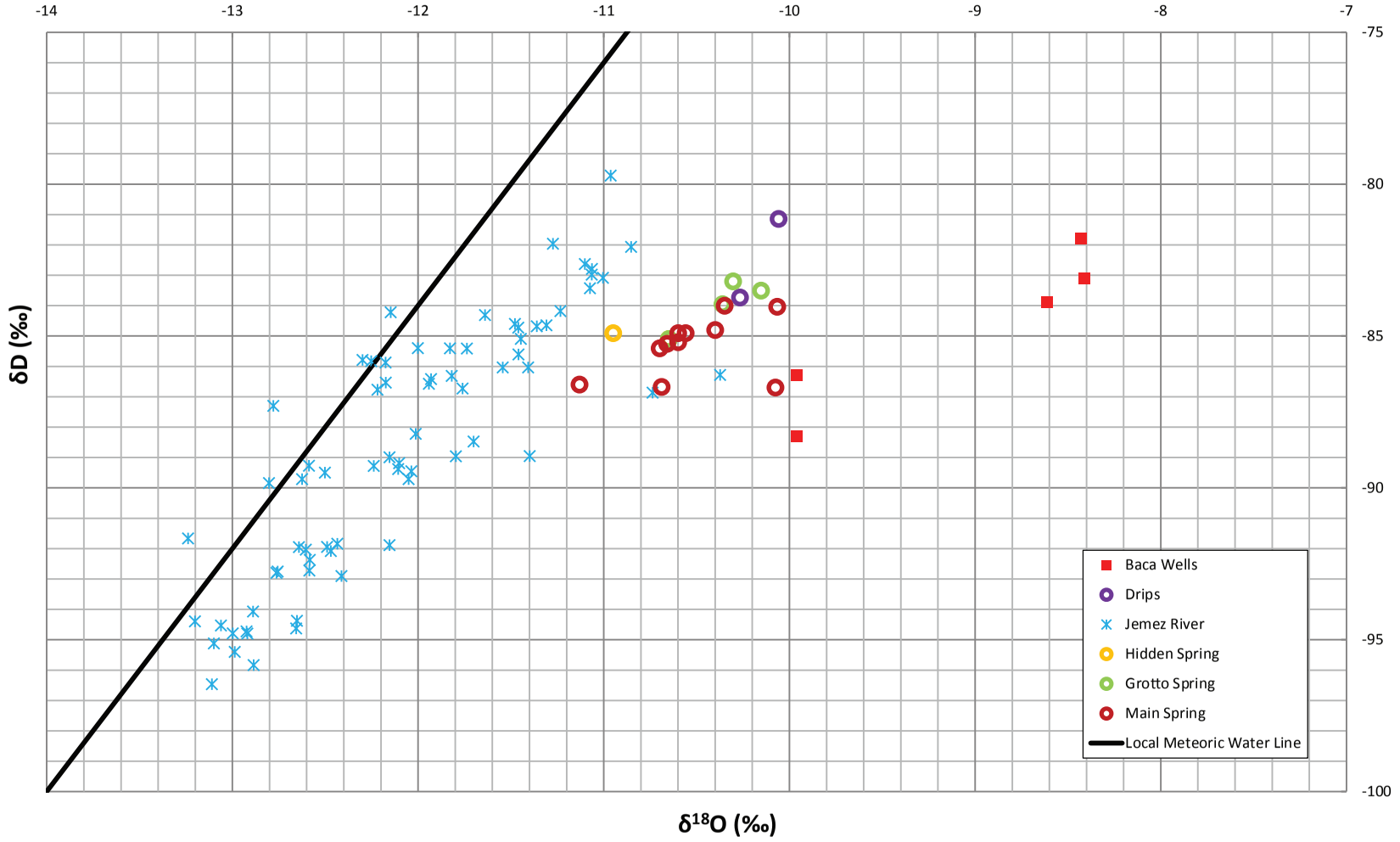

Figure 5: Stable isotope graph, δD vs. δ18O (‰, SMOW) of Baca Wells, Jemez River and fluids at Soda Dam (Table 1). Soda Dam fluids plot as a mixture of hydrothermal and meteoric waters. Local meteoric water line from Vautaz et al., 1986.

magmatic and/or endogenic input, as well as high temperature exchange with source rocks (Vautaz et al., 1986; Figure 5).

The Soda Dam and the localized area contains approximately 20 thermal and non-thermal springs and seeps that actively deposit travertine; the largest deposits on the western and eastern walls of the canyon are inactive deposits that are not associated with active springs or seeps (Moats, 2004; Goff et al., 1987). Hot springs and fumaroles that manifest along fault systems to the north and south of the Valles Caldera reveal chemical compositions that are consistent with the fluid and gas composition of the hydrothermal waters sampled during exploratory drilling (Vautaz et al., 1986; Goff et al., 2002). Five subsystems exist within the Jemez Mountain hydrothermal system, all with distinct, traceable chemical characteristics; cold groundwaters, thermal meteoric waters, acid-sulfate waters, deep geothermal and derivative waters, and Precambrian pore fluid (Vautaz et al., 1986). Deep reservoir fluids that have been encountered by the Baca wells in Redondo Creek Graben and at Sulphur Springs are chemically analogous with respect to ratios of conservative tracers (B/Cl, Br/Cl and Li/Cl) of the fluids discharged by hot springs at the Soda Dam location (Goff et al., 1994). These waters are classified as neutral pH-chloride, with concentrations of Na + K exceeding Ca + Mg, high concentrations of SiO_2, as well as As, B, Br, Cs, Li, Rd and a suite of other trace elements (Goff et al., 1994). Total dissolved solids (TDS) averages at 7,000 mg/L; the waters are heated at depth to approximately 220° to 300°C (depending on depth of circulation) and are isotopically enriched in $\delta^{18}O$ (Vautaz et al., 1986; Goff et al., 2002). Tritium data suggests ages of 60 and 10 ka, and a mean residence time of approximately 3 to 10 ka for the deep reservoir fluids (Goff et al., 1994).

Temperatures of the springs at Soda Dam have been recorded as relatively constant; the main hot spring on the west side of the highway emerges at approximately 47°C and the “Grotto” spring, bubbling up inside deposit D, emerges at approximately 27°C, with greater variation than the main hot spring, discharging water at 38°C (Shevenell et al., 1987; Figure 3; Table 1). Various other hot and cool springs emerge around the base of the Soda Dam deposits; the two mentioned discharge the largest

volume. Springs at Soda Dam have a $\delta^{13}C$ of -4.9‰, $CO_2/^3He$ ratio of 418 x 10^9, R_C/R_A value of 0.84 and a percent mantle helium value of 10.5 (Crossey et al., 2011). Endogenic water sources are characterized in the Southwestern United States by having high $^3He/^4He$ ratios, high amounts of dissolved CO_2, high alkalinity, low pH, high salinity, and high trace elements such as uranium and arsenic relative to shallow aquifer or surface recharge water (Crossey et al., 2009). These endogenic waters, although usually minor by volume in contribution to the surface hydrologic systems, can cause deterioration in water quality affecting the use of a fresh water resource, in this case, the Jemez River (Reid et al., 2003; Jochems et al., 2010).

Previous work on this travertine system was conducted by Goff and Shevenell (1987) established that travertine deposition at Soda Dam has been episodic for the past 1.0 Ma. Goff and Shevenell recognized three time periods in deposition; 1) high platform and micritic drape development (deposit A) on the western wall of San Diego Canyon from 1.0 to 0.5-0.43 Ma, 2) fissure ridge and mound accumulation from 107-58 ka on the eastern banks of the Jemez River (deposits B and C) and 3) deposition of the Soda Dam itself from 5 ka to present (Figure 3). We report 37 new high-precision U-series dates to improve this chronology, and produce a more detailed map using recent work of Moats (2004) and Kelly et al. (2007), as well as field mapping, to refine locations of travertine deposition, spring locations and faulting (Figure 3).

Goff and Shevenell also completed paired temperature calculations using $\delta^{18}O$ and $\delta^{13}C$ of the spring water, CO_2 (gas) and travertine to determine if the hydrothermal fluid exhibits steady state conditions. Results from 13 samples suggested agreement between the temperature calculations; 1‰ change in $10^3 \ln\alpha$ at 50°C systematically produced ±6°C change (Goff et al., 1987). A steady state system, for the last 1.0 Ma was concluded based on consistent results between $\delta^{13}C$ and $\delta^{18}O$ methods. We report isotopic composition of 79 samples that suggest non-steady state conditions as well as deposition outside of isotopic equilibrium.

The travertine deposition at Soda Dam contains a history of a river, canyon and spring system that has evolved as the canyon was incised, filled and affected by a variety

of influences, including dynamic volcanic activity, variation in local hydrologic head via the filling and draining of multiple paleo-lakes and paleoclimatic conditions that affect surface and spring discharge.

RESULTS - TRAVERTINE OCCURANCE: DISTRIBUTION, LANDSCAPE POSITION AND VOLUME

We subdivide the Soda Dam travertines into four major depositional periods and describe them from oldest to youngest. Deposit A consists of a large platform high landscape on the western canyon wall with a large micritic drape containing a multitude of cross-cutting calcite veins; Deposit A_i is a stratigraphic deposit inset into an erosional excavation at the base of deposit A; Deposits B/C accumulated on the east side of river along Soda Dam fault and represents an older analog to the modern fissure ridge/mound system; and Deposit D, the Soda Dam itself and related platform and low mounds, reflects youngest (and active) deposition in the river floodplain where construction of some deposits competes with seasonal river flooding. Figure 3 depicts a geologic map of the Soda Dam travertine deposits and Figure 4 depicts elevations of the travertine deposits in a schematic cross section of San Diego Canyon.

Deposit A is the largest deposit, in volume and extent, with layers that dip SE towards the canyon and are crosscut by numerous spar calcite dikes and sills that range 0.1 – 1 m thick. Deposit A consists of a high, older platform that caps the canyon wall, extending 0.61 km to the southwest of Soda Dam with a maximum 2,130 m elevation, an average thickness of 20 m, and an estimated travertine volume of 2.9×10^6 m^3 that overlies river gravels containing volcanic clasts at 132 m above the modern river, ash beds and upfaulted Paleozoic sedimentary rocks, all of which have been intruded by calcite veins. The older micritic cap deposited along the Jemez Fault and the Soda Dam Fault, and has been intruded by large, numerous, and quite spectacular spar sills and dikes. The north end of this deposit drapes to the east, indicating that travertine deposition was simultaneous with canyon incision, likely occurring on the banks of the paleo-Jemez River, similar to the deposition occurring at La Madera today (Crossey et al., 2011). The large, micritic drape is cross-cut by calcite sills and contains 8.25×10^5 m^3

of stratigraphic travertine approximately 90 m above the modern river; the drape of deposit A has been excavated by the Jemez river is inset by deposit A_i.

Deposit A_i accumulated 30 to 65 m above the modern river, with an average thickness of 20 m and an estimated travertine volume of 3.0×10^5 m^3. The entire deposit sits on upturned Precambrian and Paleozoic rocks, and overlies travertine-cemented river gravels approximately 30 m above the modern river. This micritic inset deposit is stratigraphic, with the oldest layer at the base, youngest at the top, and is cross cut by numerous calcite veins. A well-known, and well loved (as indicated by the large number of carabineers) climbing cave is at the base of the deposit; several cross cutting calcite sills are visible and easily accessible at this location.

Deposit B is situated on the northeast bank of the Jemez River on a small ridge of Paleozoic rocks and colluvium; maximum elevation is approximately 40 m above the Jemez River and travertine volume is estimated at 1.1×10^5 m^3. Two deep, central fissures of finely laminated spar calcite approximately 1 m wide dissect the deposit. The western fissure cuts east-west through the deposit, on trend with the Soda Dam Fault until it intersects the second fissure, near the center of the deposit, which cuts in a northeast-southwest direction, on trend with a reverse fault. Deposit C is the smallest deposit, likely a continuation of the depositional event that produced deposit B, with an estimated volume of <30 m^3. Deposit C is a micritic, stratigraphic deposit that slopes westward, towards the Jemez River with maximum and minimum elevations of 25 and 16.5 m above the river, respectively. A sill of calcite approximately 0.5 m thick is exposed near the base on the south side of the deposit, directly above river gravels at 16.5 m above the modern river.

Deposit D, the Soda Dam itself, is approximately 100 m long and 30 m wide with an estimated travertine volume of 2.4×10^4 m^3. The deposit sits on a large carbonate platform which has an estimated area of 6,000 m^2 and thickness of up to 1 m. In the past, the main spring discharged along a 0.5 m wide central fissure that dissects the deposit on an northeast-southwest axis that is on trend with the Soda Dam Fault; the main spring discharge presently occurs along the west side of NM State Highway 4 due

to damage caused within the plumbing of the structure when it was dynamited over 50 years ago for the construction of the highway (Goff et al., 1987). Two small openings on the southern side of the structure allow access to the interior of the mound; the larger of the two is the well-known Grotto spring consisting of a pool 1 m in diameter within a travertine mound covered with a veneer of microterraces. Calcite straws build daily as super saturated thermal waters drip from the ceiling above the pool. The smaller of the two openings reveals a very small cave at the base of the Soda Dam. Multiple seeps surround the base and platform, many of which deposit travertine. Underneath the mound accumulation and platform (accessible from within the river) thermal waters drip directly into the Jemez River in two "lower grottos," depositing calcite straws.

RESULTS - URANIUM-SERIES GEOCHRONOLOGY

A suite of 36 samples were selected from the deposits at Soda Dam for precise U-series dating (Appendix A). Samples were dated to constrain: 1) bottom and top layers (hence durations) of the various travertine deposits; 2) samples that cemented and were interpreted to have been deposited contemporaneously with river gravels in elevated ancient terraces of the Jemez River; and 3) banded feeder vein systems that can also be used to constrain deposition durations and potentially provide continuous data for stable isotope analysis.

U-series dates on travertine at Soda Dam have provided new insight on the history of the Soda Dam and surrounding deposits. Table 2 reports both new and previously reported results, listed from oldest to youngest. Figure 3 displays sample locations, and figure 4 depicts the schematic position of the U-series dates relative to the modern topography and inferred paleo-topography.

The top, micritic platform of deposit A (LC11_NMSDA_31), sampled along the precaldera Jemez fault, yielded an unresolved age via U-series geochronology. A model based upon decay equations, assuming a range of 400-1400 $\delta 234_i$ from measured uranium concentrations within all four deposits produced a conservative age range of 0.69 – 1.14 Ma (Appendix A). Two spar samples within the high platform of deposit A

and a micritic drape sample yielded ages within error of each other at 480 and 455 ka (AJT11_SDA_51, LC10_NMSDA_24, and LC11_NMSDA_32). Large sparite intrusions yielded ages of 339 ±8.1, 211 ±3.5, 207 ±13.8 and 111 ±12.9 ka (AJT11_SDA_52, LC10_NMSDA_22b , LC11_NMSDA_34, and LC10_NMSDA_22a). A micritic drape sample, 130 m above the modern river, yielded an age of 287 ±7.0 ka (LC10_NMSDA_23a). The youngest sample within deposit A yielded an age of 96 ±7.3 ka from a cross cutting vein within the top micritic platform, 195 m above the modern river (LC11_NMSDA_30).

Deposit A_i yielded an age of 201 ±2.0 ka from calcite cemented river gravels at the base of the deposit, 32 m above the modern river (K06_SDam_2). Stratigraphic accumulation ages range from 183 ±2.1 at the base to 132 ±4.4 ka at 64 m above the modern river (K06_SDam_4; LC10_NMSDA_21). A cross-cutting sill, eye level with the cave at the base of the deposit, yielded an age of 111 ±1.5 ka (K06_SDam_1).

Deposit B, the fissured northeast deposit, yielded ages of 138.4±1.1 ka near the base, and 78.2±1.6 ka at the top of the micritic mound accumulation (LC10-NMSDB-15, LC10-NMSDB-19). The laminated central fissure yielded ages ranging from 209.6 ±1.7 ka to 92.7 ±0.5 ka (LC10-SdamB-25a-d, 1-5a). Deposit C yielded ages of 102.6±0.5 ka at the base which cements river gravels 16.5 m above the modern river, and 101.7±5 ka at the top, 25 m above the modern river (LC10-NMSDC-11, LC10-NMSDC-13).

Deposit D yielded a maximum age of 10 ±0.8 ka from a basal stratigraphic layer exposed at the road (KLC12_SD100). Ages from the central fissure vein ranged from 4,681 ±45 to 5,149 ±43 (LC10-Sdam-28 b, LC10-Sdam-28 a).

Figure 6 reports the U-series results in an age probability diagram produced by *Isoplot* 3.7, an add-in program for Microsoft *Excel 2010* for plotting radiogenic-isotope data (Ludwig, 2008). A histogram and probability distribution was calculated by summing the suite of ages and normally distributed errors; bin width was user defined as 20 ka. Periods of bulk accumulation were episodic, and well represented in the sampling suite. Approximately 77% of the travertine was deposited at or before 500 ka (possibly back to 1.2 Ma), 14% between 482 and 287 ka, 8% between 183 and 78 ka, and

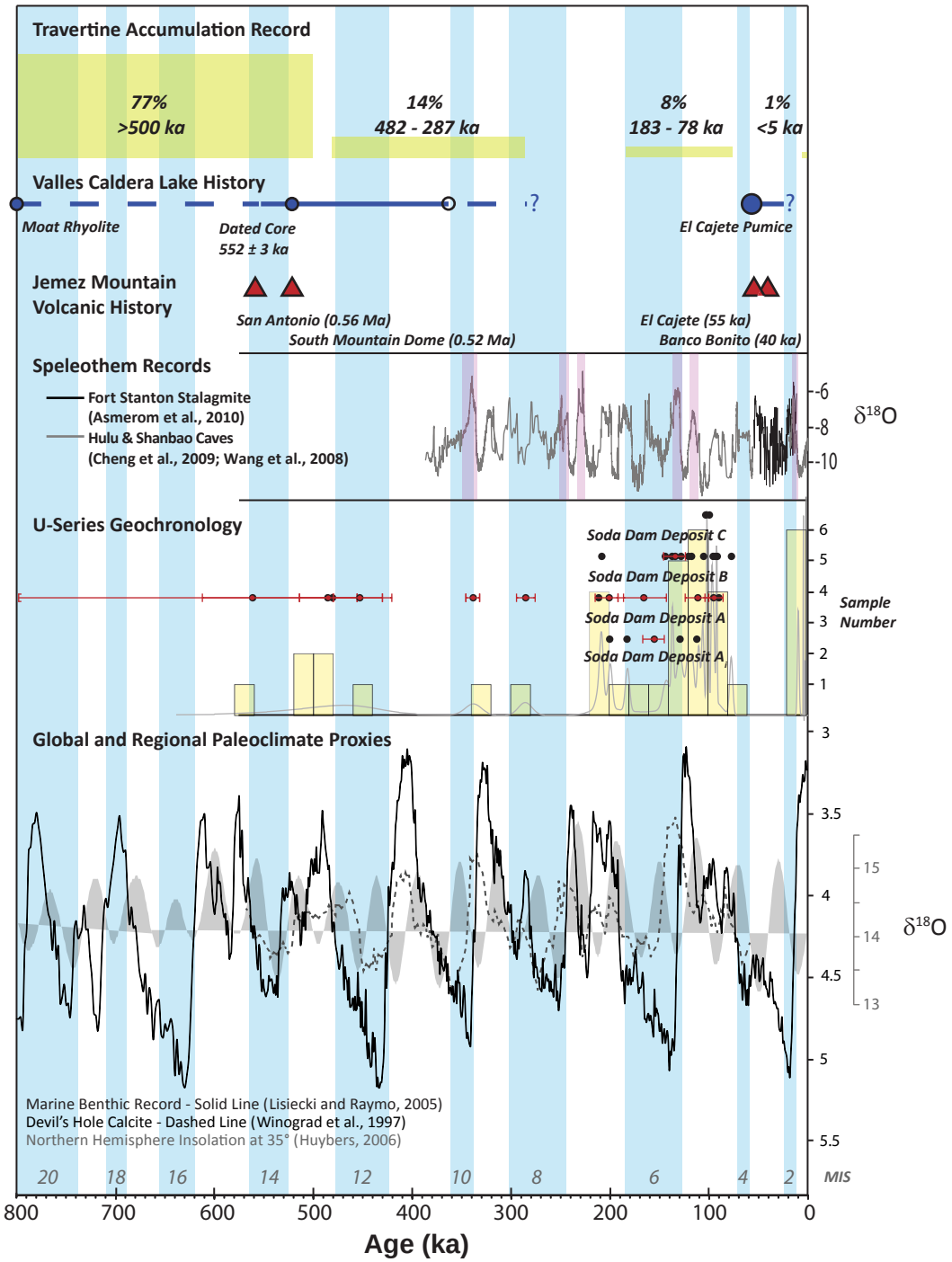

Figure 6: Timeline displaying dated travertine deposits of Soda Dam in relation to; MIS (Wright, 1999); SPECMAP marine core record (Lisiecki and Raymo, 2005); Devil's Hole calcite record (Winograd et al., 1997); Northern Hemisphere Insolation at 35°N (Huybers, 2006); Fort Stanton stalagmite record (Asmerom et al., 2010); Hulu and Shanbao Cave records (Cheng et al., 2012); WAMI (pink boxes); Jemez Mountain volcanic history and VC-3 lake core record (Fawcett et al., 2011). Probability plot displays sample frequency in yellow bars and 2σ error curve in gray; dated samples (black circle) display error bars in red, except when error is smaller than sample point.

1% from 10 ka to present (Figure 4, 6). Records of high hydrologic head have been interpreted from the young, cross-cutting calcite sills that have intruded older, micritic deposits at approximately 95, 110, 210, 340, 455 and 486 ka.

RESULTS - STABLE ISOTOPES

Stable isotope values were obtained on 27 dated, and an additional 52 undated travertines (Table 3; Figure 7). The wide range in $\delta^{18}O$ values, $\delta^{18}0$ = -19 to -4‰ (PDB), is characteristic of travertine deposits, and possibly reflects variations in local spring chemistry, temperature of deposition and facies influences (Chiodini et al., 2000; Sharp, 2007). $\delta^{13}C$ isotope values range from +1.4 to +11.7‰ (PDB); these relatively positive values suggest degassing of the light CO_2, a higher quantity of endogenically sourced CO_2 relative to organically derived CO_2 in the hydrothermal system and likely high temperature water-rock interaction.

General trends in the data include an average lighter value for both $\delta^{18}O$ and $\delta^{13}C$ in dense, cross-cutting sparitic samples as opposed to the more porous, stratigraphic micritic layers. The average $\delta^{18}O$ and $\delta^{13}C$ value of sparite is -13.64 and 3.72‰; micritic sample produce averages of -10.61 and 5.00‰. The range of $\delta^{13}C$ is 5.91‰ for micritic samples and 5.96‰ for sparite samples, while the range of $\delta^{18}O$ is larger and displays more variation at 8.39 and 12.92‰, respectively. These results suggest that facies morphology plays a role in stable isotope composition. Older samples generally plot with lighter isotope values for $\delta^{18}O$ and $\delta^{13}C$; a noticeable increase in the range of isotopic composition is evident at approximately 180 ka when data is plotted through time (Figure 8). The average $\delta^{18}O$ value pre-180 ka is -15.17‰ and increases to -9.84‰ post-180 ka; values of $\delta^{13}C$ follow a similar trend with from 6.28 to 3.17‰.

Measured $\delta^{13}C$ from CO_2 of the Soda Dam hot spring is -4.9‰; this value suggests buffering from the Madera limestone, which has a measured -4.4±1.2‰ $\delta^{13}C$ value (Goff et al., 1987; Goff et al., 2002; Crossey et al., 2011). Measured $\delta^{18}O$ values from Soda Dam and Grotto spring water have been averaged as -10.6‰ (Goff et al.,

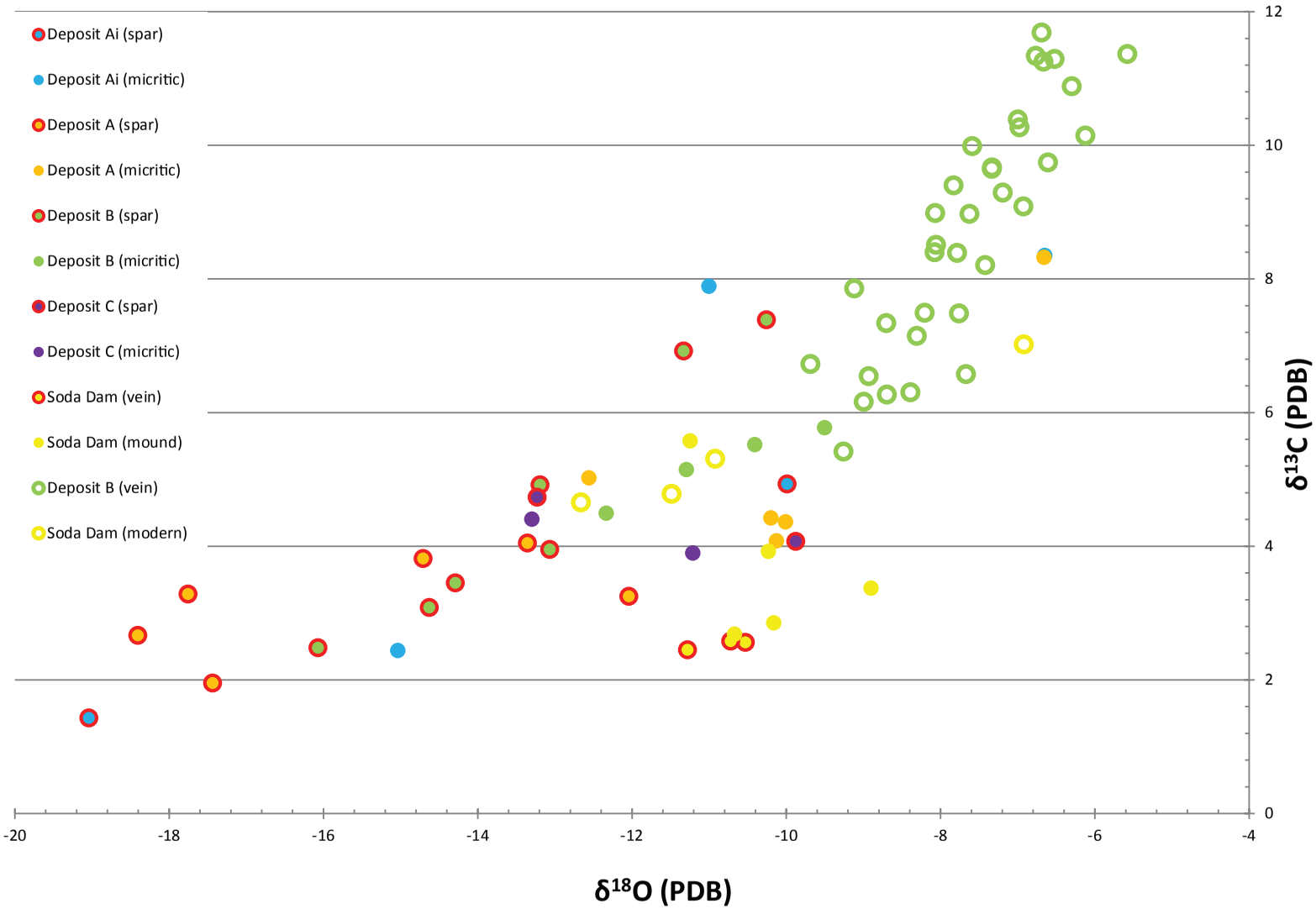

Figure 7: Stable Isotopes of carbon and oxygen from travertine samples (Table 3).

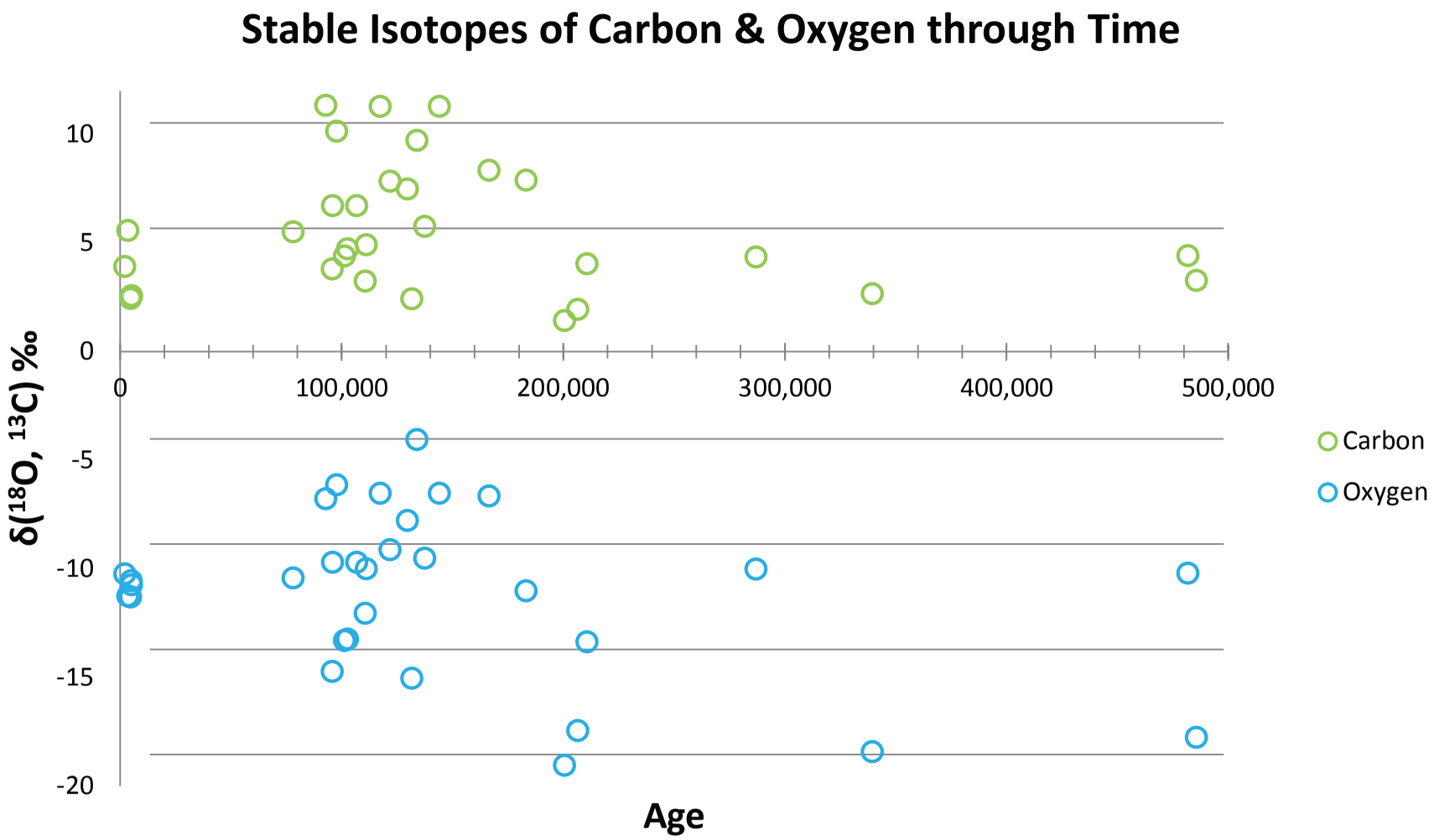

Figure 8: Stable isotopes of δ ^{18}O & $\delta^{13}C$ through time.

1987; Jochems et al., 2010; this study). Using measured isotopic values of travertine (Table 3) a sensitivity analysis was performed using relationships between fractionation factor and temperature for CO_2-$CaCO_3$ (^{13}C) and H_2O-$CaCO_3$ (^{18}O) (Clark, 1992; Romanek et al., 1992; Appendix A). Differences between $\delta^{13}C$ and $\delta^{18}O$ temperature calculations exhibited a range among the measured samples from 2.2 – 5.1 °C per 1‰ change in $10^3 ln\alpha$. Temperature variation existed solely among the measured $\delta^{18}O$ values, suggesting that a steady state conditions for source water isotopic composition for the past 500 ka is unlikely.

Deposit D is the center of the modern calcite precipitation at Soda Dam. Water samples from drips that form in the lower grottos along the banks of the Jemez River are enriched in $\delta^{18}O$, relative to main Grotto and the main hot spring, and the Grotto is enriched in $\delta^{18}O$ relative to the Main hot spring (Table 3; Figure 5). When the isotopic signature of the fluid from the Baca wells, the Soda Dam spring system and the Jemez River are plotted, a well-developed mixing line reveals the meteoric water of the Jemez River and enriched geothermal waters of the Baca well system as clear end-members, with the Soda Dam spring system plotting as a combination of the two sources (Figure 5).

STABLE ISOTOPES: INSIGHTS INTO PAST DEPOSITION CONDITIONS

Temperature of deposition was calculated using oxygen isotope thermometry based on oxygen isotopic fractionation between calcite and water. Equations, each with a slightly varying calcite-water fractionation relationship with temperature, from Romanek et al. 1992 for ^{13}C as well as Kim and O'Neil, 1997 and Demény et al., 2010 for ^{18}O were employed (Table 4). The bicarbonate-water fractionation relationship was applied as the pH of modern springs measured from 6.05 – 7.34, which infers that carbon resides as species of CO_2 (aq) and HCO_3^- (Table 3; Kele et al. 2011). Of these, the Demény et al., 2010 results are discussed as results produced temperatures closest to modern measured temperatures; the oxygen isotope fractionation factor was determined for open-air, warm to hot water travertines in a natural environment.

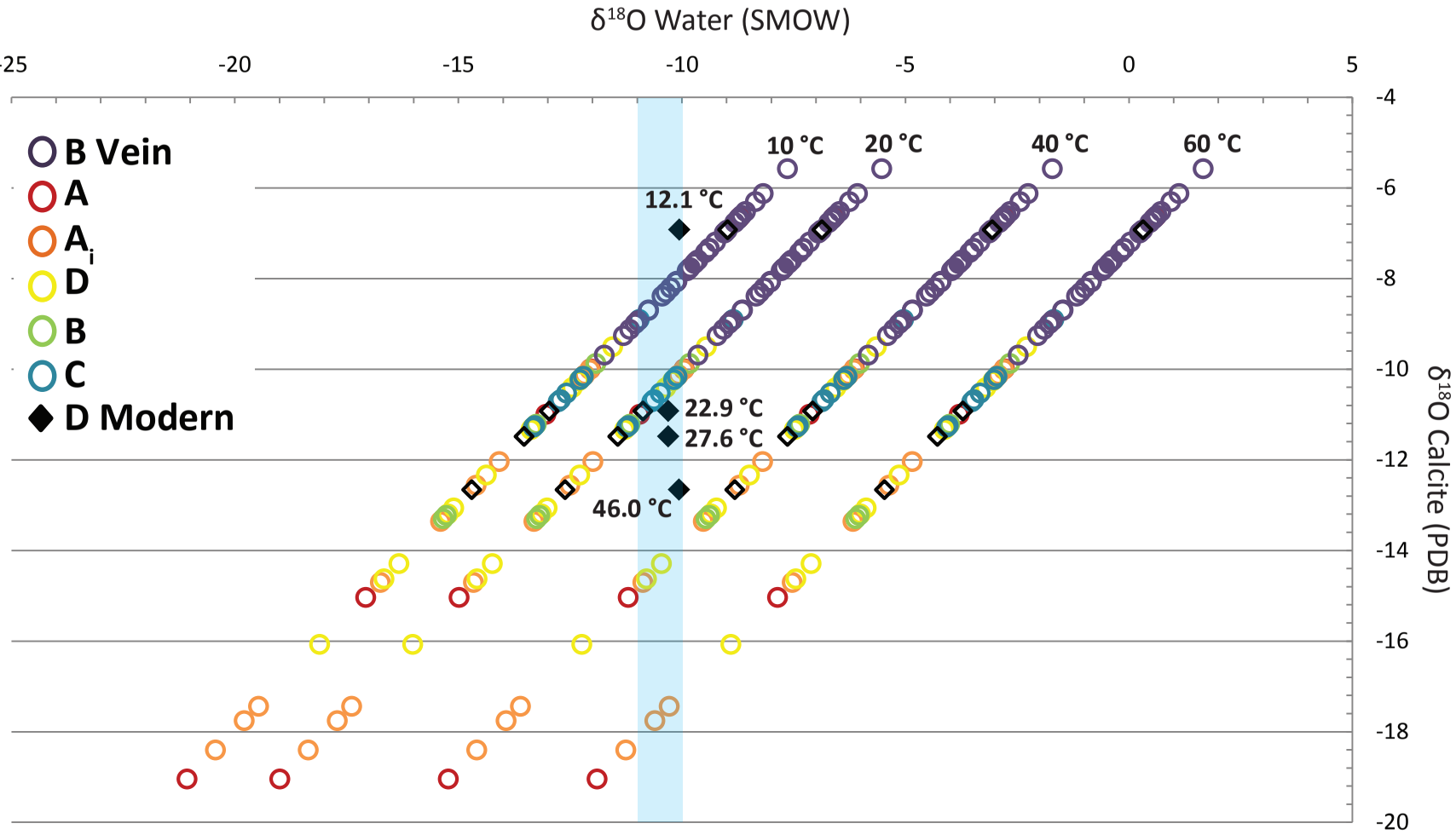

Figure 9: Calculated range of $\delta^{18}O_{water}$ values using the Demény et al., 2010 calcite-water oxygen isotope fractionation equation [$1000\ln\alpha = 17.599\ (1000/T) - 29.64$], based on measured $\delta^{18}O_{calcite}$ values for a range of modern temperatures (10-60°C) which encompass the modern temperature range of travertine depositing springs, shown in black diamonds with measured depositing temperature. Range of modern water values shown in blue.

Figure 9 displays the calculated range of $\delta^{18}O_{water}$ values from measured $\delta^{18}O_{calcite}$ values for a range of temperatures (10-60°C) that encompasses the modern temperature range of travertine depositing springs. In modern samples, where depositing temperature, as well as the $\delta^{18}O$ values for the calcite and water can be measured, kinetic enrichment of 1-2.3‰ was observed; adjustments to the measured calcite value produce measured temperatures. Considering $\delta^{18}O$ values from the laminated vein fissure is deposit B, where morphologic facies and rate of degassing is more controlled (fractionation effects less likely), calculated paleotemperatures range from -0.46 to 18.23°C. If kinetic enrichment with the same magnitude observed in modern samples occurred within this sample, the range of deposition temperatures is 3.86 to 29.90°C.

The above calculations were made assuming that the composition of the source water remained steady; a modern value of -10‰ was used. This assumption is unlikely, albeit necessary for paleotemperature calculation. The $\delta^{18}O$ value of the paleo-source water could have been enriched relative to measured modern values. Enrichment of $\delta^{13}C$ and $\delta^{18}O$ is a reasonable assumption within the Jemez hydrothermal system as increased volcanic activity, and therefore magmatic input into the hydrothermal system, could have produced heavier isotopic values of both $\delta^{13}C$ and $\delta^{18}O$ (Chiodini et al., 2000; Sharp, 2007).

RESULTS - JEMEZ RIVER INCISION RATES

Figure 4 and Table 4 present new ages and insight into post 1.25 Ma incision, allowing for the refinement of existing incision rate information in this upper reach of the Jemez River through San Diego canyon. The Jemez River drainage basin is the largest contributor to the Rio Grande on the east side of the Sierra Nacimiento with an area of approximately 1480 km^2. Fluvial incision rates are calculated as strath height above the modern channel; a strath is defined as an unconformable surface that is older than the overlying sediments.

Two studies reported long term bedrock incision rate for the lower reaches of the Jemez River, near the confluence with the Rio Guadalupe and through the Jemez River Valley to Arroyo Peñasco. Near the Rio Guadalupe confluence, the long term incision rate is 119 m/Ma over the last 1.61 Ma based upon 3 m thick buried axial gravels beneath the lower Bandelier tuff unit exposed an average of 192 m above the modern river at Virgin Mesa, Mesa de las Casas and Guadalupita Mesa (Rogers, 1996). Calculation did not include the thickness of the Bandelier tuff units as rapid incision through the tuff is assumed (Goff et al., 1987; Rogers, 1996). In the Jemez River Valley, the long term incision rate was calculated at 117 m/Ma (Formento-Trigilio et al., 1998).

Two additional well dated tephras provide longer term average incision rates; 141 m/Ma since 1.25 was obtained from 3 m gravel exposure at the base of the 1.25 Ma upper Bandelier tuff an average of 176 m above the modern river near the confluence of the Jemez River and the Rio Guadalupe and 173 m/Ma since 640 ka obtained from the top of a 21 m thick terrace deposit 111 m above the modern river containing intercalated Lava Creek B ash (Rogers, 1996). These well mapped terrace deposits associated with well dated tephras record a history of inconsistent bedrock incision throughout the Quaternary. Reported incision rates are 30-80 m/Ma between 1.61 and 1.25 Ma, 90-150 m/Ma between 1.25 and 0.64 Ma and 140-220 m/Ma from 0.64 Ma to present (Rogers, 1996). These results are congruent with regional studies have shown fluvial incision rates to increase during the late Pliestocene, between 500 and 100 ka (Formento-Trigilio et al., 1998).

Deposit A_i contains travertine rinds on river cobbles just above the bedrock strath at the cave which yielded an age of 200.6±2.1 ka (K06-SDam-2; Table 2). The strath is 30 m above the river yielding an average bedrock incision rate of 150m/Ma over the last 200 ka. Deposit C yielded an age of 102.6±0.5 ka from a calcite rind at the base, directly above river gravels (LC10_NMSDC_11; Table 2, Figure 4, 10). The bedrock strath is 16.5 m above the river, yielding an incision rate of 160 m/Ma over the last 100 ka. This suggests semi-steady bedrock incision rates over last 200 ka (Figure 10).

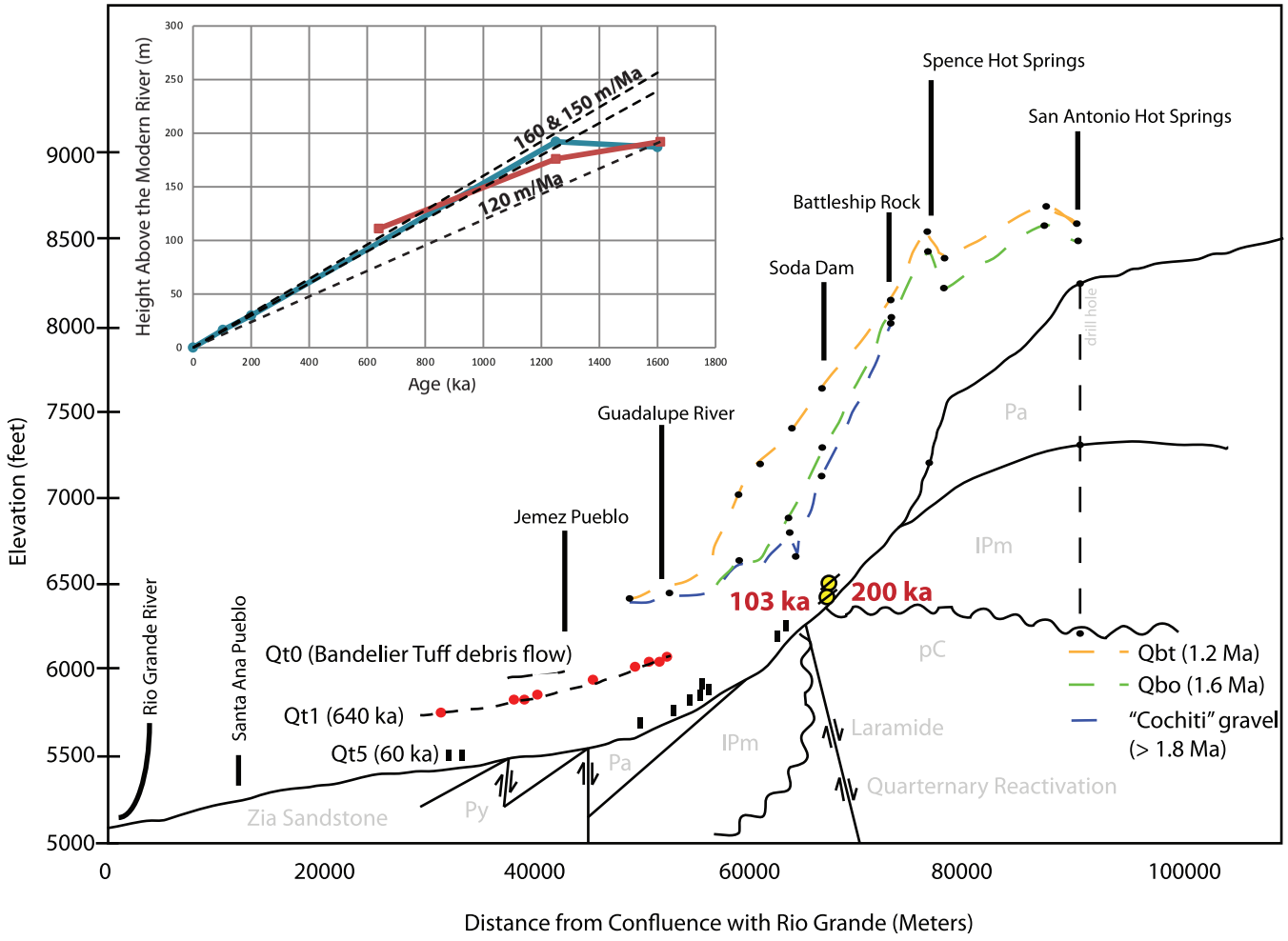

Figure 10: Modified from Cox (1995), profile of the Jemez River from San Antonio hot springs to confluence with the Rio Grande. New dated strath (yellow circles, deposit Ai) at 16.5 and 32 m above the modern river. Graph depicts long term incision rates (120m/Ma; Rogers, 1996) and new incision rates (160 & 150m/Ma). Red box is potential age range of river gravels at 132 m above the modern river. Red connected data points from Rogers, 1996; blue connected data points from this study.

At the Soda Dam location, the base of the Tshirege Member is 292 m be the modern river, producing an incision rate of 234 m/Ma for the past 1.25 Ma. Thus, our calculation of "bedrock incision" using the base of the 1.25 tuff and the modern river is a maximum incision rate. If the approximately 400 m of incision that the paleo-Jemez River must have done to incise back through the Bandelier tuff Members is included, we get a rate of about 554 m/Ma since 1.25 Ma.

River gravels are in place at the base of the older platform of the deposit A, with a strath 132 m above the modern river yielding an average incision rate of 155 m/Ma over the last 850 ka (Figure 4, 10). These incision rates are calculated assuming that the cemented river gravel strath is 850 ka, congruent with semi-steady bedrock incision rates of the Jemez River. Kelly et al., 2007 suggests that the formation and draining of several paleo-lakes in the caldera since 1.25 Ma likely prolonged an episodic river incision history in San Diego Canyon.

It is also likely that this strath is just over 500 ka as conditions for platform development occurred after the South Mountain Dome eruption blocked flow of the Jemez River, locally increasing hydrologic head and providing continuous water supply for travertine accumulation. An age of 0.52 Ma produces an incision rate of 254 m/Ma since 0.52 Ma.

Another plausible explanation assumes that older platform development began at approximately 1.1 Ma, yielding an incision rate of 120m/Ma for the past 1.1 Ma. This infers rapid incision of the Bandelier Tuff Members, as proposed by Goff and Shevenell (1987). Rapid incision of tuff units has been documented in the Valley of Ten Thousand Smokes, Alaska and Mount Saint Helens, Washington (Goff et al., 1987). Ar-Ar dating of pumice clasts within the river gravel at the base of deposit A is in progress and may improve the accuracy of this incision data point.

INTERPRETATION OF TRAVERTINE AT SODA DAM IN TERMS OF REGIONAL/GLOBAL PALEOCLIMATE RECORDS

Figure 6 displays a timeline of travertine deposition at Soda Dam, as well as regional and global paleoclimate records, including $\delta^{18}O$ values from a benthic marine

sediment core (Lisieki et al., 2005), Devil's Hole calcite (Winograd et al., 2006), northern hemisphere insolation at 35°N (Huybers, 2006), the Fort Stanton Stalagmite (Asmerom et al., 2010), Hulu Cave and Shanbao Caves (Cheng et al., 2012), as well as timing of the VC-3 lake record from the Valles Grande (Fawcett et al., 2011). We apply these proxies to our interpretations of regional wet periods capable of supplying the water limited system at Soda Dam with enough recharge to raise hydrologic head levels for high elevation calcite intrusion and large volume accumulation.

Global glacial and interglacial paleoclimate proxies are derived from $\delta^{18}O$ values recorded by forminiferal organisms within benthic marine sediment cores, which correspond to global ice-sheet volume (Imbrie et al., 1984, Martinson et al., 1987, Lieseki et al., 2005). Sea surface temperature (SST) can also be obtained from a selection of these records through the use of alkenone content (Winograd et al., 2006). Marine cores, while robust records of paleoclimate, cannot be radiometrically dated past the limits of carbon analysis and are therefore tuned to SPECMAP chronology using a variety of orbital tuning techniques based upon Milankovitch theory of eccentricity driven glacial/interglacial cycles (Imbrie et al., 1984, Martinson et al., 1987, Lieseki et al., 2005).

A well-known debate of this issue developed around Devil's Hole, a calcite vein that accumulated in a submerged, groundwater fed cave system in southern Nevada that contains a late-Pleistocene to mid-Holocene $\delta^{18}O$ record (Winograd et al., 2006). While the Devil's Hole record clearly exhibits Milankovitch theory periods of eccentricity (94 ka) and obliquity (41 ka), the debate focused around early warming of SST during the penultimate glaciation. The Devil's Hole record provides a radiometrically dated, continuous warming trend that begins 5 – 10 ka prior to SPECMAP chronology, suggesting that warming was well underway when ice sheets were at their maximum, and before a rise in Northern Hemisphere insolation (Winograd et al., 2006).

It has been established that while the early warming of SST recorded in the Devil's Hole calcite does not directly challenge Milankovitch's astronomical theory of climate change; the record is viewed as a regional signal of Pacific SST (Winograd et al.,

2006). The Devil's Hole record is not an anomaly among paleoclimate records that display an early warming, relative to SPECMAP, in the penultimate glacial (Winograd et al., 2006). Early SST warming has been demonstrated in multiple, but notably not all, low to mid-latitude benthic ocean records; several researchers have provided evidence of sea level rise prior to the peak in Northern Hemisphere insolation (NHI) (Levine et al., 2001; CLIMAP Project Members, 1984, Henderson et al., 2000; Stirling et al., 1998).

Global ice volume, or simply global warm and cold cycles, while an excellent generalized record for wet vs. dry intervals, can cause unintentional disregard of regional influences affecting the amount of precipitation an area actually receives. Variations within the recorded signals of regional, continental paleoclimate proxies on millennial and centennial timescales often serve as more precise records of wet vs. dry intervals. For the southwestern United States, a rise in Pacific SST shifts the westerly storm tracks south, creating El Niño conditions which regionally enhance winter moisture, and hence recharge (Wagner et al., 2010). The North Atlantic plays a role in this system as well; warmer North Atlantic SST causes poleward migration of the Polar Jet Stream due to a decrease in the pole to equator temperature gradient, consequently, creating arid conditions in the southwest (Wagner et al., 2010; Asmerom et al., 2010).

The strength of El Niño Southern Oscillation (ENSO), a prevalent feature of the late Quaternary, is dependent upon various teleconnections, including, but not limited to, the latitudinal position of the polar jet stream, polar temperatures, SST in the North Atlantic and tropical Pacific, fresh water input into the North Atlantic, solar activity, NHI, and pacific currents (Asmerom et al., 2010; Wagner et al., 2010; Bull et al., 2000; Winograd et al., 2006). While not the aim of this paper or ability of this dataset to defend one theory over another in master forcing's of southwestern precipitation, it is of particular interest to present evidence for travertine production timing which corresponds to events recorded in mid-latitude, continental proxies rather than the global marine record.

The North American Monsoon (NAM) and the Asian Monsoon (AM) respond to ENSO and shifts in the intertropical convergence zone (ITCZ) inversely and can thus be used as proxies for one another (Asmerom et al., 2006:2010; Wagner et al., 2010; Cheng et al., 2009). When the polar jet stream shifts north, creating dry conditions in the southwest, the ITCZ shifts north, creating wet conditions for regions in southeastern China affected by the AM. A weak AM interval (WAMI) corresponds to El Niño conditions in the southwest, and vice versa.

INSIGHTS FROM GEOCHRONOLOGY: PALEOHYDROLOGY AND CLIMATE-DRIVEN CONTROLS ON TRAVERTINE ACCUMULATIONS AS EVIDENCE FOR EPISODIC VARIATIONS IN SPRING DISCHARGE

We interpret the episodic travertine accumulations as variations in spring discharge. This variation reflects the complex hydrology of the Jemez Mountains. Causes of variation within spring discharge at Soda Dam include; 1) Valles Caldera lake activity and its effects of the local hydrologic head; 2) regional variations in precipitation. Estimated accumulation rates for deposits that yielded stratigraphic accumulation rates are as follows: 5,700 m^3/ka for deposit A_i, 50 m^3/ka for deposit B and 30 m^3/ka for deposit C. Rates of accumulation for deposit A are more difficult to interpret as much of the deposit is outside of U-series range.

Deposit A, containing an estimated 77% of the total travertine volume, was likely able to produce such a spectacular accumulation due to large volumes of water storage within the early Valles Caldera paleolakes. Early platform development may have begun shortly after the Valles Caldera eruption, coinciding with the hydrothermal pulse recorded at 1.0 Ma by previous research in a variety of rock records (Heiken et al., 1990; Goff et al., 1994). Incision rates from San Diego Canyon are approximately 120 m/Ma if the high elevation travertine deposition occurred at 1.1 Ma, in agreement with long term averages reported by Roger, 1996. The incision rate of the Jemez River through the upper and lower Bandelier Tuff units must have been more than twice as fast for travertine deposition to occur at 132 m above the modern river at 1.1 Ma (Goff et al., 1987). If bedrock incision rates are semi-steady with our newly reported rates of 150

and 160 m/Ma, the high platform travertine would be approximately 850 ka. This early expression of the hydrothermal system was likely a small, micritic platform developing along the banks of a paleo-Jemez river, similar to small platforms developing along the modern river, through CO_2 and thermal water ascending via the Soda Dam fault.

Local hydrologic head was high with the presence of a lake within the Valles Caldera; the rhyolite dam produced by the South Mountain Dome eruption slowed the Jemez River flow to a trickle, allowing rapid mound, pool and terrace accumulation to occur and cement river gravels. Substantial artesian head during MIS 8 could have allowed drape development from the high elevation platform of deposit A (Figure 4, 6). The period in which the Valles Caldera lake, represented by core VC-3, possibly extended through MIS 8 as a high elevation sill within the platform yielded an age of 339 ka (AJT11_SDA_52). This date also corresponds to a WAMI record (discussed above) so it is unclear whether the high head necessary to deposit the sampled sill was caused by the increased hydrologic head due to the Valles Caldera lake or wetter climatic conditions. Regardless, detailed chronology of the high elevation drape deposit could improve the applied sediment record chronology with precise U-series dates. The present caldera is marshland, with head levels approximately 1000 m above the springs at Soda Dam. Paleolake sediments are recorded a maximum of 1000 m above present day caldera floor; a 1000 m deep lake in the caldera would effectively double the local hydrologic head.

The youngest sample from deposit A is a spar sample, high in the deposit along the Soda Dam fault; this sample yielded an age of 96 ±7 ka, suggesting very high artesian head during MIS 5 while accumulation of the mound deposits B and C was occurring (Table 2, Figure 4, 6). Four spar samples in the high elevation of deposit A yielded ages of 111, 206, 211 and 339 ka that correspond to MIS 5, 7 and 10; there is not systematic evidence to conclude that periods of high hydrologic head occurred only during the wetter glacial periods (AJT11_SDA_52, LC10_NMSDA_22a, LC10_NMSDA_22b and LC11_NMSDA_34; Table 2, Figure 6).

Deposit A_i is inset into the drape of deposit A, whose basal portion of accumulation was eroded by increased flow in the Jemez River, or destroyed if the failure of the rhyolite dam was catastrophic. Deposit A_i begins accumulation 32 m above the modern Jemez River and was active for at least 52 ka during MIS 6; this time period also correlates to a WAMI as recorded in the Sanbao Cave, a peak in insolation at 35°N and lighter isotopic values (Pacific-based winter precipitation) recorded at Devil's Hole (Table 2; Figure 4, 6; Winograd et al., 2006; Cheng et al., 2009). The basal portion of Deposit A_i preserves paleo-Jemez River gravels from the 200 ka valley bottom (K06-SDam-2, Table 2, Figure 4). A cross cutting sill at 110.9 ±1.5 ka is another indication of wet periods during interglacial MIS 5 (K06-SDam-1, Table 2, Figure 6).

Deposit B dates indicate accumulation for at least a 130,000 yr interval that begins during MIS 7, through penultimate glacial (MIS 6) to the preceding Eemian interglacial (MIS 5) (Figure 6). The fissured vein system was sampled near the base of the deposit, against country rock. The oldest date, 209.6 ±1.7 ka, suggests that calcite growth began within the Jemez fault a minimum of 70 ka before above ground mound accumulation began. This calcite growth began within the Soda Dam fault when the paleo-Jemez River flowed at an elevation near the top of deposit B mound accumulation (Figure 4). The vein system displays discontinuous growth indicated by the sequence of ages (Table 2; Figure 11). The infilling could be a result of fault reactivation or splitting and infilling from slumping under weight as the mound accumulation developed on alluvium (Figure 3). Deposit B began large travertine mound accumulation at 137.5 ±1.0 ka, which correlates to a rise in Pacific SST recorded in the Devil's Hole calcite, and a WAMI recorded in Hulu and Sanbao Caves, China (LC10_NMSDB_15; Table 2, Figure 6; Winograd et al., 2006; Cheng et al, 2009:2012). The SST warming recorded in Devil's Hole also correlates to a peak in insolation at 35° latitude, which occurs during the glacial MIS 6. The combination of a warm Pacific SST due to peak solar insolation and a cold North Atlantic during a glacial period could explain the increase in winter precipitation that would be necessary for large volume travertine accumulation.

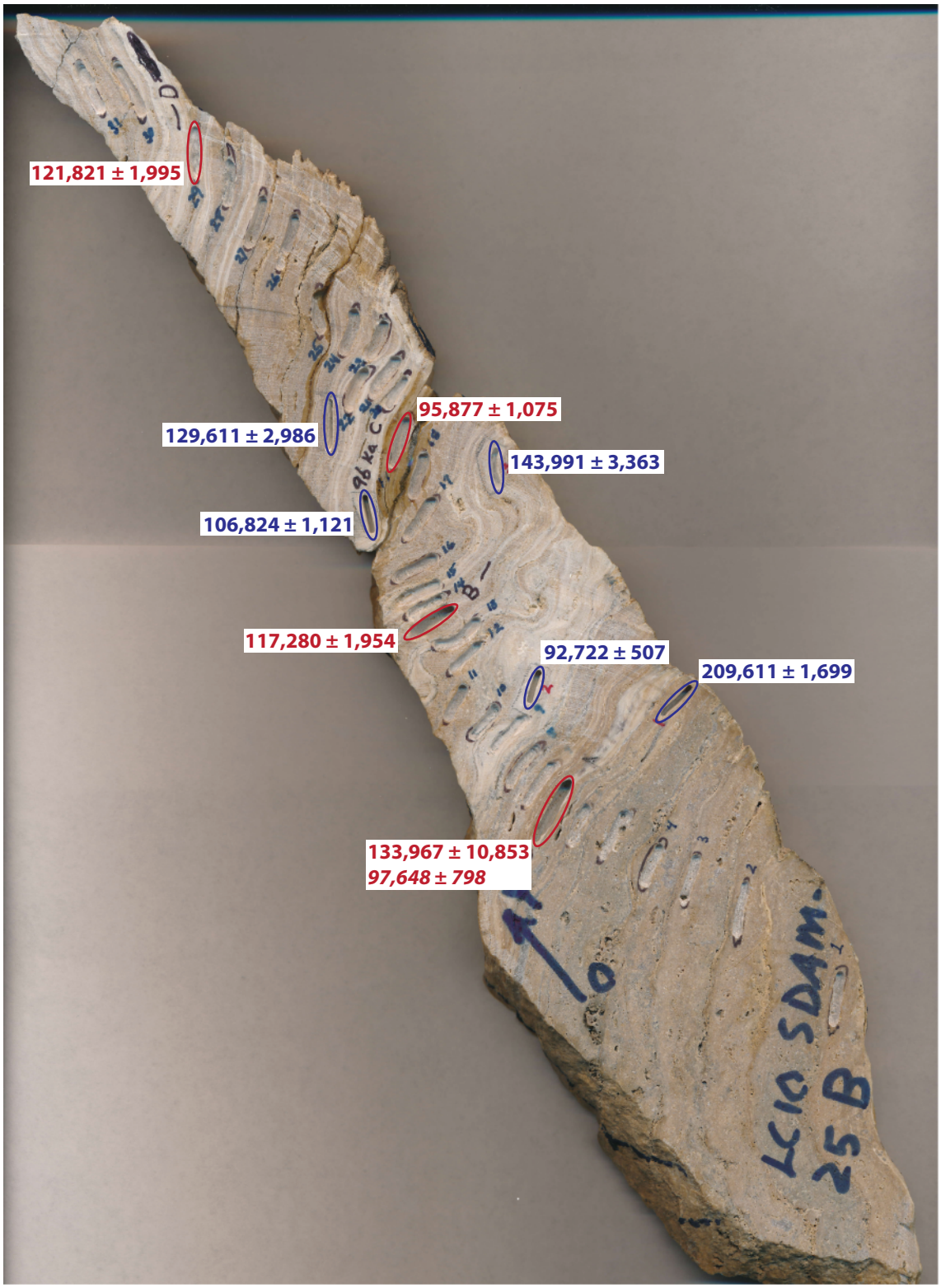

Figure 11: Sample from deposit B fissure vein (LC10_SDamB_25) displaying U-series dated locations.

Two distinct WANI occur during the beginning of the Eemian interglacial, which is clearly recorded as a wet interval within the Soda Dam deposits. Deposit C began accumulation shortly after the recorded WAMI and simultaneously with the mound accumulation of deposit B; cessation of deposit C accumulation occurs correlates with an interstadial event recorded from a speleothem in Nevada (Denniston et al., 2007). The large volume accumulation event that occurs through the beginning of the Eemian interglacial also correlates to lighter isotopic values recorded in the Devil's Hole record.

Deposit A_i exhibits the largest rate of accumulation, through the glacial MIS 6. However, deposits A_i, B and C do not begin stratigraphic mound accumulation corresponding to marine glacial intervals based on SPECMAP chronology, but rather are likely driven by a more complicated regional climate system that controls precipitation in the southwestern United States discussed above. Deposits A, A_i and B yielded dates within MIS 7 from cross cutting calcite veins and the main fissure ridge, respectively (LC10_SDamB_25B_1a, LC10-NMSDA-22b, LC11_NMSDA_34, K06-SDam-2). This period of high hydrologic head broadly correlates to enriched isotopic values recorded in the Hulu and Sanbao records; it is likely that regional records, once they are established, will reveal a wet time period in the southwest from 200 – 210 ka.

Deposit D began accumulation during the early stages of the current interglacial, much later than the pluvial, glacial highstands recorded in Lake Estancia at 19.7 and 13.7 ka, in central New Mexico, and is still actively depositing travertine today (Allen et al., 2000). The closely spaced dates from the central fissure vein suggest rapid accumulation around 5 ka (LC10_Sdam_28a,b,c; Table 2).

The Soda Dam system is likely limited by water flux, as opposed to a system that is limited by the flux of external CO_2. Dates yielded by the deposits at Soda Dam correspond to proxies recording wetter paleoclimatic and hydrologic conditions, rather than with the timing of volcanic activity in the Valles Caldera. For example, a system limited by the flux of external CO_2 may become diluted during times of high spring discharge and is more probable to produce travertine during climatically dryer conditions (Crossey et al., 2011). As more regional paleoclimate proxies are established,

it will likely become clear that large volume accumulation of travertine in the water limited southwest is driven by the millennial scale forces, rather than global glacial/interglacial cycles.

SUMMARY OF MAIN FINDINGS

Periods of travertine accumulation were episodic at Soda Dam, occurring at approximately 500, 200,140-90, and 10 ka to present (Figure 4, 6) with records of high artesian head at approximately 95, 110, 210, 340, 455 and 486 ka. The Valles Caldera paleolakes, were the likely the cause of the high hydrologic head and the accumulation of the large volume deposit A. Periods of accumulation and high head correlate broadly to regional paleoclimate records, rather than the global glacial/interglacial periods; data from the travertine deposits at Soda Dam reveal wet conditions during the beginning of the Eemian interglacial for this alpine study cite in Northern New Mexico. Bedrock incision rates through the upper reaches of San Diego Canyon were semi-steady for at least the past 200 ka; robust rates were calculated at 150 m/Ma over last 200 ka and 160 m/Ma over the last 100 ka, slightly faster than previously reported long term rates.

Stable isotope values revealed a large range for $\delta^{18}0$, reflecting variations in local spring chemistry, source water through time, and fractionation effects. Positive values of $\delta^{13}C$ suggest degassing of the light CO_2 and a higher quantity of endogenically derived CO_2 relative to other endmember sources in the hydrothermal system. A sensitivity analysis suggested that steady state conditions for source water isotopic composition for the past 500 ka is unlikely due to inconsistent temperature variations with systematic changes in $10^3 ln\alpha$.

The deposits at Soda Dam have a dynamic history, full of massive volcanic eruptions, the filling and draining of caldera lakes, global and regional forcing's affecting the climate and recharge, and active faulting that has channeled hydrothermal waters carrying mantle and magmatic signals from deep within the Earth; it is no wonder over 1 million visitors stop at this site each year. The Soda Dam is an iconic landmark in New Mexico, worthy of attention as a world heritage site.

APPENDICES

APPENDIX A – METHODS

Water Sampling and Analysis Methods

Spring temperature, pH, conductivity and total dissolved solids were measured in situ using an Oakton 1066 Series pH/ion/°C portable meter. Spring coordinates (WGS84, UTM) were collected with a handheld GPS unit. At each locality two water samples were collected in Nalgene bottles. One was collected without head space for the preservation of bicarbonate in alkalinity measurements; anions were also analyzed from this sample. A second sample was collected with a 0.45 micron filter and acidified with HNO_3 for preservation of dissolved metals; cations were also calculated from this sample. Each time a sample was collected, the bottle and syringe were rinsed three times with sample water. Water samples were preserved in cold storage and analyzed for major and minor element composition within 2 weeks in the Diagensis and Analytical Chemistry Laboratories at the University of New Mexico using standard Methods (American Public Health Association, 1995). Cations, metals and minor elements were analyzed using a Perkin Elmer Inductively Coupled Plasma Optical Emission Spectrophotometer (ICPOES). Anions were analyzed using the Dionex DX-500 Ion chromatograph. To determine alkalinity as a measure of the concentrations of CO_3, HCO_3, and $CaCO_3$, endpoint alkalinity titrations were performed on each sample with a pH meter. Ten milliliters of each sample were titrated with 0.2 N sulfuric acid (H_2SO_4). These titrant volumes, sample volumes, and sulfuric acid normality were used to calculate concentrations of CO_3, HCO_3, and $CaCO_3$. The pH meter was calibrated with pH 7 and pH 10 standard buffers. PHREEQCI (Version 2, Parkhurst and Appelo, 1999) was used for simulating chemical reactions, speciation, saturation indices for minerals and transport processes in the sampled water.

Uranium-series Geochronology

Subsamples as drilled powders were dissolved in 15N nitric acid, spiked with a mixed solution with known concentrations of ^{229}Th, ^{233}U and ^{236}U. After fluxing, the spiked solutions were dried down; then redissolved in 15N nitric acid with one to two

drops of perchloric ($HClO_4$) acid. These solutions are dried down and redissolved in 7N nitric acid for column work. Sample solutions are introduced into 200 µL Teflon columns having 0.5 ml of anion resin where U and Th are cleaned and separated. Thorium is collected with a flush of 6N HCl, uranium with H_2O. These separates are dried down and redissolved in 2-3% nitric acid, and then are ready for analyses on a Thermo Neptune Mulitcollector Inductively Coupled Plasma Mass Spectrometer (MC-ICPMS). The U and Th isotope ratios were measured on the MC-ICPMS as a static run with ^{230}Th and ^{234}U going into a secondary electron multiplier (SEM), and all other isotopes measured in Faraday cups. SEM-Faraday gain was established using CRM-145 U standard for U and an in-house Th standard for Th analyses. The CRM-145 U isotope standard was measured with the samples yielding the conventionally accepted $\delta^{234}U$ value of -36.5 ±0.5‰ (Asmerom et al. 2006). Procedural blanks are between 5-30 picograms for both ^{232}Th and ^{238}U. All laboratory work is completed in the Radiogenic Isotope Laboratory at the University of New Mexico.

Stable Isotope Geochemistry

For stable oxygen and carbon isotopic analysis, subsamples as drilled powders were flushed with He gas, then reacted for 24 hours with H_3PO_4 at 50°C (Spotl and Vennemann, 2003). Evolved CO_2 was measured by continuous flow Isotope Ratio Mass Spectrometery using a Gasbench device coupled to a Finnigan Mat Delta Plus Isotope Ratio Mass Spectrometer in the Stable Isotope Laboratory at the University of New Mexico. Carbon and oxygen isotope ratios will be expressed in delta notation relative to VPDB and VSMOW standards, for carbonate and water, respectively.

Mapping and GIS Analysis

Existing geologic maps (Goff et al., 1980; Kelley, 2003) were digitized and compiled into a working field map. Digital datalayers were New Mexico Geologic Survey, RGIS and USGS topographic maps were compiled using ArcGIS 10.0 (ESRI, 2011).

APPENDIX B – LIST OF FIGURES, TABLES AND CAPTIONS

Figure 1: Tectonic DEM map of the Jemez transfer zone formed at the intersection of the Rio Grande rift, the Jemez lineament and Soda Dam. Neotectonic features of this area include: Quaternary extensional and transtensional faults, Plio-Pleistocene volcanic fields (line pattern), springs with mantle ^{3}He (white dots), and Quaternary travertine deposits (stars).

Figure 2: Schematic hydrothermal cross section (modified from Goff, 2009) depicting endogenic waters entering the hydrothermal system via faults (red arrows) and mixing (orange & blue arrows) with the meteoric waters (blue arrows). The hydrothermal waters are heated at depth and convected up where they flow down the Paleozoic aquifer units, mixing with meteoric waters along the way, through the JFZ in San Diego Canyon. A portion of these waters discharge at Soda Dam hot springs and deposit travertine.

Figure 3: Localized geologic map of the Soda Dam study area (modified from Goff et al., 1980; Kelly et al., 2003; and Moats, 2004) depicting locations of the five travertine deposits, as well as major faults that act as subsurface conduits, channeling the hydrothermal plume through San Diego canyon.

Figure 4: Schematic profile of San Diego Canyon depicting elevations and ages of travertine samples (yellow stars, Table 2) as well as paleocanyon positions resolved through U-series dating of travertine cemented river gravels.

Figure 5: Stable isotope graph, δD vs. δ^{18}O (‰, SMOW) of Baca Wells, Jemez River and fluids at Soda Dam (Table 1). Soda Dam fluids plot as a mixture of hydrothermal and meteoric waters. Local meteoric water line from Vautaz et al., 1986.

Figure 6: Timeline displaying dated travertine deposits of Soda Dam in relation to; MIS

(Wright, 1999); SPECMAP marine core record (Lisiecki and Raymo, 2005); Devil's Hole calcite record (Winograd et al., 1997); Northern Hemisphere Insolation at 35°N (Huybers, 2006); Fort Stanton stalagmite record (Asmerom et al., 2010); Hulu and Shanbao Cave records (Cheng et al., 2012); WAMI (pink boxes); Jemez Mountain volcanic history and VC-3 lake core record (Fawcett et al., 2011). Probability plot displays sample frequency in yellow bars and 2σ error curve in gray; dated samples (black circle) display error bars in red, except when error is smaller than sample point.

Figure 7: Stable Isotopes of carbon and oxygen from travertine samples (Table 3).

Figure 8: Stable Isotopes of carbon and oxygen from travertine samples through time (Table 3).

Figure 9: Calculated range of δ18Owater values using the Demény et al., 2010 calcite-water oxygen isotope fractionation equation [1000lnα = 17.599 (1000/T) -29.64], based on measured δ18Ocalcite values for a range of modern temperatures (10-60°C) which encompass the modern temperature range of travertine depositing springs, shown in black diamonds with measured depositing temperature. Range of modern water values shown in blue.

Figure 10: Modified from Cox (1995), profile of the Jemez River from San Antonio hot springs to the confluence with the Rio Grande. New dated strath (yellow circles, deposit Ai) at 16.5 and 32 m above the modern river. Graph depicts long term incision rates (195m/Ma; Rogers, 1996) and new incision rates (160 & 150m/Ma). Red box is potential age range of river gravels at 132 m above the modern river.

Figure 11: Sample from deposit B fissure vein (LC10_SDamB_25) displaying U-series dated locations.Figure 10: Stable isotopes of $\delta^{18}O$ & $\delta^{13}C$ through time.

Table 1: Description, temperature, pH and measured stable isotope values of water from various springs and locations along the Jemez River (JR) in San Diego Canyon, and the Baca Wells (Figure 8).

Table 2: Location and U-series data for travertine samples.

Table 3: Measured stable isotope values of $\delta^{18}O$ and $\delta^{13}C$ of travertine samples.

Table 4: Paleotemperature calculations using temperature dependent fractionation factors by Demeny et al., 2010; Kele et al., 2011; Kim and O'Neil, 1997 and Romanek et al., 1992 (eq. 6,7; APPENDIX D).

Table 5: VC-3 Core Chronology Data (Fawcett et al., 2011).

Table 6: Model ages for out of U-series range travertine samples.

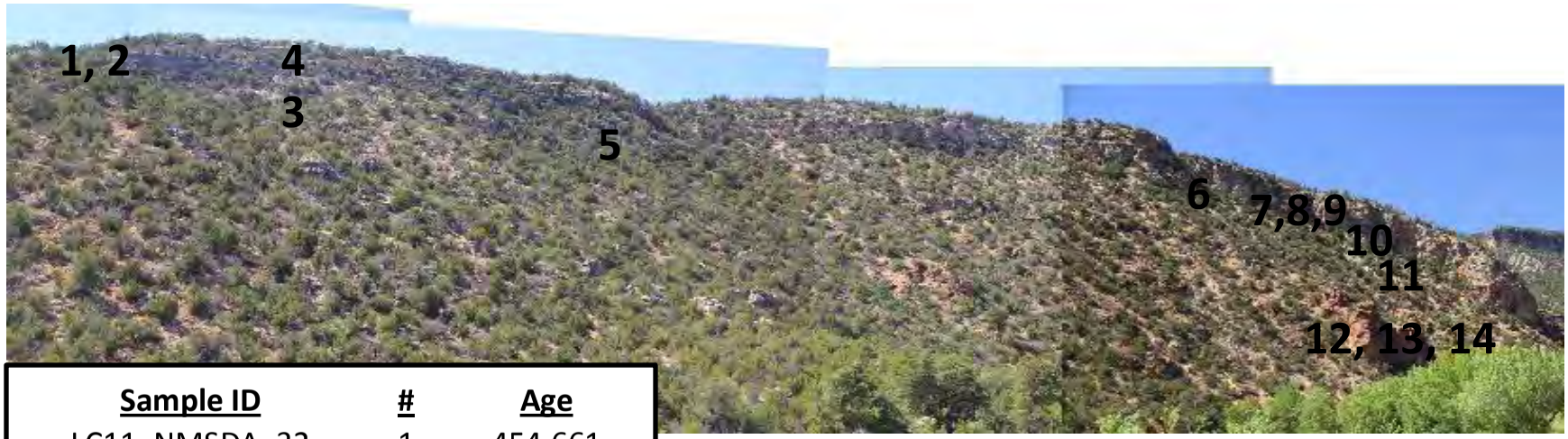

Sample ID	#	Age
LC11_NMSDA_32	1	454,661
LC11_NMSDA_34	2	206,563
AJT11_SDA_52	3	339,407
LC11_NMSDA_30	4	95,661
AJT11_SDA_51	5	485,690
LC10-NMSDA-24	6	481,860
LC10-NMSDA-22b	7	210,645
LC10_NMSDA_22a	8	110,605
LC10-NMSDA-23a	9	286,864
LC10-NMSDA-21	10	131,546
LC10-NMSDA-20	11	166,457
K06-SDam-4	12	183,147
K06-SDam-1	13	110,981
K06-SDam-2	14	200,595

AJT11_SDA_51

AJT11_SDAM_1

AJT11_SDA_52

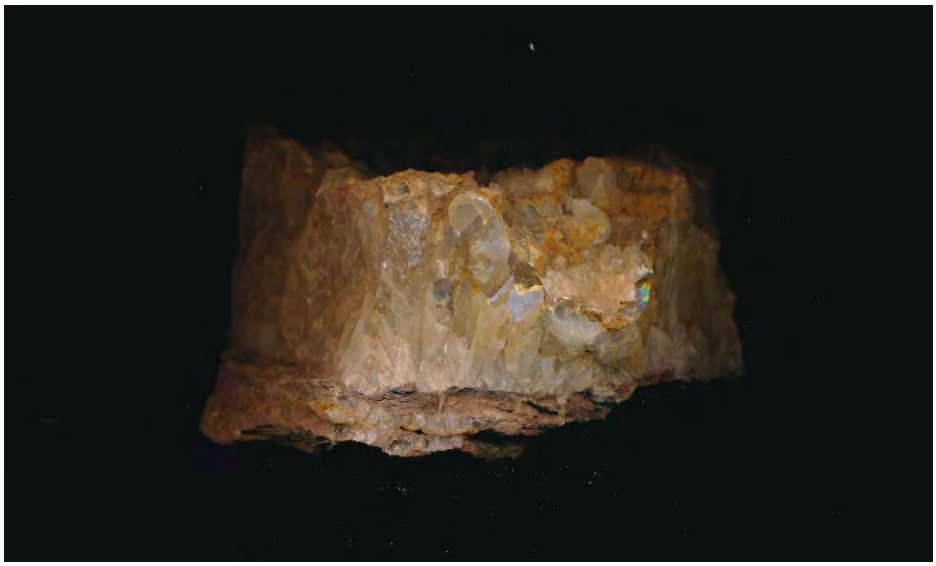

K06_SDAM_1

K06_SDAM_2

K06_SDAM_4

LC10_NMSD_11

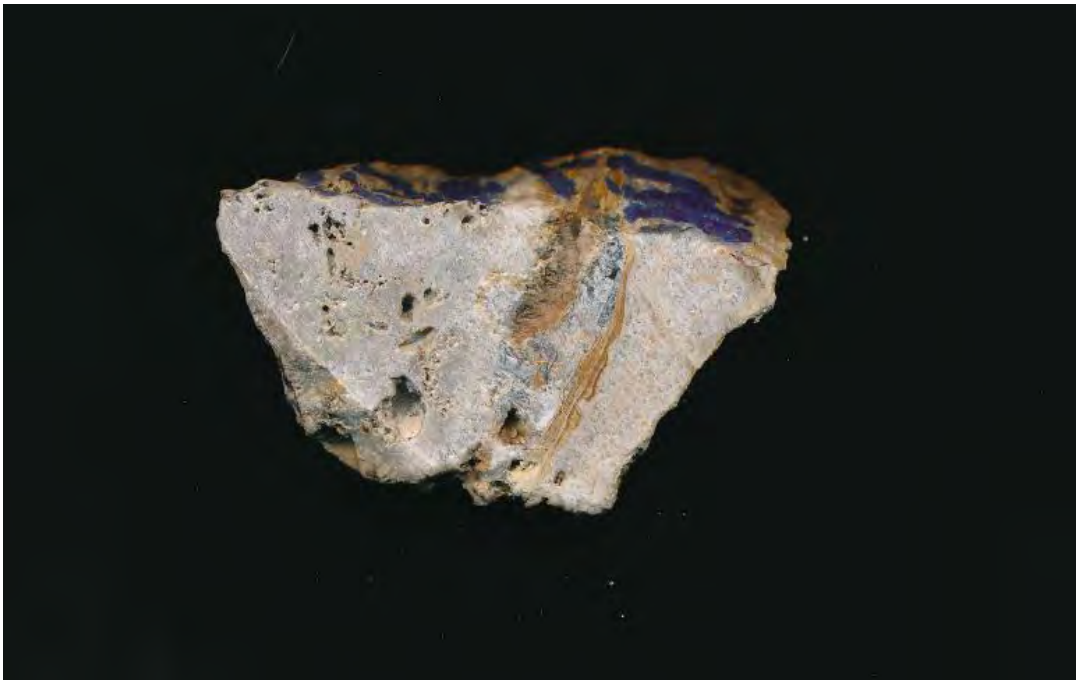

LC10_NMSD_15

LC10_NMSDA_20

LC10_NMSDA_21

LC10_NMSDA_22

LC10_NMSDA_24

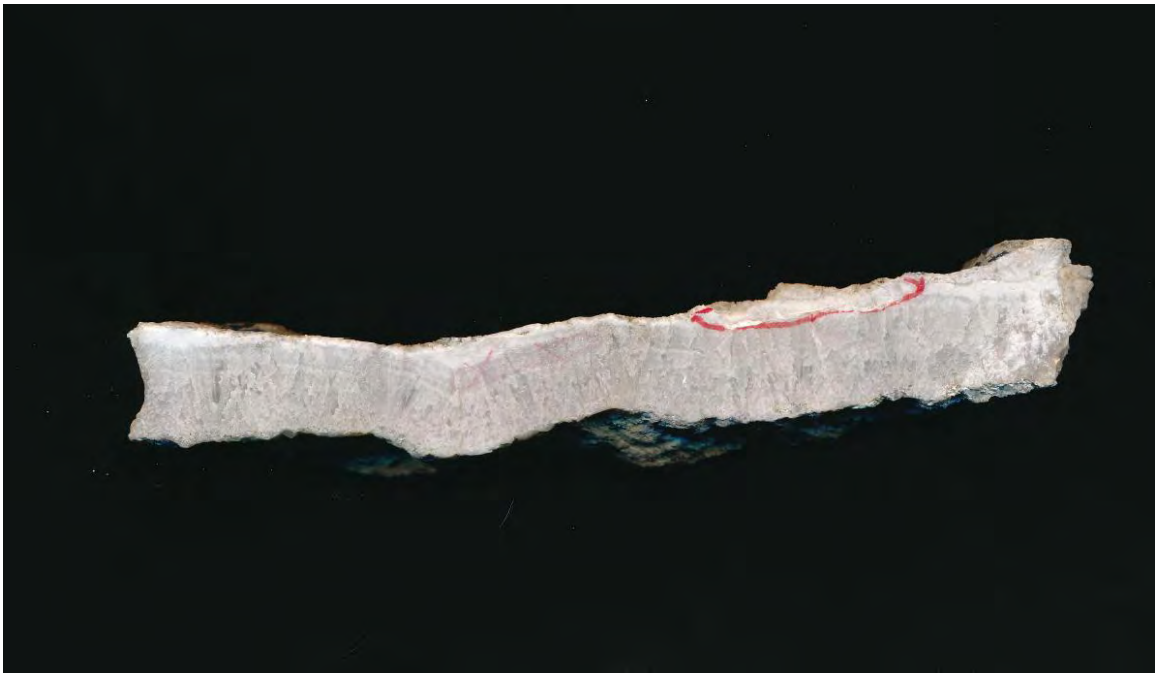

LC10_NMSDA_28

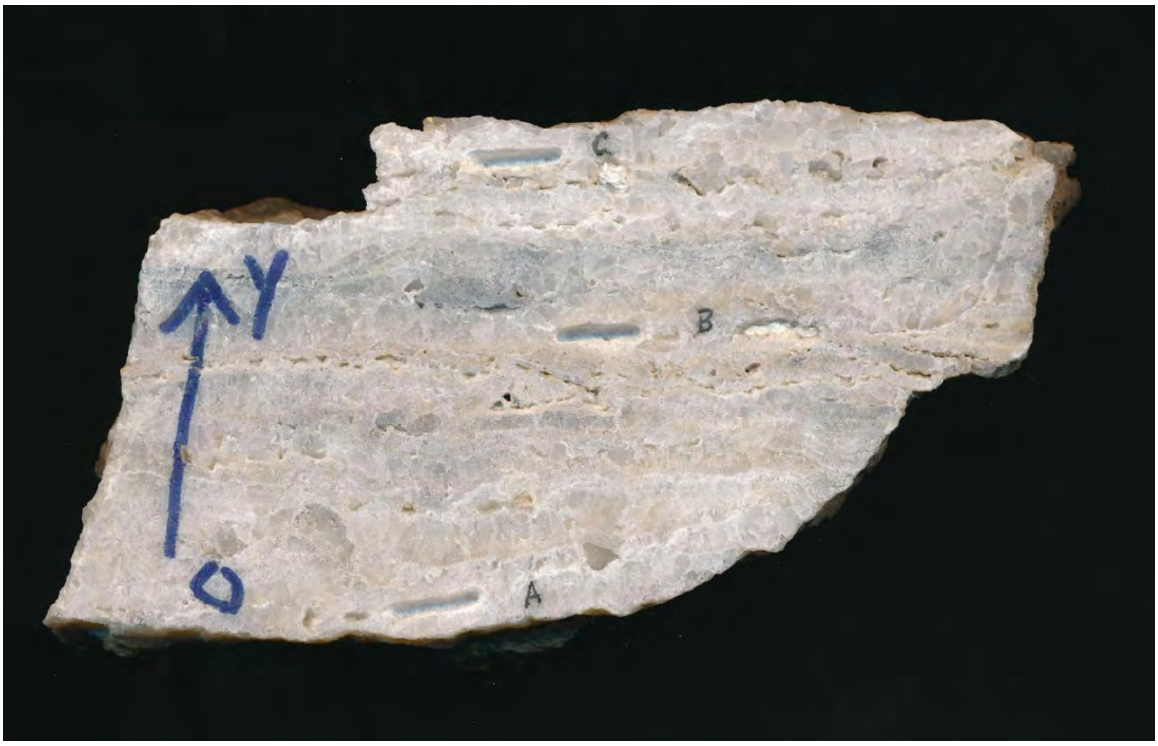

LC10_NMSDA_19

LC10_NMSDA_13

LC11_NMSDA_31

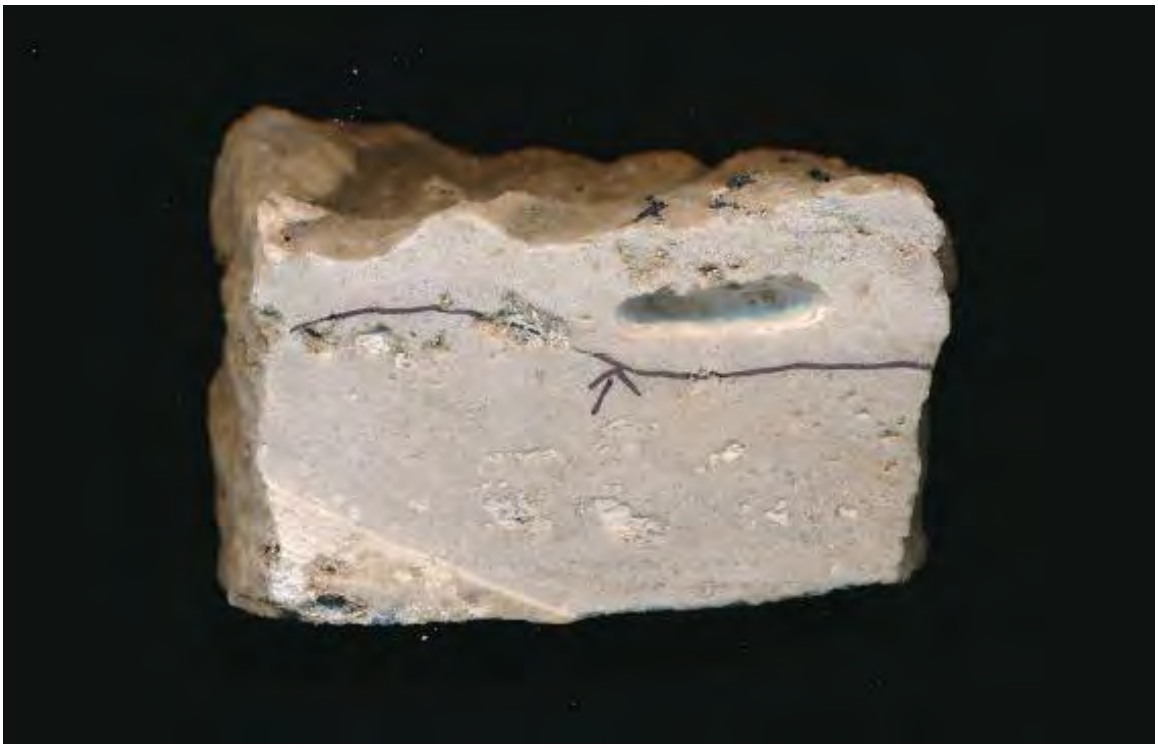

LC11_NMSDA_32

LC11_NMSDA_34

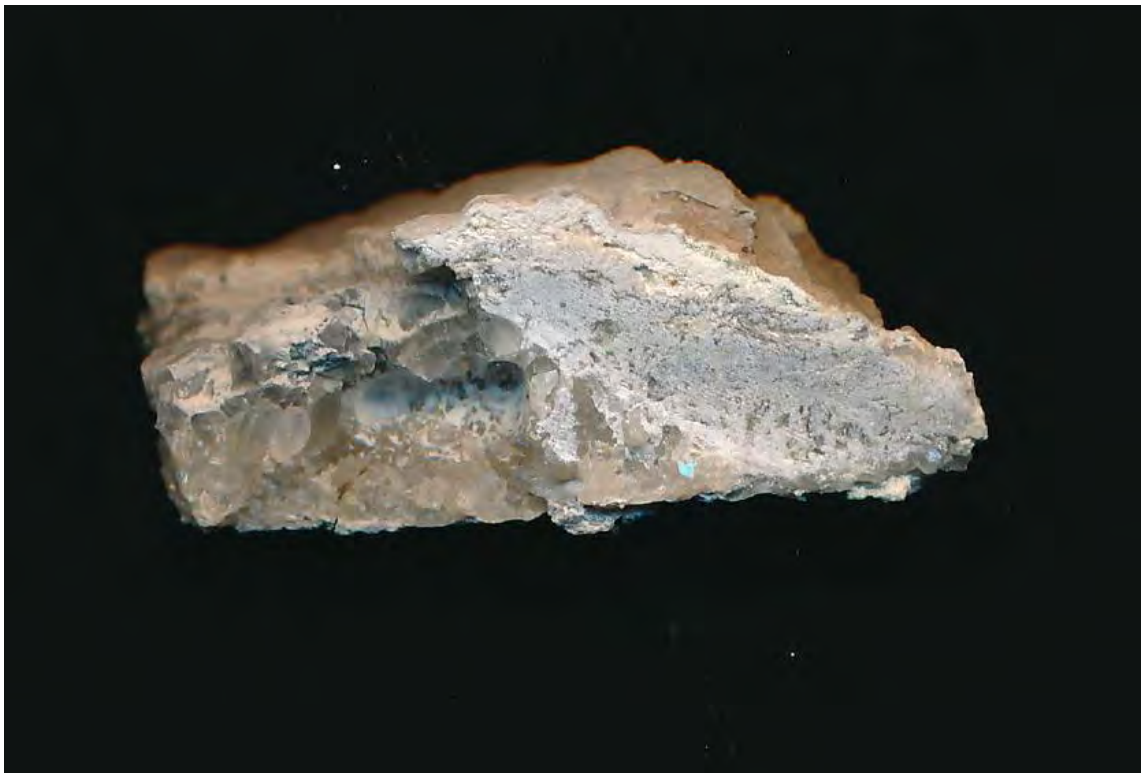

LC11_NMSDA_36

LC11_NMSDA_30

LC10_SDA_23a

AJT11_SDAM_2

KLC12_SD100

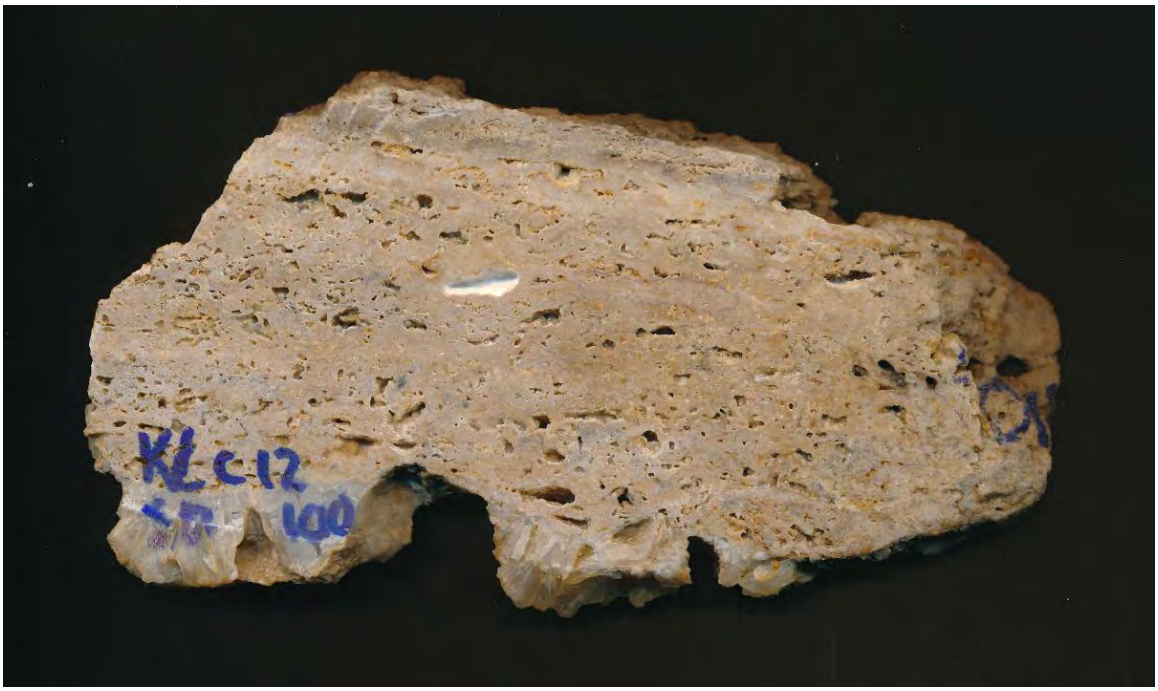

APPENDIX D – SUPPLEMENTARY INFORMATION

Table 5: VC-3 Core Chronology Data (Fawcett et al., 2011)

Age (ka)	Depth in core (m)	Age determination method
363	5.50	Upper core average sedimentation rates applied to sediment lamination between 17.25 m (400 ka) and 5.5 m producing an age estimate for top of core (lake termination).
400	17.25	Geomagnetic field event 11α.
426	27.50	Abrupt significant increase in TOC, Si/Ti ratios, MAT estimates, $\delta^{13}C_{TOC}$, C:N and warm taxa pollen types correlated to termination V (Lieseiki et al., 2005)
480	43.10	Significant decreases in Si:Ti, warm taxa pollen, and MAT estimates correlated to the end of MIS 13 (global age, Lieseiki et al., 2005). Linear interpolation of sediment rates places 43.1 m at 505 ka; mudcracks indicate sediment hiatuses.
520	47.45	Depth of onset of mudcracked interval in MIS 13; average sedimentation rate from upper core applied.
533	51.50	Abrupt significant increase in TOC, Si/Ti ratios, MAT estimates, $\delta^{13}C_{TOC}$, C:N and warm taxa pollen types correlated to termination VI (Lieseiki et al., 2005).
536	52.30	Geomagnetic field event 14α.
552	75.60	Ar-Ar age date; South Mountain Dome eruption.

Stable Isotopes of Carbon and Oxygen:

Variations of ^{18}O and ^{16}O are measured using mass spectrometry relative to the Pee Dee Belemnite (PDB) standard for carbonates and Standard Mean Ocean Water (SMOW) standard for water, then expressed in delta (δ) notation (eq. 1) (Sharp, 2007).

$$\delta^{18}O = [(^{18}O/^{16}O_{sample} - {}^{18}O/^{16}O_{standard})/(^{18}O/^{16}O_{standard})] \times 1000$$

Isotopic ratios are expressed in per mil (‰) notation where PDB and SMOW are defined as 0.0‰ (Sharp, 2007). The PDB and SMOW standards can be related using (eq. 2) and (eq. 3) (Sharp, 2007).

$$\delta^{18}O_{SMOW} = 1.03091\ (\delta^{18}O_{PDB}) + 30.91$$
$$\delta^{18}O_{PDB} = 0.97002\ (\delta^{18}O_{SMOW}) - 29.98$$

Fractionation is defined by (eq. 4) where α is the equilibrium fractionation and R is the isotopic ratio between phase changes (A-B, calcite-water); fractionation is expressed in 1000lnα notation (Sharp, 2007).

(4) $\alpha_{A\text{-}B} = R_A/R_B$

Paleothermometry:

Temperatures were calculated based on equilibrium oxygen isotope temperature dependent fractionation factors as determined by O'Neil, 1969 (eq. 5) and Kim and O'Neil, 1997 (eq. 6):

(5) $$10^3 \ln\alpha_{calcite-water} = \frac{2.78x10^6}{T^2} - 2.89$$

(6) $$10^3 \ln\alpha_{calcite-water} = \frac{18.03x10^3}{T} - 32.42$$

where T (temperature) is in kelvins and α is calculated using eq.4 (above). Equilibrium fractionation was determined with measured values of $\delta^{18}O_{calcite}$ and a range of $\delta^{18}O_{water}$ (-13 - -8‰) based on measured $\delta^{18}O_{water}$ values from various studies (Fig. 5, paper).

Temperatures were calculated based on equilibrium carbon isotope temperature dependent fractionation factors as determined by Romanek et al., 1992 (eq. 7):

(7) $$10^3 \ln\alpha_{calcite-CO2(gas)} = 11.98 - 0.12 \times T$$

where T (temperature) is in Celsius and α is calculated using eq.4 (above), between CO_2 (gas) and calcite. Equilibrium fractionation was determined with measured values of $\delta^{13}C_{calcite}$ and a measured value of $\delta^{13}C_{CO2}$ of -4.9‰ from Goff et al., 2002.

Temperatures were calculated based on equilibrium carbon isotope temperature dependent fractionation factors as determined by Demény et al., 2010 (eq. 8):

(8) $$10^3 \ln\alpha_{calcite-water} = 17.599 \left(\frac{1000}{T}\right) - 29.64$$

where T (temperature) is in Celsius and α is calculated using eq.4 (above), between calcite and water. Equilibrium fractionation was determined with measured values of $\delta^{13}C_{calcite}$ and a range of $\delta^{18}O_{water}$ (-13 - -8‰) based on measured $\delta^{18}O_{water}$ values from various studies (Fig. 5, paper).

Temperatures were calculated based on equilibrium carbon isotope temperature dependent fractionation factors when species of carbon are bicarbonate after Kele et al., 2011 (eq. 9):

(9) $$10^3 \ln\alpha_{bicarbonate-water} = \left(\frac{12{,}920{,}000}{T^2}\right) - 2.66$$

where T (temperature) is in Celsius and α is calculated using eq.4 (above), between bicarbonate and water. Equilibrium fractionation was determined with measured values of $\delta^{13}C_{calcite}$ and a range of $\delta^{18}O_{water}$ (-13 - -8‰) based on measured $\delta^{18}O_{water}$ values from various studies (Fig. 5, paper).

Model Ages

Model ages for out of U-series range travertines were determined based upon the following age equations:

(8) $$n = n_o\, e^{-\lambda t}$$

Where *n* is ^{234}U measured, n_o is ^{234}U initial and λ is the decay constant for ^{234}U. Initial 234U value is unknown and estimated as a range from other measured samples (Table 2, 6).

WORKS CITED

ALLEN, B. D. & ANDERSON, R. Y. 2000. A continuous, high-resolution record of late Pleistocene climate variability from the Estancia basin, New Mexico. *Geological Society of America Bulletin,* 112**,** 1444-1458.

ASMEROM, Y., POLYAK, V. J. & BURNS, S. J. 2010. Variable winter moisture in the southwestern United States linked to rapid glacial climate shifts. *Nature Geoscience,* 3**,** 114-117.

BALLENTINE, C.J. & BURNARD, P.G. 2002. Production, release and transport of noble gases in the continental crust, *in* Porcelli, D., Ballentine, C.J., and Weiler, R., eds., Reviews in mineralogy and geochemistry— Noble gases in geochemistry and cosmochemistry, Volume 47: Washington, D.C., Mineralogical Society of America, p. 481–538.

BALLENTINE, C.J., BURNARD, P.G., MARTY, B. 2002. Tracing fl uid origin, transport and interaction in the crust, *in* Porcelli, D., Ballentine, C.J., and Wieler, R., eds., Reviews in mineralogy and geochemistry—Noble gases in geochemistry and cosmochemistry, Volume 47: Washington, D.C., Mineralogical Society of America, p. 539–614.

BULL, D., KEMP, A.E.S, & WEEDON, G.P. 2000. A 160-k.y.-old record of El Nino-Southern Oscillation in marine production and coastal runoff from Santa Barbara Basin, California, USA. *Geology*, 28, 11, 1007-1010.

CHAFETZ, H.S., & FOLK, R.L. 1984. Travertines: Depositional morphology and the bacterially constructed constituents. *Journal of Sedimentary Petrology*, 54, 1, 0289-0316.

CHENG, H., EDWARDS, R.L., WANG, Y., KONG, X., MING, Y., KELLY, M.J., WANG, X., GALLUP, C.D., & LIU, W. 2006. A penultimate glacial monsoon record from Hulu Cave and two-phase glacial terminations. *Geology*, 34, 3, 217-220.

CHENG, H., EDWARDS, R.L., BROECKER, W.S., DENTON, G.H., KONG, X., WANG, Y., ZHANG, R., & WANG, X. 2009. Ice age terminations. *Science*, 326, 248-251.

CHIODINI, G., FRONDINI, F., CARDELLINI, C., PARELLO, F., & PERUZZI, L. 2000. Rate of diffuse carbon dioxide Earth degassing estimated from carbon balance of regional aquifers: The case of central Apennine, Italy. *Journal of Geophysical Research*, 105, B4, 8423-8434.

CLARK, I. & FRITZ, P. 1997. *Environmental Isotopes in Hydrogeology,* New York, CRC Press LLC.

CLIMAP Project Members. 1984. The last interglacial ocean. *Quaternary Research*, 21, 123-225

COX, C., KELLEY, S. A., KARLSTROM, K. E., CROSSEY, L., DILLON, M. & NEWELL, D. 2005. Quanternay Incision History of the Upper Reaches of the Jemez River. *New Mexico Geology,* 27**,** 43.

CROSSEY, L. J., FISCHER, T. P., PATCHETT, P. J., KARLSTROM, K. E., HILTON, D. R., NEWELL, D. L., HUNTOON, P., REYNOLDS, A. C. & DE LEEUW, G. A. M. 2006. Dissected hydrologic system at the Grand Canyon: Interaction between deeply derived fluids and plateau aquifer waters in modern springs and travertine. *Geology,* 34**,** 25-28.

CROSSEY, L. J., KARLSTROM, K. E., SPRINGER, A. E., NEWELL, D., HILTON, D. R. & FISCHER, T. 2009. Degassing of mantle-derived CO_2 and He from springs in the southern Colorado Plateau region - Neotectonic connections and implications for groundwater systems. *GSA Bulletin,* 121**,** 1034-1053.

CROSSEY, L.J., KARLSTROM, K.E., NEWELL, D.L., KOOSER, A., & TAFOYA, A. 2011. The La Madera travertines, Rio Ojo Caliente, Northern New Mexico: Investigating system of CO2-rich springs and travertines as neotectonic and paleoclimate indicators. *New Mexico Geological Society Guidebook, 62nd Field Conference, Geology of the Tusas Mountains – Ojo Caliente*, 121-136.

DENNISTON, R.F, ASMEROM, Y., POLYAK, V., DORALE, J.A., CARPENTER, S.J., TRODICK, C., HOYE, B., & GONZALEZ, L.A. 2007. Synchronous millennial-scale climatic changes in the Great Basin and the North Atlantic during the last interglacial. *Geology*. 35, 7, 619-622.

DEMÉNY, A., KELE, S., & SIKLÓSY, Z. 2010. Empirical equations for the temperature dependence of calcite-water oxygen isotope fractionation from 10 - 70°C. *Rapid Commun. Mass Spectrom.* 24, 3521-3526

EMBID, E.H., 2009. U-Series dating, geochemistry, and geomorphic studies of travertines and springs of the Springerville area, East-Central Arizona, and tectonic implications. *Thesis, Master of Science, Earth and Planetary Sciences*, 1-103

ESRI 2011. ArcGIS Desktop: Release 10. Redlands, CA: Environmental Systems Research Institute.

FAWCETT, P.J., HEITKOOP, J., GOFF, F., ANDERSON, R.S., DONOHOO-HURLEY, L.,

GEISSMAN, J.W., WOLDEGABRIEL, G., ALLEN, C.D., JOHNSON, C.M., SMITH, S.J., & FESSENDEN-RAHN, J. 2007. Two middle Pleistocene glacial-interglacial cycles from Valles Grande, Jemez Mountains, northern New Mexico. *New Mexico Geological Society Guidebook, 58th Field Conference, Geology of the Jemez Region II,* 409-417.

FAWCETT, P. J., WERNE, J. P., ANDERSON, R. S., HEIKOOP, J. M., BROWN, E. T., BERKE, M. A., SMITH, S. J., GOFF, F., DONOHOO-HURLEY, L., CISNEROS-DOZAL, L. M., SCHOUTEN, S., DAMSTE, J. S. S., HUANG, Y. S., TONEY, J., FESSENDEN, J., WOLDEGABRIEL, G., ATUDOREI, V., GEISSMAN, J. W. & ALLEN, C. D. 2011. Extended megadroughts in the southwestern United States during Pleistocene interglacials. *Nature,* 470**,** 518-521.

FORMENTO-TRIGILIO, M. L. & PAZZAGLIA, F. J. 1998. Tectonic Geomorphology of the Sierra Nacimiento: Traditional and New Techniques in Assessing Long-Term Landscape Evolution in the Southern Rocky Mountains. *The Journal of Geology,* 106**,** 433-454.

FOUKE, B. W., FARMER, J. D., DES MARAIS, D. J., PRATT, L., STURCHIO, N. C., BURNS, P. C. & DISCIPULO, M. K. 2000. Depositional facies and aqueous-solid geochemistry of travertine-depositing hot springs (Angel Terrace, Mammoth Hot Springs, Yellowstone National Park, USA). *Journal of sedimentary research. Section A, Sedimentary petrology and processes,* 70**,** 565-585.

GILBERT, R.O., TABERNER, C., SAEZ, A., GIRALT, S., ALONSO, R.N., EDWARDS, R.L., & PUEYO, J.J. 2009. Igneous origin of CO2 in ancient and recent hot-spring waters and travertines from the northern Argentinean Andes. *Journal of Sedimentary Research*, 79, 554-567

GOFF, F. 2002. Gas geochemistry of the Valles caldera region, New Mexico and comparisons with gases at Yellowstone, Long Valley and other geothermal systems. *Journal of Volcanology and Geothermal Research*, 116, 3-4, 299-323.

GOFF, F. 2009. *Valles Caldera: A Geologic History,* Albuquerque, University of New Mexico Press.

GOFF, F. & GARDNER, J. N. 1994. Evolution of a Mineralized Geothermal System, Valles Caldera, New Mexico. *Economic Geology,* 89**,** 1803-1832.

GOFF, F. 1982. Valles Caldera geothermal systems, New Mexico, U.S.A. *Journal of Hydrology (Amsterdam)*, 56, 1-2, 119-136.

GOFF, F. & JANIK, C. J. 2002. Gas geochemistry of the Valles caldera region, New Mexico and comparisons with gases at Yellowstone, Long Valley and other geothermal systems. *Journal of Volcanology and Geothermal Research,* 116**,** 299-323.

GOFF, F. & KRON, A. 1980. In-progress geologic map of Canon de San Diego, Jemez Springs, New Mexico; and lithologic log of Jemez Springs geothermal well, 1:12,000. Los Alamos, New Mexico: U. S. Gov. Print. Off., Washington, DC.

GOFF, F. & SHEVENELL, L. 1987. Travertine deposits of Soda Dam, New Mexico, and their implications for the age and evolution of the Valles caldera hydrothermal system. *Geological Society of America Bulletin,* 99**,** 292-302.

GOFF, F., SHEVENELL, L., GARDNER, J. N., VUATAZ, F. D. & GRIGSBY, C. O. 1988. The hydrothermal outflow plume of Valles Caldera, New Mexico, and a comparison with other outflow plumes. *Journal of Geophysical Research,* 93**,** 6041-6058.

HANCOCK, P.L., CHALMERS, R.M.L., ALTUNEL, E., & CAKIR, Z. 1999. Travertonics: using travertines in active fault studies. *Journal of Structural Geology*, 21, 903-916.

HEINKEN, G., GOFF, F., GARDNER, J.N., & BALDRIDGE, W.S. 1990. The Valles/Toledo Caldera complex, Jemez volcanic field, New Mexico. *Annu. Rev. Earth Planet. Sci.* 18, 27-53.

HENDERSON, G.M., & SLOWEY, N.C. 2000. Evidence from U-Th dating against northern hemisphere forcing of the penultimate deglaciation. *Nature*, 404, 61-66

HORI, M., KAWAI, T., MATSUOKA, J. & KANO, A. 2009. Intra-annual perturbations of stable isotopes in tufas: Effects of hydrologic pr. *Geochemica et Cosmochimica Acta,* 73**,** 1684-1695.

HUYBERS, P. 2006. Early Pliestocene glacial cycles and the integrated summer insolation forcing. *Science*, 313, 508-511.

IMBRIE, J., HAYS, J.D., MARTINSON, D.G., MCINTYRE, A., MIX, A.C., MORLEY, J.J., PISIAS, N.G., PRELL, W.L., & SHACKLETON, N.J. 1984. The orbital theory of Pliestocene climate: support from a revised chronology of the marine $\delta^{18}O$ record. In: Berger, A., Imbrie, J.,

HAYS, J., KUKLA, G., SALTZMANN, B. (Eds.). Milankovitch and Climate, Part 1. Reidel Publishing Company, Boston, 269–305.

JOCHEMS, A. P., SHERSON, L. R., CROSSEY, L. J. & KARLSTROM, K. E. 2010. Predictive analysis of geochemical controls in an alpine stream. Eos Trans. AGU, 91, H31D-1041.

KARLSTROM, K.E., CROW, R., CROSSEY, L.J., COBLENTZ, D., VAN WIJK, J.W. 2008. Model for tectonically driven incision of the younger than 6 Ma Grand Canyon. *Geology*, 36, 11, 835-838.

KELE, S., DEMENY, A., SIKLOSY, Z., NEMETH, T., TOTH, M., & KOVACS, M.B. 2008. Chemical and stable isotope composition of recent hot-water travertines and associated thermal waters, from Egerszalok, Hungary: Depositional facies and non-equilibrium fractionation. *Sedimentary Geology*, 211, 53-72.

KELE, S., OZKUL, M., FORIZS, I., GOKGOZ, A., BAYKARA, M.O., ALCICEK, M.C., & NEMETH, T. 2011. Stable isotope geochemical study of Pamukkale travertines: New evidence of low-temperature non-equilibrium calcite-water fractionation, *Sedimentary Geology*, 238, 191-212.

KELLEY, S., KEMPTER, K. A., GOFF, F., RAMPEY, M., OSBURN, B. & FERGUSON, C. A. 2003. *Preliminary Geologic Map of the Jemez Springs 7.5 - minute quadrangle*, 1:24,000. Socorro, New Mexico: NMBGRMR Publications.

KIM, S.T. & O'NEIL, J.R. 1997. Equilibrium and nonequilibrium oxygen isotope effects in synthetic carbonates. *Geochemica et cosmochimica acta*, 61, 16, 3461-3475.

LACHNIET, M.S. 2009. Climatic and environmental controls on speleothems oxygen-isotope values, *Quaternary Science Reviews*, 28, 412-432.

LISIECKI, L.E. & RAYMO, M.E. 2005. A Pliocene-Pleistocene stack of 57 globally distributed benthic $\delta^{18}O$ records, Paleoceanography, 20, PA1003.

LEVINE, J., KARNER, D.B., & MULLER, R.A. 2001. Warming at 140 Ka: causality problem for Milankovitch. EOS. *Transactions of the American Geophysical Union* 82S, F3.

LUDWIG, K. R. 2008 Isoplot/Ex 3.7 Beta: A Geochronological Toolkit for Microsoft Excel, Berkeley Geochronology Center, Berkeley

MARTINSON, D.G., PISIAS, N.G., HAYS, J.D., IMBRIE, J., MOORE, JR. T.C. & SHACKLETON, N.J. 1987. Age dating and the orbital theory of the ice ages: development of a high-resolution 0 to 300,000-year chronostratigraphy. *Quaternary Research*, 27, 1–29.

MINISSALE, A., KERRICK, D. M., MAGRO, G., MURRELL, M. T., PALADINI, M., RIHS, S., STURCHIO, N. C., TASSI, F. & VASELLI, O. 2002. Geochemistry of Quaternary travertines in the region north of Rome (Italy): structural, hydrologic and paleoclimatic implications. *Earth and Planetary Science Letters,* 203**,** 709-728.

MOATS, W. 2004. Geology of the Soda Dam travertine deposits, Sandoval County, New Mexico, *New Mexico Geological Society Spring Meeting*.

NEWELL, D.L., CROSSEY, L.J., KARLSTROM, K.E., & FISCHER, T.P. 2005. Continental scale links between the mantle and groundwater systems of the western United States: Evidence from the travertine springs and regional He isotope data. *GSA Today*, 15, 12, 4-10.

O'BRIEN, G. R., KAUFMAN, D. S., SHARP, W. D., ATUDOREI, V., PARNELL, R. A. & CROSSEY, L. J. 2006. Oxygen isotope composition of annually banded modern and mid-Holocene travertine and evidence of paleomonsoon floods, Grand Canyon, Arizona, USA. *Quaternary Research,* 65**,** 366-379.

PARKHUSRT, D.L. 1995. User's guide to PHREEQC—A computer program for speciation,

reaction-path, advectivetransport, and inverse geochemical calculations: *U.S. Geological Survey Water Resources Investigations Report*, 95-4227, 143

PEDERSON, J.L., ANDERS, M.D., RITENHOUR, T.M., SHARP, W.D., GOSSE, J.C. & KARLSTROM, K.E. 2006. Using fill terraces to understand incision rates and evolution of the Colorado River in eastern Grand Canyon, *Arizona: Journal of Geophysical Research (Earth Surface)*, 111, F02003

PENTECOST, A. 2005. *Travertine*, Springer.

REID, K.D., GOFF, F. & COUNCE, D.A. 2003. Arsenic concentration and mass flow rate in natural waters of the Valles caldera and Jemez Mountains region, New Mexico. *New Mexico Geology*, 25, 3, 75-82

RIHS, S., CONDOMINES, M. & POIDEVIN, J. L. 2000. Long-term behaviour of continental hydrothermal systems: U-series study of hydrothermal carbonates from the French Massif Central (Allier Valley). *Geochimica Et Cosmochimica Acta,* 64**,** 3189-3199.

ROGERS, J. B. 1996. *The Fluvial Landscape Evolution of San Diego Canyon, Jemez Mountains, New Mexico.* M.S., University of New Mexico.

ROGERS, J. B., SMITH, G. A. & ROWE, H. 1996. History of formation and drainage of Pleistocene lakes in the Valles Caldera. *Guidebook - New Mexico Geological Society,* 47**,** 14-16.

ROMANEK, C.S., GROSSMAN, E.L. & MORSE, J.W. 1992. Carbon isotopic fractionation in synthetic aragonite and calcite: Effects of temperature and precipitation rate, *Geochemica et Cosmochimica Acta*, 56, 419-430.

SHARP, Z. 2007. *Principles of Stable Isotope Geochemistry,* Upper Saddle River, Pearson Education, Inc.

SPOTL, C. & VENNEMANN, T. W. 2003. Continuous-flow isotope ratio mass spectrometric analysis of carbonate minerals. *Rapid Communications is Mass Spectrometry,* 17**,** 1004-1006.

STIRLING, C.H., ESAT, T.M., LAMBECK, K. & MCCULLOCH, M.T. 1998. Timing and duration of the last interglacial: evidence for a restricted interval of widespread coral reef growth. *Earth and Planetary Science Letters*, 160, 745–762.

SUN, H. & LIU, Z. 2010. Wet-dry seasonal and spatial variations in the $\delta^{13}C$ and $\delta^{18}O$ values of the modern endogenic travertine at Baishuitai, Yunnan, SW China and their paleoclimate and paleoenvironmental implications. *Geochimica et Cosmochimica Acta,* 74**,** 1016-1029.

SZABO, B. J. 1990. Ages of Travertine Deposits in Eastern Grand Canyon National Park, Arizona. *Quaternary Research,* 34**,** 24-32.

VUATAZ, F. D. & GOFF, F. 1986. Isotope Geochemistry of thermal and nonthermal waters in the Valles Caldera, Jemez Mountains, Northern New Mexico. *Journal of Geophysical Research,* 91**,** 1835-1853.

WAGNER, J.D.M., COLE, J.E., BECK, J.W., PATCHETT, P.J., HENDERSON, G.M. & BARNETT, H.R. 2010. Moisture variability in the southwestern United States linked to abrupt glacial climate change. *Nature Geoscience*, 3, 110-113.

WINOGRAD, I.J., LANDWEHR, J.M., COPLEN, T.B., SHARP, W.D., RIGGS, A.C., LUDWIG,

K.R. & KOLESAR, P.T. 2006. Devils Hole, Nevada, $\delta^{18}O$ record extended to the mid-Holocene. *Quaternary Research*, 66, 202-212.

WRIGHT, J.D. 1999. Global climate change in marine stable isotope records, Quaternary Geology: Methods and Applications, AGU Ref. Shelf, 4, 427-433.

ZHANG, D. D., ZHANG, Y., ZHU, A. & CHENG, X. 2001. Physical Mechanisms of River Waterfall Tufa (Travertine) Formation. *Journal of Sedimentary Research,* 71**,** 205-216.

Table 1: Description, temperature, pH and measured stable isotope values of water from various springs and locations along the Jemez River (JR) in San Diego Canyon, and the Baca Wells (Figure 8).

Spring Sampled	Source	°C	pH	$\delta^{18}O$	δD
Main Hot Spring	Dyer, 2007	37.7	6.25		-16.24
Main Hot Spring	Dyer, 2007	31.4	6.89		3.36
Main Hot Spring	Dyer, 2007	29.0	7.08		-2.72
Grotto Spring	Dyer, 2007	33.8	7.22		-4.71
Grotto Spring	Dyer, 2007	32.8	7.34		-5.93
Grotto Spring	Dyer, 2007	32.0	7.34		-7.85
Main Hot Spring	Goff et al., 1988	46.8	6.71	-84.90	-1.66
Main Hot Spring	Goff et al., 1988			-10.56	-84.90
JR North of Soda Dam	Jochems et al., 2010		19.80	-11.06	-82.99
JR South of Soda Dam	Jochems et al., 2010		22.26	-11.06	-82.80
JR South of Bathhouse	Jochems et al., 2010		24.10	-11.36	-84.68
JR Spanish Queen	Jochems et al., 2010		24.50	-11.23	-84.19
JR La Junta	Jochems et al., 2010		22.10	-11.07	-83.43
JR Guadalupe	Jochems et al., 2010		28.70	-11.31	-84.65
JR San Ysidro	Jochems et al., 2010		22.70	-11.41	-86.04
JR North of Soda Dam	Jochems et al., 2010		23.50	-11.10	-82.64
JR South of Soda Dam	Jochems et al., 2010		1.70	-10.85	-82.07
JR below Battleship Rock	Jochems et al., 2010		1.00	-12.10	-89.19
JR East Fork at Battleship Rock	Jochems et al., 2010		3.40	-11.94	-86.57
JR North of Soda Dam	Jochems et al., 2010		5.00	-11.64	-84.31
JR Jemez River at VCNP	Jochems et al., 2010		63.50	-11.74	-85.42
Bathhouse Spring	Jochems et al., 2010		8.00	-11.00	-83.09
JR South of Bathhouse	Jochems et al., 2010		8.60	-11.83	-85.41
JR Spanish Queen	Jochems et al., 2010		7.60	-11.54	-86.04
JR La Junta	Jochems et al., 2010		6.60	-11.82	-86.32
JR Guadalupe	Jochems et al., 2010		9.40	-11.46	-84.73
JR San Ysidro	Jochems et al., 2010		2.20	-12.01	-88.22
JR East Fork at Battleship Rock	Jochems et al., 2010		1.00	-13.00	-94.79
JR below Battleship Rock	Jochems et al., 2010		2.10	-13.06	-94.53
JR North of Soda Dam	Jochems et al., 2010		2.90	-13.10	-95.12
JR South of Soda Dam	Jochems et al., 2010		6.00	-12.89	-94.07
JR South of Bathhouse	Jochems et al., 2010		7.50	-12.99	-95.40
JR Spanish Queen	Jochems et al., 2010		7.50	-12.76	-92.81
JR La Junta	Jochems et al., 2010		8.30	-12.60	-92.04
JR Guadalupe	Jochems et al., 2010		10.50	-12.65	-94.38
JR San Ysidro	Jochems et al., 2010			-12.15	-89.00
Snowmelt from Battle Ship Rock	Jochems et al., 2010		0.80	-10.96	-79.72
JR Hwy 4 Upstream	Jochems et al., 2010		2.10	-12.24	-89.28
JREast Fork at Battleship Rock	Jochems et al., 2010		3.50	-12.62	-89.72

Table 1: Description, temperature, pH and measured stable isotope values of water from various springs and locations along the Jemez River (JR) in San Diego Canyon, and the Baca Wells (Figure 8).

Spring Sampled	Source	°C	pH	$\delta^{18}O$	δD
JR below Battleship Rock	Jochems et al., 2010		5.20	-12.92	-94.73
JR North of Soda Dam	Jochems et al., 2010		6.80	-12.75	-92.76
JR South of Soda Dam	Jochems et al., 2010		9.90	-12.66	-94.63
JR Bridge South of Bathhouse	Jochems et al., 2010		9.60	-12.64	-91.96
JR Spanish Queen	Jochems et al., 2010		10.00	-12.58	-92.38
JR La Junta	Jochems et al., 2010		14.40	-12.43	-91.84
JR San Ysidro	Jochems et al., 2010		29.00	-12.47	-92.08
Grotto Spring	Jochems et al., 2010		26.60	-10.15	-83.50
Grotto Spring	Jochems et al., 2010		27.60	-10.36	-83.95
Main Hot Spring	Jochems et al., 2010		37.70	-10.08	-86.69
Main Hot Spring	Jochems et al., 2010		46.30	-11.13	-86.59
Main Hot Spring	Jochems et al., 2010		46.30	-10.66	-85.25
Main Hot Spring	Jochems et al., 2010		46.00	-10.69	-86.67
Snowmelt from Battleship Rock	Jochems et al., 2010			-16.50	-120.24
Main Hot Spring	Jochems et al., 2011	46.3	6.05	-86.67	-9.41
Main Hot Spring	Jochems et al., 2011	46.3	6.21	-85.25	-5.65
Main Hot Spring	Jochems et al., 2011	37.7	6.30	-86.59	-1.21
Main Hot Spring	Jochems et al., 2011	45.8	6.40	-86.69	6.24
Grotto Spring	Jochems et al., 2011	26.6	6.91	-83.95	-3.55
Grotto Spring	Jochems et al., 2011	23.2	7.29	-83.50	-2.45
Main Hot Spring	Shevenell et al., 1987	47.0	6.20		
Main Hot Spring	Shevenell et al., 1987	46.8	6.21		
Main Hot Spring	Shevenell et al., 1987	47.0	6.28		
Main Hot Spring	Shevenell et al., 1987	47.0	6.28		
Main Hot Spring	Shevenell et al., 1987	47.0	6.30		
Main Hot Spring	Shevenell et al., 1987	47.0	6.35		
Main Hot Spring	Shevenell et al., 1987	48.0	6.40		
Main Hot Spring	Shevenell et al., 1987	47.0	6.52		
Main Hot Spring	Shevenell et al., 1987	46.8	6.71		
Grotto Spring	Shevenell et al., 1987	38.0	6.80		
Main Hot Spring	Shevenell et al., 1987	47.0	7.19		
Main Hot Spring	Tafoya et al., 2012	46.0	6.26	-84.03	
River Grotto Drips	Tafoya et al., 2012	12.1	6.48	-81.14	
Waterfall Drips	Tafoya et al., 2012	22.9	6.60	-83.73	
Grotto Spring	Tafoya et al., 2012	27.6	7.02	-83.20	
Grotto Spring	This Study		47.00	-10.30	-83.20
Main Hot Spring	This Study			-10.07	-84.03
Main Hot Spring	Trainer, 1984		6.10	-84.80	
Main Hot Spring	Trainer, 1984		46.80	-10.40	-84.80

Table 1: Description, temperature, pH and measured stable isotope values of water from various springs and locations along the Jemez River (JR) in San Diego Canyon, and the Baca Wells (Figure 8).

Spring Sampled	Source	°C	pH	$\delta^{18}O$	δD
Hidden Warm Spring	Vautaz and Goff, 1986		32.00	-10.95	-84.90
Hidden Warm Spring	Vautaz and Goff, 1986		38.00	-10.65	-85.10
Grotto Spring	Vautaz and Goff, 1986		23.20	-10.65	-85.10
Main Hot Spring	Vautaz and Goff, 1986		47.00	-10.60	-84.90
Main Hot Spring	Vautaz and Goff, 1986		47.00	-10.70	-85.40
Main Hot Spring	Vautaz and Goff, 1986		47.00	-10.60	-85.20
Main Hot Spring	Vautaz and Goff, 1986		45.80	-10.35	-84.00

Table 2: Location and U-series data for travertine samples.

Sample ID	Elev. (m)	NAD	UTM ZONE	UTM E	UTM N	error (m)	Deposit
LC11_NMSDA_30	2128	NAD 83	13 S	347023	3961832		A
LC10_NMSDA_22a*	2028	NAD 83	13 S	347467	3962195	7	A
K06-SDam-1	1970	NAD 83	13 S	347530	3962205		A
LC10-NMSDA-21	2009	NAD 83	13 S	347509	3962195	6	A
LC10-NMSDA-20	2002	NAD 83	13 S	347508	3962183	6	A
K06-SDam-4	1971	NAD 83	13 S	347530	3962205		A
K06-SDam-2	1968	NAD 83	13 S	347524	3962208		A
LC11_NMSDA_34	2100	NAD 83	13 S	346849	3961645		A
LC10-NMSDA-22b	2028	NAD 83	13 S	347467	3962165	7	A
LC10-NMSDA-23a*	2047	NAD 83	13 S	347462	3962166		A
AJT11_SDA_52	2060	NAD 83	13 S	347211	3961665	3.5	A
LC11_NMSDA_32	2100	NAD 83	13 S	346849	3961645		A
LC10-NMSDA-24	2065	NAD 83	13 S	347327	3962146	4	A
AJT11_SDA_51	2071	NAD 83	13 S	347185	3961827	3.5	A
LC10-NMSDA-23a	2047	NAD 83	13 S	347462	3962166	7	A
LC10_NMSDA_22a	2028	NAD 83	13 S	347467	3962195	7	A
LC11_NMSDA_31	2128	NAD 83	13 S	347023	3961832		A
LC10-NMSDB-19	1967	NAD 83	13 S	347636	3962224		B
LC10_SDamB_25B_2a	1995	NAD 83	13 S	347678	3962218		B
LC10-SdamB-25c	1995	NAD 83	13 S	347678	3962218		B
LC10-SdamB-25a*	1995	NAD 83	13 S	347678	3962218		B
LC10_SDamB_25B_4a	1995	NAD 83	13 S	347678	3962218		B
LC10-SdamB-25b	1995	NAD 83	13 S	347678	3962218		B
LC10-SdamB-25d	1995	NAD 83	13 S	347678	3962218		B
LC10_SDamB_25B_5a	1995	NAD 83	13 S	347678	3962218		B

(*) denotes sample from Goff et al., 1987.

Table 2: Location and U-series data for travertine samples.

Sample ID	Elev. (m)	NAD	UTM ZONE	UTM E	UTM N	error (m)	Deposit
LC10-SdamB-25a	1995	NAD 83	13 S	347678	3962218		B
LC10-NMSDB-15	1949	NAD 83	13 S	347615	3962219		B
LC10_SDamB_25B_3a	1995	NAD 83	13 S	347678	3962218		B
LC10_SDamB_25B_1a	1995	NAD 83	13 S	347678	3962218		B
LC10-NMSDC-13	1961	NAD 83	13 S	347696	3962182		C
LC10-NMSDC-11	1954.5	NAD 83	13 S	347682	3962173	6	C
AJT11-SD-1	1943	NAD 83	13 S	347634	3962181		D
LC11_NMSDA_36	1940	NAD 83	13 S	347603	3962137		D
LC10-Sdam-28b	1942	NAD 83	13 S	347594	3962179		D
LC10-Sdam-28c	1942	NAD 83	13 S	347594	3962179		D
LC10-Sdam-28a	1942	NAD 83	13 S	347594	3962179		D
KLC12_SD100	1942	NAD 83	13 S	347594	3962179		D
F80-76aSD*		NAD 83	13 S	347603	3962137		D
F80-76bSD*		NAD 83	13 S	347603	3962137		D
F85-7SD*		NAD 83	13 S	347594	3962145		D
F85-3C*		NAD 83	13 S	347686	3962143		C
F85-4B*		NAD 83	13 S	347701	3962166		B
F85-5B*		NAD 83	13 S	347701	3962166		B
F80-76dA*		NAD 83	13 S	347432	3962150	2075	A
F80-76eA*		NAD 83	13 S	346939	3961698	2121	A
F80-76fA*		NAD 83	13 S	346939	3961698	2121	A
F80-76gA*		NAD 83	13 S	346997	3961839	2134	A
L85-2bA*		NAD 83	13 S	347516	3962145		A
L85-8A*		NAD 83	13 S	347367	3961609	1969	A

(*) denotes sample from Goff et al., 1987.

Table 2: Location and U-series data for travertine samples.

Sample ID	Remarks	corr age	(+) error
LC11_NMSDA_30	Top of deposit A, spar travertine.	95,661	7,565
LC10_NMSDA_22a*	82 m above Jemex River, horizontal vein of calcite.	110,605	13,620
K06-SDam-1	Calcite sill at the right end of the cave.	110,981	1,506
LC10-NMSDA-21	64 m above Jemez River.	131,546	4,437
LC10-NMSDA-20	61 m above Jemez River.	166,457	28,085
K06-SDam-4	A pour, ~8 m above strath directly above sill.	183,147	2,115
K06-SDam-2	Calcite rinds on cobbles right at the bedrock strath.	200,595	2,053
LC11_NMSDA_34	Top of horizontal basal sill in large sparite vein system, high platform.	206,563	14,614
LC10-NMSDA-22b	82 m above Jemez River, horizontal vein of calcite.	210,645	3,574
LC10-NMSDA-23a*	Stratagraphic travertine just below vein (LC10_NMSDA_22a).	286,864	7,143
AJT11_SDA_52	Travertine sparite vein sitting on Abo; base of platform.	339,407	8,398
LC11_NMSDA_32	Large sparite cliff, top of vien system.	454,661	26,925
LC10-NMSDA-24	127 m above Jemez River.	481,860	32,368
AJT11_SDA_51	Travertine sparite layer within the river gravel layer.	485,690	124,654
LC10-NMSDA-23a	Stratagraphic travertine just below vein (LC10_NMSDA_22a).	560,301	323,575
LC10_NMSDA_22a	82 m above Jemex River, horizontal vein of calcite.	>500,000	1.E+26
LC11_NMSDA_31	Micritic travertine, top of deposit A, same location as LC11_NMSDA_30.	>500,000	-
LC10-NMSDB-19	29.1 m above Jemez River, top of deposit.	77,999	1,573
LC10_SDamB_25B_2a	Lamination in LC10-SdamB-25.	92,722	508
LC10-SdamB-25c	Lamination in LC10-SdamB-25.	95,877	1,079
LC10-SdamB-25a*	Lamination in LC10-SdamB-25.	97,648	801
LC10_SDamB_25B_4a	Lamination in LC10-SdamB-25.	106,824	1,125
LC10-SdamB-25b	Lamination in LC10-SdamB-25.	117,280	1,968
LC10-SdamB-25d	Lamination in LC10-SdamB-25.	121,821	2,010
LC10_SDamB_25B_5a	Lamination in LC10-SdamB-25.	129,611	3,019

(*) denotes sample from Goff et al., 1987.

Table 2: Location and U-series data for travertine samples.

Sample ID	Remarks	corr age	(+) error
LC10-SdamB-25a	Lamination in LC10-SdamB-25.	133,967	11,297
LC10-NMSDB-15	11 m above Jemez River, 2m above exposed base.	137,491	1,051
LC10_SDamB_25B_3a	Lamination in LC10-SdamB-25.	143,991	3,405
LC10_SDamB_25B_1a	Lamination in LC10-SdamB-25.	209,611	1,709
LC10-NMSDC-13	23 m above Jemez River, top surface, 2 m below highest point of deposit.	101,235	531
LC10-NMSDC-11	16.5 m above river, directly above river gravel deposits.	102,676	479
AJT11-SD-1	Top of cone mound in North trending fissure.	2,128	32
LC11_NMSDA_36	Rind in SD, approximately 3 m in.	3,503	35
LC10-Sdam-28b	Lamination in LC10-Sdam-28.	4,681	45
LC10-Sdam-28c	Lamination in LC10-Sdam-28.	4,974	87
LC10-Sdam-28a	Lamination in LC10-Sdam-28.	5,149	43
KLC12_SD100	Vein sample cross cutting fissure vein on west side of deposit (by road); near base.	10,008	835
F80-76aSD*	Fresh Travertine, Grotto	<30	
F80-76bSD*	Travertine, inner rind, E. Soda Dam	<4000	
F85-7SD*	Travertine, inner rind, W. Soda Dam	4,800	200
F85-3C*	Spar Travertine, near base of deposit C	107,000	5,000
F85-4B*	Spar travertine, core of deposit B	58,000	3,000
F85-5B*	Travertine, near summit deposit B	98,000	7,000
F80-76dA*	Spar travertine "dike"	1,140,000	570,000
F80-76eA*	Spar travertine "sill"	215,000	40,000
F80-76fA*	Spar travertine "sill"	730,000	420,000
F80-76gA*	Pisolithic travertine, old spring	800,000	90,000
L85-2bA*	Travertine from cemented basal gravel	480,000	60,000
L85-8A*	Spar travertine "dike"	830,000	200,000

(*) denotes sample from Goff et al., 1987.

Table 2: Location and U-series data for travertine samples.

Sample ID	(-) error	U (ppm)	error	Th (ppm)	error	^{238}U ppb	error	^{232}Th pg/g	error
LC11_NMSDA_30	7,108	0.01	0.00	0.01	0.00	17.01	0.48	5,710.56	288.46
LC10_NMSDA_22a*	12,296	0.10	0.00	0.17	0.00	106.99	0.44	170,499.29	426.78
K06-SDam-1	1,489	0.29	0.00	0.04	0.00	289.46	0.68	43,943.55	117.00
LC10-NMSDA-21	4,306	0.02	0.00	0.01	0.00	14.98	0.07	5,475.11	136.76
LC10-NMSDA-20	22,803	0.04	0.00	0.09	0.00	35.81	0.08	92,010.32	232.66
K06-SDam-4	2,081	1.03	0.00	0.00	0.00	1,022.66	2.49	4,549.02	48.01
K06-SDam-2	2,023	0.99	0.00	0.00	0.00	979.45	2.32	4.44	41.81
LC11_NMSDA_34	13,059	0.16	0.00	0.21	0.00	155.50	0.41	210,856.31	1,704.95
LC10-NMSDA-22b	3,475	0.05	0.00	0.01	0.00	46.21	0.11	12,444.67	38.87
LC10-NMSDA-23a*	6,809	0.08	0.00	0.00	0.00	83.39	0.18	1,857.12	44.40
AJT11_SDA_52	7,968	0.27	0.00	0.05	0.00	265.51	0.61	48,255.57	73.37
LC11_NMSDA_32	22,315	0.08	0.00	0.00	0.00	76.64	0.11	3,400.86	46.70
LC10-NMSDA-24	26,174	0.08	0.00	0.06	0.00	83.16	0.19	62,102.42	312.89
AJT11_SDA_51	64,639	0.14	0.00	0.13	0.00	142.83	1.20	13,100.20	543.20
LC10-NMSDA-23a	84,822	0.09	0.00	0.00	0.00	86.87	0.20	2,315.02	67.69
LC10_NMSDA_22a	1.E+26	0.11	0.00	0.30	0.00	108.04	0.25	298,099.84	751.30
LC11_NMSDA_31	-	0.11	0.00	0.01	0.00	108.50	0.37	4,858.59	38.38
LC10-NMSDB-19	1,554	0.17	0.00	0.04	0.00	169.28	0.32	35,896.04	59.59
LC10_SDamB_25B_2a	506	1.82	0.00	0.11	0.00	1,810.25	0.81	113,386.80	101.79
LC10-SdamB-25c	1,070	1.13	0.00	0.16	0.00	1,120.56	1.52	162,956.06	758.01
LC10-SdamB-25a*	796	0.28	0.00	0.02	0.00	274.22	0.66	22,082.19	92.74
LC10_SDamB_25B_4a	1,116	0.49	0.00	0.08	0.00	485.02	0.17	76,620.85	333.01
LC10-SdamB-25b	1,939	0.53	0.00	0.15	0.00	526.17	0.72	149,904.76	1,462.94
LC10-SdamB-25d	1,980	0.50	0.00	0.00	0.00	491.51	0.68	2.77	47.40
LC10_SDamB_25B_5a	2,953	0.25	0.00	0.08	0.00	246.55	0.09	77,180.97	1,951.85

(*) denotes sample from Goff et al., 1987.

Table 2: Location and U-series data for travertine samples.

Sample ID	(-) error	U (ppm)	error	Th (ppm)	error	^{238}U ppb	error	^{232}Th pg/g	error
LC10-SdamB-25a	10,410	0.35	0.00	0.03	0.00	343.18	0.47	34,015.57	412.56
LC10-NMSDB-15	1,043	0.74	0.00	0.05	0.00	737.59	1.65	50,713.90	126.44
LC10_SDamB_25B_3a	3,321	0.89	0.00	0.32	0.00	879.00	0.36	316,101.94	3,272.49
LC10_SDamB_25B_1a	1,689	0.69	0.00	0.02	0.00	689.15	0.26	18,976.10	102.63
LC10-NMSDC-13	529	0.42	0.00	0.01	0.00	416.57	0.85	10,377.31	44.28
LC10-NMSDC-11	478	1.18	0.00	0.01	0.00	1,167.03	2.14	10,274.17	31.63
AJT11-SD-1	32	0.84	0.00	0.00	0.00	829.33	1.09	1,743.58	41.05
LC11_NMSDA_36	35	0.51	0.00	0.00	0.00	510.36	0.84	2,464.08	49.88
LC10-Sdam-28b	45	0.59	0.00	0.00	0.00	589.16	0.73	4,338.99	31.96
LC10-Sdam-28c	87	0.38	0.00	0.01	0.00	374.57	0.46	5,296.09	44.51
LC10-Sdam-28a	43	0.49	0.00	0.00	0.00	488.05	1.05	3,019.11	27.84
KLC12_SD100	830	0.44	0.00	0.06	0.00	435.22	0.38	60,335.50	535.30
F80-76aSD*		0.60	0.01						
F80-76bSD*		0.42	0.01						
F85-7SD*	200	0.72	0.02						
F85-3C*	5,000	0.70	0.02						
F85-4B*	3,000	0.53	0.02						
F85-5B*	7,000	0.23	0.01						
F80-76dA*	210,000	0.12	0.00						
F80-76eA*	40,000	0.37	0.00						
F80-76fA*	190,000	0.03	0.00						
F80-76gA*	70,000	0.51	0.01						
L85-2bA*	50,000	2.20	0.07						
L85-8A*	120,000	0.17	0.01						

(*) denotes sample from Goff et al., 1987.

Table 2: Location and U-series data for travertine samples.

Sample ID	δ^{234} measured	error	δ234 intial	(+) error	(-) error	$^{230}Th/^{232}Th$ ppm	error	$[^{230}Th/^{238}U]$
LC11_NMSDA_30	-1,388.60	132.60	-953.90	146.60	958.30	32.53	1.77	0.66
LC10_NMSDA_22a*	343.50	4.30	681.90	13.20	12.90	12.63	0.00	1.28
K06-SDam-1	946.90	1.70	-	-	-	146.17	1.00	1.34
LC10-NMSDA-21	1,040.30	13.70	1,527.20	26.60	26.20	71.36	2.00	1.58
LC10-NMSDA-20	308.90	1.30	593.10	6.10	5.90	7.86	0.00	1.22
K06-SDam-4	259.20	1.40	-	-	-	3,973.98	45.00	1.07
K06-SDam-2	393.30	1.50	-	-	-	4.55E+06	4.28E+07	1.25
LC11_NMSDA_34	258.40	2.90	583.80	12.10	11.70	15.13	0.00	1.24
LC10-NMSDA-22b	281.60	1.10	518.40	4.20	4.10	71.44	0.00	1.17
LC10-NMSDA-23a*	157.07	3.67	353.34	10.97	10.66	828.01	19.98	1.12
AJT11_SDA_52	111.70	2.20	312.10	13.90	12.60	105.32	0.00	1.11
LC11_NMSDA_32	114.60	1.00	361.30	18.00	15.30	420.05	6.00	1.13
LC10-NMSDA-24	178.60	1.10	724.20	76.60	55.80	27.33	0.00	1.24
AJT11_SDA_51	47.40	3.30	200.20	137.90	41.40	19.00	0.00	1.06
LC10-NMSDA-23a	159.80	1.10	779.80	1,192.30	166.70	755.08	23.00	1.22
LC10_NMSDA_22a	141.40	0.70	-	-	-	7.30	0.00	1.22
LC11_NMSDA_31	61.50	2.60	-	-	-	470.43	4.00	1.28
LC10-NMSDB-19	869.30	2.40	1,092.90	3.40	3.40	80.05	0.00	1.03
LC10_SDamB_25B_2a	989.20	2.00	1,287.90	2.80	2.80	320.00	1.00	1.22
LC10-SdamB-25c	920.70	2.80	1,213.80	4.00	4.00	136.98	1.00	1.21
LC10-SdamB-25a*	811.90	4.10	1,081.30	6.00	6.00	243.69	1.00	1.16
LC10_SDamB_25B_4a	970.50	2.00	1,319.40	3.30	3.30	139.00	1.00	1.33
LC10-SdamB-25b	897.10	1.40	1,262.90	3.10	3.10	79.07	1.00	1.36
LC10-SdamB-25d	934.00	1.30	1,332.20	3.30	3.20	4.17E+06	7.13E+07	1.43
LC10_SDamB_25B_5a	1,032.30	2.00	1,503.80	10.80	10.60	82.00	2.00	1.56

(*) denotes sample from Goff et al., 1987.

Table 2: Location and U-series data for travertine samples.

Sample ID	δ^{234} measured	error	δ234 intial	(+) error	(-) error	$^{230}Th/^{232}Th$ ppm	error	$[^{230}Th/^{238}U]$
LC10-SdamB-25a	896.60	2.80	1,313.90	43.20	38.60	242.55	12.00	1.46
LC10-NMSDB-15	845.40	1.20	1,250.00	3.80	3.80	343.89	1.00	1.43
LC10_SDamB_25B_3a	981.50	2.00	1,491.40	11.90	11.60	74.00	1.00	1.61
LC10_SDamB_25B_1a	853.20	1.90	1,542.70	8.20	8.10	1,055.00	7.00	1.76
LC10-NMSDC-13	1,040.50	2.40	1,386.40	3.80	3.80	874.30	4.00	1.32
LC10-NMSDC-11	929.20	1.30	1,242.50	2.40	2.40	2,349.68	9.00	1.25
AJT11-SD-1	1,400.00	0.90	1,408.50	0.90	0.90	366.64	10.00	0.05
LC11_NMSDA_36	1,412.20	2.40	1,426.40	2.40	2.40	263.28	6.00	0.08
LC10-Sdam-28b	1,490.10	1.30	1,510.10	1.30	1.30	237.22	2.00	0.11
LC10-Sdam-28c	1,449.70	2.50	1,470.50	2.50	2.50	129.89	1.00	0.11
LC10-Sdam-28a	1,482.50	7.40	1,504.80	7.50	7.50	314.74	3.00	0.12
KLC12_SD100	1,412.20	2.40	1,459.50	2.50	2.50	29.38	0.26	0.25
F80-76aSD*								
F80-76bSD*								
F85-7SD*								
F85-3C*								
F85-4B*								
F85-5B*								
F80-76dA*								
F80-76eA*								
F80-76fA*								
F80-76gA*								
L85-2bA*								
L85-8A*								

(*) denotes sample from Goff et al., 1987.

Table 2: Location and U-series data for travertine samples.

Sample ID	2σ error	uncorr age	(+) error	(-) error
LC11_NMSDA_30	0.02	105,079	6,699	6,345
LC10_NMSDA_22a*	0.01	139,388	1,430	1,416
K06-SDam-1	0.01	2.19E+27	1.31E+25	1.31E+25
LC10-NMSDA-21	0.02	135,854	4,019	3,912
LC10-NMSDA-20	0.01	230,822	3,280	3,201
K06-SDam-4	0.01	2.19E+27	1.31E+25	1.31E+25
K06-SDam-2	0.01	2.19E+27	1.31E+25	1.31E+25
LC11_NMSDA_34	0.01	237,062	3,802	3,706
LC10-NMSDA-22b	0.01	215,946	2,523	2,475
LC10-NMSDA-23a*	0.00	287,344	7,170	6,834
AJT11_SDA_52	0.01	343,216	8,455	8,021
LC11_NMSDA_32	0.01	406,395	17,010	15,034
LC10-NMSDA-24	0.01	495,369	35,540	28,254
AJT11_SDA_51	0.01	510,731	184,977	76,603
LC10-NMSDA-23a	0.01	560,737	328,284	85,039
LC10_NMSDA_22a	0.01	3.20E+25	1.61E+25	1.13E+25
LC11_NMSDA_31	0.01	7.97E+26	2.42E+25	2.39E+25
LC10-NMSDB-19	0.01	80,995	518	516
LC10_SDamB_25B_2a	0.00	93,522	316	316
LC10-SdamB-25c	0.00	97,809	496	494
LC10-SdamB-25a*	0.26	98,738	596	593
LC10_SDamB_25B_4a	0.00	108,828	526	524
LC10-SdamB-25b	0.00	121,018	669	666
LC10-SdamB-25d	0.01	125,630	706	703
LC10_SDamB_25B_5a	0.02	133,324	2,445	2,402

(*) denotes sample from Goff et al., 1987.

Table 2: Location and U-series data for travertine samples.

Sample ID	2σ error	uncorr age	(+) error	(-) error
LC10-SdamB-25a	0.07	135,222	11,390	10,488
LC10-NMSDB-15	0.01	138,385	958	952
LC10_SDamB_25B_3a	0.02	148,290	2,727	2,673
LC10_SDamB_25B_1a	0.01	209,926	1,706	1,686
LC10-NMSDC-13	0.00	101,539	511	509
LC10-NMSDC-11	0.00	102,791	477	475
AJT11-SD-1	0.00	2,141	29	29
LC11_NMSDA_36	0.00	3,531	20	20
LC10-Sdam-28b	0.00	4,722	15	15
LC10-Sdam-28c	0.00	5,053	24	24
LC10-Sdam-28a	0.00	5,290	25	25
KLC12_SD100	0.00	11,663	128	128
F80-76aSD*				
F80-76bSD*				
F85-7SD*				
F85-3C*				
F85-4B*				
F85-5B*				
F80-76dA*				
F80-76eA*				
F80-76fA*				
F80-76gA*				
L85-2bA*				
L85-8A*				

(*) denotes sample from Goff et al., 1987.

Table 3: Measured stable isotope values of $\delta^{18}O$ and $\delta^{13}C$ of travertine samples.

Sample ID	Deposit	$\delta^{13}C$	$\delta^{18}O$	AGE	+ error	- error
LC11-NMSDA 30	A	3.82	-14.71	95,661	7,565	7,108
LC10-NMSDA-22a	A	3.25	-12.04	110,605	13,620	12,296
LC11-NMSDA 34	A	1.95	-17.44	206,563	14,614	13,059
LC10-NMSDA-22b	A	4.05	-13.36	210,645	3,574	3,475
LC10-NMSDA-23 a	A	4.36	-10.01	286,864	7,143	6,809
AJT11-SDA 52	A	2.67	-18.41	339,407	8,398	7,968
LC10-NMSDA-24	A	4.42	-10.20	481,860	32,368	26,174
AJT11-SDA 51	A	3.28	-17.76	485,690	124,654	64,639
LC11-NMSDA 31	A	5.02	-12.56	>500,000		
LC10-NMSDA-23 b	A	4.08	-10.12			
K06-SDAM-1	A_i	4.93	-9.99	110,981	1,506	1,489
LC10-Sdam 21	A_i	2.44	-15.03	131,546	4,437	4,306
LC10-NMSDA-20	A_i	8.35	-6.65	166,457	28,085	22,803
L06-SDAM-4	A_i	7.89	-11.00	183,147	2,115	2,081
K06-SDAM-2	A_i	1.43	-19.04	200,595	2,053	2,023
LC10-NMSDB-19	B	5.52	-10.41	77,999	1,573	1,554
LC10-NMSDB-15	B	5.77	-9.50	137,491	1,051	1,043
LC10-NMSDB-17	B	3.95	-13.06			
LC10_SdamB-26c	B	6.92	-11.33			
LC10-SdamB-26a	B	7.39	-10.26			
LC10_SdamB-26b	B	2.48	-16.07			
LC10_SdamB-27a	B	3.45	-14.29			
LC10-SdamB-27 b	B	4.92	-13.19			
LC10-SdamB-27 c	B	3.08	-14.63			
LC10-NMSDB-16	B	5.14	-11.29			
LC10-NMSDB-18	B	4.49	-12.33			
LC10 Sdam 25B 30	B - Vein	8.99	-8.07	95,877	1,079	1,070
LC10 Sdam 25Ba	B - Vein	10.14	-6.12			
LC10 Sdam 25B 1	B - Vein	6.58	-7.67			
LC10 Sdam 25B 2	B - Vein	6.27	-8.69			
LC10 Sdam 25B 3	B - Vein	6.30	-8.39			
LC10 Sdam 25B 4	B - Vein	6.54	-8.93			
LC10 Sdam 25B 5	B - Vein	6.16	-9.00			
LC10 Sdam 25B 6	B - Vein	7.15	-8.31			
LC10 Sdam 25B 7	B - Vein	8.97	-7.62			
LC10 Sdam 25B 8	B - Vein	7.49	-8.21			
LC10 Sdam 25B 9	B - Vein	11.34	-6.76			
LC10 Sdam 25B 10	B - Vein	10.88	-6.30			
LC10 Sdam 25B 12	B - Vein	8.51	-8.06			

Table 3: Measured stable isotope values of $\delta^{18}O$ and $\delta^{13}C$ of travertine samples.

Sample ID	Deposit	$\delta^{13}C$	$\delta^{18}O$	AGE	+ error	- error
LC10 Sdam 25B 13	B - Vein	9.08	-6.93			
LC10 Sdam 25B 14	B - Vein	9.74	-6.61			
LC10 Sdam 25B 15	B - Vein	11.25	-6.67			
LC10 Sdam 25B 16	B - Vein	7.34	-8.70			
LC10 Sdam 25B 17	B - Vein	9.29	-7.19			
LC10 Sdam 25B 18	B - Vein	8.39	-7.79			
LC10 Sdam 25B 19	B - Vein	10.39	-7.00			
LC10 Sdam 25B 20	B - Vein	11.69	-6.69			
LC10 Sdam 25B 21	B - Vein	9.40	-7.83			
LC10 Sdam 25B 22	B - Vein	9.99	-7.59			
LC10 Sdam 25B 23	B - Vein	10.27	-6.98			
LC10 Sdam 25B 24	B - Vein	7.49	-7.76			
LC10 Sdam 25B 25	B - Vein	8.40	-8.08			
LC10 Sdam 25B 26	B - Vein	8.21	-7.42			
LC10 Sdam 25B 27	B - Vein	9.65	-7.34			
LC10 Sdam 25B 28	B - Vein	5.42	-9.26			
LC10 Sdam 25B 29	B - Vein	9.67	-7.33			
LC10 Sdam 25B 31	B - Vein	11.37	-5.58			
LC10-SDamB-25c	B - Vein	6.73	-9.69			
LC10-SdamB-25b	B - Vein	11.29	-6.52			
LC10-SDamB-25d	B - Vein	7.86	-9.12			
LC10-NMSDC-13	C	4.40	-13.30	101,235	531	529
LC10-NMSDC-11	C	4.73	-13.23	102,676	479	478
LC10-NMSDC-10	C	4.07	-9.88			
LC10-NMSDC-12	C	3.90	-11.21			
AJT-SD-1	SD	3.92	-10.23	2,128	32	32
LC11-NMSDA 36	SD	5.57	-11.24	3,503	35	35
LC10-Sdam-28 b	SD	2.45	-11.28	4,681	45	45
LC10-Sdam-28 c	SD	2.56	-10.53	4,974	87	87
LC10-Sdam-28 a	SD	2.58	-10.72	5,149	43	43
LC10-NMSD-5	SD	2.85	-10.16			
LC10-NMSD-6	SD	2.68	-10.67			
AJT-SD-2	SD	3.37	-8.90			
AJT11_SDAM_40	SD Modern	4.66	-12.66			
AJT11_SDAM_41	SD Modern	5.31	-10.92			
AJT11_SDAM_43	SD Modern	4.78	-11.48			
AJT11_SDAM_44	SD Modern	7.02	-6.92			

Table 4: Paleotemperature calculations using temperature dependent fractionation factors by Demeny et al., 2010; Kele et al., 2011; Kim and O'Neil, 1997 and Romanek et al., 1992 (eq. 7, 8, 9; APPENDIX D).

Sample	Deposit	Calcite $d18O_{PDB}$	Water $d18O_{SMOW}$	Water $d18O_{PDB}$	PDB $\alpha_{cal\text{-}water}$	$1000\ln\alpha$
LC10-NMSDA-22a	A	-12.04	-10	-39.68	1.03	28.38
LC10-NMSDA-22b	A	-13.36	-10	-39.68	1.03	27.05
LC10-NMSDA-23 a	A	-10.01	-10	-39.68	1.03	30.44
LC10-NMSDA-23 b	A	-10.12	-10	-39.68	1.03	30.32
LC10-NMSDA-24	A	-10.20	-10	-39.68	1.03	30.24
LC11-NMSDA 31	A	-12.56	-10	-39.68	1.03	27.86
LC11-NMSDA 31	A	-12.79	-10	-39.68	1.03	27.62
LC11-NMSDA 30	A	-14.71	-10	-39.68	1.03	25.68
LC11-NMSDA 34	A	-17.44	-10	-39.68	1.02	22.90
AJT11-SDA 51	A	-17.76	-10	-39.68	1.02	22.58
AJT11-SDA 52	A	-18.41	-10	-39.68	1.02	21.92
K06-SDAM-1	Ai	-9.99	-10	-39.68	1.03	30.45
K06-SDAM-2	Ai	-19.04	-10	-39.68	1.02	21.27
L06-SDAM-4	Ai	-11.00	-10	-39.68	1.03	29.43
LC10-NMSDA-20	Ai	-6.65	-10	-39.68	1.03	33.82
LC10-Sdam 21	Ai	-15.03	-10	-39.68	1.03	25.34
LC10_SdamB-26b	B	-16.07	-10	-39.68	1.02	24.29
LC10_SdamB-26c	B	-11.33	-10	-39.68	1.03	29.10
LC10_SdamB-26c	B	-11.33	-10	-39.68	1.03	29.10
LC10_SdamB-27a	B	-14.29	-10	-39.68	1.03	26.10
LC10-NMSDB-15	B	-9.50	-10	-39.68	1.03	30.95
LC10-NMSDB-16	B	-11.29	-10	-39.68	1.03	29.13
LC10-NMSDB-17	B	-13.06	-10	-39.68	1.03	27.34
LC10-NMSDB-18	B	-12.33	-10	-39.68	1.03	28.08
LC10-NMSDB-19	B	-10.41	-10	-39.68	1.03	30.03
LC10-SdamB-25b	B	-6.52	-10	-39.68	1.03	33.95
LC10-SDamB-25c	B	-9.69	-10	-39.68	1.03	30.76
LC10-SDamB-25d	B	-9.12	-10	-39.68	1.03	31.33
LC10-SdamB-26a	B	-10.26	-10	-39.68	1.03	30.18
LC10-SdamB-27 b	B	-13.19	-10	-39.68	1.03	27.21
LC10-SdamB-27 c	B	-14.63	-10	-39.68	1.03	25.76
LC10 Sdam 25B 31	B - Vein	-5.58	-10	-39.68	1.04	34.90
LC10 Sdam 25B A	B - Vein	-6.12	-10	-39.68	1.03	34.35
LC10 Sdam 25B 10	B - Vein	-6.30	-10	-39.68	1.03	34.17
LC10-SdamB-25b	B - Vein	-6.52	-10	-39.68	1.03	33.95
LC10 Sdam 25B 14	B - Vein	-6.61	-10	-39.68	1.03	33.86

Table 4: Paleotemperature calculations using temperature dependent fractionation factors by Demeny et al., 2010; Kele et al., 2011; Kim and O'Neil, 1997 and Romanek et al., 1992 (eq. 7, 8, 9; APPENDIX D).

Sample	Deposit	Calcite $d18O_{PDB}$	Water $d18O_{SMOW}$	Water $d18O_{PDB}$	PDB $\alpha_{cal\text{-}water}$	$1000ln\alpha$
LC10 Sdam 25B 15	B - Vein	-6.67	-10	-39.68	1.03	33.80
LC10 Sdam 25B 20	B - Vein	-6.69	-10	-39.68	1.03	33.78
LC10 Sdam 25B 9	B - Vein	-6.76	-10	-39.68	1.03	33.70
LC10 Sdam 25B 13	B - Vein	-6.93	-10	-39.68	1.03	33.54
LC10 Sdam 25B 23	B - Vein	-6.98	-10	-39.68	1.03	33.49
LC10 Sdam 25B 19	B - Vein	-7.00	-10	-39.68	1.03	33.47
LC10 Sdam 25B 17	B - Vein	-7.19	-10	-39.68	1.03	33.27
LC10 Sdam 25B 29	B - Vein	-7.33	-10	-39.68	1.03	33.13
LC10 Sdam 25B 27	B - Vein	-7.34	-10	-39.68	1.03	33.13
LC10 Sdam 25B 26	B - Vein	-7.42	-10	-39.68	1.03	33.04
LC10 Sdam 25B 22	B - Vein	-7.59	-10	-39.68	1.03	32.87
LC10 Sdam 25B 7	B - Vein	-7.62	-10	-39.68	1.03	32.84
LC10 Sdam 25B 1	B - Vein	-7.67	-10	-39.68	1.03	32.79
LC10 Sdam 25B 24	B - Vein	-7.76	-10	-39.68	1.03	32.70
LC10 Sdam 25B 18	B - Vein	-7.79	-10	-39.68	1.03	32.68
LC10 Sdam 25B 21	B - Vein	-7.83	-10	-39.68	1.03	32.63
LC10 Sdam 25B 12	B - Vein	-8.06	-10	-39.68	1.03	32.40
LC10 Sdam 25B 30	B - Vein	-8.07	-10	-39.68	1.03	32.39
LC10 Sdam 25B 25	B - Vein	-8.08	-10	-39.68	1.03	32.38
LC10 Sdam 25B 8	B - Vein	-8.21	-10	-39.68	1.03	32.25
LC10 Sdam 25B 6	B - Vein	-8.31	-10	-39.68	1.03	32.15
LC10 Sdam 25B 3	B - Vein	-8.39	-10	-39.68	1.03	32.07
LC10 Sdam 25B 2	B - Vein	-8.69	-10	-39.68	1.03	31.76
LC10 Sdam 25B 16	B - Vein	-8.70	-10	-39.68	1.03	31.75
LC10 Sdam 25B 4	B - Vein	-8.93	-10	-39.68	1.03	31.52
LC10 Sdam 25B 5	B - Vein	-9.00	-10	-39.68	1.03	31.46
LC10-SDamB-25d	B - Vein	-9.12	-10	-39.68	1.03	31.33
LC10 Sdam 25B 28	B - Vein	-9.26	-10	-39.68	1.03	31.19
LC10-SDamB-25c	B - Vein	-9.69	-10	-39.68	1.03	30.76
LC10-NMSDC-10	C	-9.88	-10	-39.68	1.03	30.57
LC10-NMSDC-11	C	-13.23	-10	-39.68	1.03	27.18
LC10-NMSDC-12	C	-11.21	-10	-39.68	1.03	29.22
LC10-NMSDC-13	C	-13.30	-10	-39.68	1.03	27.11
LC11-NMSDA 36	D	-11.24	-10	-39.68	1.03	29.18
LC11-NMSDA 36	D	-11.49	-10	-39.68	1.03	28.93
AJT11-SDAM 40	Modern	-12.66	-10	-39.68	1.03	27.75

Table 4: Paleotemperature calculations using temperature dependent fractionation factors by Demeny et al., 2010; Kele et al., 2011; Kim and O'Neil, 1997 and Romanek et al., 1992 (eq. 7, 8, 9; APPENDIX D).

Sample	Deposit	Calcite $d18O_{PDB}$	Water $d18O_{SMOW}$	Water $d18O_{PDB}$	PDB $\alpha_{cal\text{-}water}$	$1000\ln\alpha$
AJT11-SDAM 41	Modern	-10.92	-10	-39.68	1.03	29.51
AJT11-SDAM 44	Modern	-6.92	-10	-39.68	1.03	33.55
AJT11-Sdam 43a	Modern	-11.48	-10	-39.68	1.03	28.94
AJT11-SDAM 40	Modern	-12.66	-10.06622	-39.75	1.03	27.82
AJT11-SDAM 41	Modern	-10.92	-10.30356	-39.98	1.03	29.82
AJT11-SDAM 44	Modern	-6.92	-10.05897	-39.74	1.03	33.61
AJT-SD-1	SD	-10.23	-10	-39.68	1.03	30.21
AJT-SD-2	SD	-8.90	-10	-39.68	1.03	31.55
LC10-NMSD-5	SD	-10.16	-10	-39.68	1.03	30.28
LC10-NMSD-6	SD	-10.67	-10	-39.68	1.03	29.76
LC10-Sdam-28 a	SD	-10.72	-10	-39.68	1.03	29.71
LC10-Sdam-28 b	SD	-11.28	-10	-39.68	1.03	29.15
LC10-Sdam-28 c	SD	-10.53	-10	-39.68	1.03	29.91

Table 4: Paleotemperature calculations using temperature dependent fractionation factors by Demeny et al., 2010; Kele et al., 2011; Kim and O'Neil, 1997 and Romanek et al., 1992 (eq. 7, 8, 9; APPENDIX D).

	Demény et al., 2010		Kele et al., 2011		Kim & O'Neil, 1997	
	Temp.	Temp.	Temp.	Temp.	Temp.	Temp.
Sample	K	°C	K	°C	K	°C
LC10-NMSDA-22a	303.33	30.18	320.76	47.61	296.55	23.40
LC10-NMSDA-22b	310.47	37.32	328.58	55.43	303.20	30.05
LC10-NMSDA-23 a	292.95	19.80	309.74	36.59	286.85	13.70
LC10-NMSDA-23 b	293.53	20.38	310.35	37.20	287.40	14.25
LC10-NMSDA-24	293.89	20.74	310.72	37.57	287.73	14.58
LC11-NMSDA 31	306.10	32.95	323.77	50.62	299.13	25.98
LC11-NMSDA 31	307.34	34.19	325.13	51.98	300.29	27.14
LC11-NMSDA 30	318.16	45.01	337.23	64.08	310.35	37.20
LC11-NMSDA 34	334.96	61.81	357.07	83.92	325.91	52.76
AJT11-SDA 51	337.03	63.88	359.63	86.48	327.83	54.68
AJT11-SDA 52	341.36	68.21	365.02	91.87	331.83	58.68
K06-SDAM-1	292.89	19.74	309.67	36.52	286.79	13.64
K06-SDAM-2	345.71	72.56	370.54	97.39	335.84	62.69
L06-SDAM-4	297.92	24.77	314.97	41.82	291.50	18.35
LC10-NMSDA-20	277.31	4.16	293.82	20.67	272.18	-0.97
LC10-Sdam 21	320.07	46.92	339.42	66.27	312.13	38.98
LC10_SdamB-26b	326.32	53.17	346.70	73.55	317.92	44.77
LC10_SdamB-26c	299.62	26.47	316.78	43.63	293.09	19.94
LC10_SdamB-26c	299.62	26.47	316.78	43.63	293.09	19.94
LC10_SdamB-27a	315.74	42.59	334.48	61.33	308.10	34.95
LC10-NMSDB-15	290.48	17.33	307.17	34.02	284.54	11.39
LC10-NMSDB-16	299.44	26.29	316.58	43.43	292.91	19.76
LC10-NMSDB-17	308.85	35.70	326.79	53.64	301.70	28.55
LC10-NMSDB-18	304.89	31.74	322.45	49.30	298.00	24.85
LC10-NMSDB-19	294.93	21.78	311.82	38.67	288.70	15.55
LC10-SdamB-25b	276.76	3.61	293.27	20.12	271.66	-1.49
LC10-SDamB-25c	291.38	18.23	308.11	34.96	285.38	12.23
LC10-SDamB-25d	288.64	15.49	305.28	32.13	282.82	9.67
LC10-SdamB-26a	294.19	21.04	311.04	37.89	288.01	14.86
LC10-SdamB-27 b	309.55	36.40	327.57	54.42	302.35	29.20
LC10-SdamB-27 c	317.69	44.54	336.70	63.55	309.92	36.77
LC10 Sdam 25B 31	272.69	-0.46	289.26	16.11	267.84	-5.31
LC10 Sdam 25B A	275.02	1.87	291.55	18.40	270.03	-3.12
LC10 Sdam 25B 10	275.80	2.65	292.31	19.16	270.75	-2.40
LC10-SdamB-25b	276.76	3.61	293.27	20.12	271.66	-1.49
LC10 Sdam 25B 14	277.13	3.98	293.64	20.49	272.01	-1.14

Table 4: Paleotemperature calculations using temperature dependent fractionation factors by Demeny et al., 2010; Kele et al., 2011; Kim and O'Neil, 1997 and Romanek et al., 1992 (eq. 7, 8, 9; APPENDIX D).

	Demény et al., 2010		Kele et al., 2011		Kim & O'Neil, 1997	
	Temp.	Temp.	Temp.	Temp.	Temp.	Temp.
Sample	K	°C	K	°C	K	°C
LC10 Sdam 25B 15	277.40	4.25	293.91	20.76	272.26	-0.89
LC10 Sdam 25B 20	277.51	4.36	294.01	20.86	272.36	-0.79
LC10 Sdam 25B 9	277.83	4.68	294.33	21.18	272.67	-0.48
LC10 Sdam 25B 13	278.55	5.40	295.05	21.90	273.34	0.19
LC10 Sdam 25B 23	278.77	5.62	295.27	22.12	273.55	0.40
LC10 Sdam 25B 19	278.86	5.71	295.36	22.21	273.64	0.49
LC10 Sdam 25B 17	279.74	6.59	296.24	23.09	274.46	1.31
LC10 Sdam 25B 29	280.36	7.21	296.87	23.72	275.05	1.90
LC10 Sdam 25B 27	280.38	7.23	296.88	23.73	275.06	1.91
LC10 Sdam 25B 26	280.76	7.61	297.27	24.12	275.42	2.27
LC10 Sdam 25B 22	281.52	8.37	298.03	24.88	276.13	2.98
LC10 Sdam 25B 7	281.68	8.53	298.19	25.04	276.28	3.13
LC10 Sdam 25B 1	281.89	8.74	298.40	25.25	276.48	3.33
LC10 Sdam 25B 24	282.31	9.16	298.82	25.67	276.87	3.72
LC10 Sdam 25B 18	282.42	9.27	298.93	25.78	276.98	3.83
LC10 Sdam 25B 21	282.62	9.47	299.14	25.99	277.17	4.02
LC10 Sdam 25B 12	283.67	10.52	300.20	27.05	278.15	5.00
LC10 Sdam 25B 30	283.72	10.57	300.25	27.10	278.20	5.05
LC10 Sdam 25B 25	283.75	10.60	300.28	27.13	278.23	5.08
LC10 Sdam 25B 8	284.35	11.20	300.89	27.74	278.79	5.64
LC10 Sdam 25B 6	284.82	11.67	301.37	28.22	279.23	6.08
LC10 Sdam 25B 3	285.20	12.05	301.76	28.61	279.59	6.44
LC10 Sdam 25B 2	286.63	13.48	303.21	30.06	280.93	7.78
LC10 Sdam 25B 16	286.67	13.52	303.25	30.10	280.97	7.82
LC10 Sdam 25B 4	287.75	14.60	304.36	31.21	281.98	8.83
LC10 Sdam 25B 5	288.06	14.91	304.68	31.53	282.27	9.12
LC10-SDamB-25d	288.64	15.49	305.28	32.13	282.82	9.67
LC10 Sdam 25B 28	289.31	16.16	305.97	32.82	283.44	10.29
LC10-SDamB-25c	291.38	18.23	308.11	34.96	285.38	12.23
LC10-NMSDC-10	292.31	19.16	309.07	35.92	286.25	13.10
LC10-NMSDC-11	309.76	36.61	327.79	54.64	302.54	29.39
LC10-NMSDC-12	299.01	25.86	316.13	42.98	292.51	19.36
LC10-NMSDC-13	310.13	36.98	328.21	55.06	302.89	29.74
LC11-NMSDA 36	299.18	26.03	316.31	43.16	292.67	19.52
LC11-NMSDA 36	300.46	27.31	317.67	44.52	293.87	20.72
AJT11-SDAM 40	306.65	33.50	324.38	51.23	299.65	26.50

Table 4: Paleotemperature calculations using temperature dependent fractionation factors by Demeny et al., 2010; Kele et al., 2011; Kim and O'Neil, 1997 and Romanek et al., 1992 (eq. 7, 8, 9; APPENDIX D).

	Demény et al., 2010		Kele et al., 2011		Kim & O'Neil, 1997	
Sample	Temp. K	Temp. °C	Temp. K	Temp. °C	Temp. K	Temp. °C
AJT11-SDAM 41	297.53	24.38	314.56	41.41	291.13	17.98
AJT11-SDAM 44	278.52	5.37	295.02	21.87	273.31	0.16
AJT11-Sdam 43a	300.42	27.27	317.64	44.49	293.84	20.69
AJT11-SDAM 40	306.30	33.15	323.99	50.84	299.32	26.17
AJT11-SDAM 41	296.00	22.85	312.93	39.78	289.70	16.55
AJT11-SDAM 44	278.26	5.11	294.76	21.61	273.07	-0.08
AJT-SD-1	294.05	20.90	310.89	37.74	287.88	14.73
AJT-SD-2	287.60	14.45	304.21	31.06	281.84	8.69
LC10-NMSD-5	293.71	20.56	310.53	37.38	287.56	14.41
LC10-NMSD-6	296.25	23.10	313.21	40.06	289.94	16.79
LC10-Sdam-28 a	296.51	23.36	313.47	40.32	290.18	17.03
LC10-Sdam-28 b	299.36	26.21	316.50	43.35	292.85	19.70
LC10-Sdam-28 c	295.55	22.40	312.47	39.32	289.28	16.13

Table 4: Paleotemperature calculations using temperature dependent fractionation factors by Demeny et al., 2010; Kele et al., 2011; Kim and O'Neil, 1997 and Romanek et al., 1992 (eq. 7, 8, 9; APPENDIX D).

	Romanek et al., 1992				
	Calcite	CO_2	PDB		Temp.
Sample	$d13C_{PDB}$	$d13C_{PDB}$	$\alpha_{CO2\text{-}water}$	1000lnα	°C
LC10-NMSDA-22a	-12.04	-4.9	0.99	-7.20	159.84
LC10-NMSDA-22b	-13.36	-4.9	0.99	-8.53	170.95
LC10-NMSDA-23 a	-10.01	-4.9	0.99	-5.14	142.71
LC10-NMSDA-23 b	-10.12	-4.9	0.99	-5.26	143.70
LC10-NMSDA-24	-10.20	-4.9	0.99	-5.34	144.31
LC11-NMSDA 31	-12.56	-4.9	0.99	-7.73	164.21
LC11-NMSDA 31	-12.79	-4.9	0.99	-7.96	166.16
LC11-NMSDA 30	-14.71	-4.9	0.99	-9.91	182.38
LC11-NMSDA 34	-17.44	-4.9	0.99	-12.68	205.49
AJT11-SDA 51	-17.76	-4.9	0.99	-13.00	208.19
AJT11-SDA 52	-18.41	-4.9	0.99	-13.67	213.71
K06-SDAM-1	-9.99	-4.9	0.99	-5.13	142.60
K06-SDAM-2	-19.04	-4.9	0.99	-14.31	219.11
L06-SDAM-4	-11.00	-4.9	0.99	-6.15	151.06
LC10-NMSDA-20	-6.65	-4.9	1.00	-1.76	114.48
LC10-Sdam 21	-15.03	-4.9	0.99	-10.24	185.13
LC10_SdamB-26b	-16.07	-4.9	0.99	-11.29	193.90
LC10_SdamB-26c	-11.33	-4.9	0.99	-6.48	153.85
LC10_SdamB-26c	-11.33	-4.9	0.99	-6.48	153.85
LC10_SdamB-27a	-14.29	-4.9	0.99	-9.48	178.84
LC10-NMSDB-15	-9.50	-4.9	1.00	-4.63	138.45
LC10-NMSDB-16	-11.29	-4.9	0.99	-6.45	153.55
LC10-NMSDB-17	-13.06	-4.9	0.99	-8.24	168.49
LC10-NMSDB-18	-12.33	-4.9	0.99	-7.50	162.31
LC10-NMSDB-19	-10.41	-4.9	0.99	-5.55	146.07
LC10-SdamB-25b	-6.52	-4.9	1.00	-1.63	113.42
LC10-SDamB-25c	-9.69	-4.9	1.00	-4.82	140.02
LC10-SDamB-25d	-9.12	-4.9	1.00	-4.25	135.24
LC10-SdamB-26a	-10.26	-4.9	0.99	-5.40	144.82
LC10-SdamB-27 b	-13.19	-4.9	0.99	-8.37	169.56
LC10-SdamB-27 c	-14.63	-4.9	0.99	-9.82	181.70
LC10 Sdam 25B 31	-5.58	-4.9	1.00	-0.68	105.52
LC10 Sdam 25B A	-6.12	-4.9	1.00	-1.23	110.07
LC10 Sdam 25B 10	-6.30	-4.9	1.00	-1.41	111.57
LC10-SdamB-25b	-6.52	-4.9	1.00	-1.63	113.42
LC10 Sdam 25B 14	-6.61	-4.9	1.00	-1.72	114.14

Table 4: Paleotemperature calculations using temperature dependent fractionation factors by Demeny et al., 2010; Kele et al., 2011; Kim and O'Neil, 1997 and Romanek et al., 1992 (eq. 7, 8, 9; APPENDIX D).

	Romanek et al., 1992				
	Calcite	CO_2	PDB		Temp.
Sample	$d13C_{PDB}$	$d13C_{PDB}$	$\alpha_{CO2\text{-}water}$	1000lnα	°C
LC10 Sdam 25B 15	-6.67	-4.9	1.00	-1.78	114.64
LC10 Sdam 25B 20	-6.69	-4.9	1.00	-1.80	114.85
LC10 Sdam 25B 9	-6.76	-4.9	1.00	-1.88	115.46
LC10 Sdam 25B 13	-6.93	-4.9	1.00	-2.04	116.82
LC10 Sdam 25B 23	-6.98	-4.9	1.00	-2.09	117.24
LC10 Sdam 25B 19	-7.00	-4.9	1.00	-2.11	117.42
LC10 Sdam 25B 17	-7.19	-4.9	1.00	-2.31	119.07
LC10 Sdam 25B 29	-7.33	-4.9	1.00	-2.45	120.24
LC10 Sdam 25B 27	-7.34	-4.9	1.00	-2.45	120.26
LC10 Sdam 25B 26	-7.42	-4.9	1.00	-2.54	120.98
LC10 Sdam 25B 22	-7.59	-4.9	1.00	-2.71	122.38
LC10 Sdam 25B 7	-7.62	-4.9	1.00	-2.74	122.68
LC10 Sdam 25B 1	-7.67	-4.9	1.00	-2.79	123.06
LC10 Sdam 25B 24	-7.76	-4.9	1.00	-2.88	123.83
LC10 Sdam 25B 18	-7.79	-4.9	1.00	-2.91	124.04
LC10 Sdam 25B 21	-7.83	-4.9	1.00	-2.95	124.41
LC10 Sdam 25B 12	-8.06	-4.9	1.00	-3.18	126.33
LC10 Sdam 25B 30	-8.07	-4.9	1.00	-3.19	126.42
LC10 Sdam 25B 25	-8.08	-4.9	1.00	-3.20	126.47
LC10 Sdam 25B 8	-8.21	-4.9	1.00	-3.33	127.57
LC10 Sdam 25B 6	-8.31	-4.9	1.00	-3.43	128.42
LC10 Sdam 25B 3	-8.39	-4.9	1.00	-3.51	129.11
LC10 Sdam 25B 2	-8.69	-4.9	1.00	-3.82	131.67
LC10 Sdam 25B 16	-8.70	-4.9	1.00	-3.83	131.74
LC10 Sdam 25B 4	-8.93	-4.9	1.00	-4.06	133.66
LC10 Sdam 25B 5	-9.00	-4.9	1.00	-4.12	134.21
LC10-SDamB-25d	-9.12	-4.9	1.00	-4.25	135.24
LC10 Sdam 25B 28	-9.26	-4.9	1.00	-4.39	136.41
LC10-SDamB-25c	-9.69	-4.9	1.00	-4.82	140.02
LC10-NMSDC-10	-9.88	-4.9	0.99	-5.01	141.61
LC10-NMSDC-11	-13.23	-4.9	0.99	-8.40	169.87
LC10-NMSDC-12	-11.21	-4.9	0.99	-6.36	152.85
LC10-NMSDC-13	-13.30	-4.9	0.99	-8.47	170.45
LC11-NMSDA 36	-11.24	-4.9	0.99	-6.40	153.13
LC11-NMSDA 36	-11.49	-4.9	0.99	-6.65	155.22
AJT11-SDAM 40	-12.66	-4.9	0.99	-7.83	165.08

Table 4: Paleotemperature calculations using temperature dependent fractionation factors by Demeny et al., 2010; Kele et al., 2011; Kim and O'Neil, 1997 and Romanek et al., 1992 (eq. 7, 8, 9; APPENDIX D).

	Romanek et al., 1992				
	Calcite	CO_2	PDB		Temp.
Sample	$d13C_{PDB}$	$d13C_{PDB}$	$\alpha_{CO2\text{-}water}$	1000lnα	°C
AJT11-SDAM 41	-10.92	-4.9	0.99	-6.07	150.42
AJT11-SDAM 44	-6.92	-4.9	1.00	-2.03	116.77
AJT11-Sdam 43a	-11.48	-4.9	0.99	-6.64	155.16
AJT11-SDAM 40	-12.66	-4.9	0.99	-7.83	165.08
AJT11-SDAM 41	-10.92	-4.9	0.99	-6.07	150.42
AJT11-SDAM 44	-6.92	-4.9	1.00	-2.03	116.77
AJT-SD-1	-10.23	-4.9	0.99	-5.37	144.59
AJT-SD-2	-8.90	-4.9	1.00	-4.03	133.40
LC10-NMSD-5	-10.16	-4.9	0.99	-5.30	144.00
LC10-NMSD-6	-10.67	-4.9	0.99	-5.82	148.29
LC10-Sdam-28 a	-10.72	-4.9	0.99	-5.87	148.72
LC10-Sdam-28 b	-11.28	-4.9	0.99	-6.43	153.43
LC10-Sdam-28 c	-10.53	-4.9	0.99	-5.67	147.11

Table 5: Model ages for out of U-series range travertine samples.

Sample	U(ppm)	U error	$\delta^{234}U_m$	$^{234}U/^{238}U_m$	$(^{234}U/^{238}U)_m$	$\delta^{234}U_i$	$^{234}U/^{238}U_i$
LC10_NMSDA_22a	0.109	0.001	141.4	62.65	1.14	900	104.28
LC10_NMSDA_31	0.109	0.001	57.0	58.01	1.06	900	104.28
LC10_NMSDA_23a	0.088	0.001	159.8	63.66	1.16	900	104.28
	$(^{234}U/^{238}U)_i$	$\delta^{234}U_i$ - error	MAX Age	Age	MIN Age	(+) error	(-) error
LC10_NMSDA_22a	1.9	500	0.81	0.66	0.37	0.16	0.29
LC10_NMSDA_31	1.9	500	1.14	0.98	0.69	0.16	0.29
LC10_NMSDA_23a	1.9	500	0.77	0.61	0.33	0.16	0.29